EXCITATION AND DECAY OF STARK MIXED
n = 2 STATES OF ATOMIC HYDROGEN

SIMON WATKIN

Thesis submitted for the degree of

Doctor of Philosophy

University of Stirling

MAY 1985

I wish to dedicate this thesis to my parents and to Mary

ABSTRACT

The electron impact excitation of the $n = 2$ states of atomic hydrogen has been investigated using the electron-photon coincidence technique.

The parameters λ and R have been determined at incident electron energies of 100eV and 350eV for a small range of scattering angles about the forward direction.

A coincidence apparatus capable of time resolution of the order of half a nanosecond has been developed, permitting the study of the time evolution of the 2S and 2P states of atomic hydrogen which have been coherently excited in the presence of an electric field. The Stark mixing of the 2S and 2P states results in experimental observables which depend on the relative phase of the f_{00} and f_{10} scattering amplitudes. Such quantities have been determined for an incident electron energy of 350eV over a small range of scattering angles about the forward direction.

In addition, a quantum beat pattern, resulting from the interference between the decays of the Stark mixed states, has been observed.

These measurements represent the first attempt to investigate the coherent excitation of states of opposite parity using the coincidence technique.

CONTENTS

CONTENTS (Contd.)

Page

CHAPTER 5: STARK FIELD MEASUREMENTS

LIST OF FIGURES

CHAPTER 1

INTRODUCTION

The study of electron-atom collisions has been the subject of a great deal of both experimental and theoretical effort since the early days of atomic physics. Collision phenomena such as electron impact excitation, elastic scattering and ionization have been investigated for a wide range of atomic systems and incident projectile energies. Obtaining an accurate theoretical description of such phenomena is important in many branches of physics, e.g. astrophysics, atmospheric physics, plasma physics etc. Many theoretical models and approximations exist and it has been the role of experiment to test the validity and accuracy of these models. Since the hydrogen atom is the simplest of all atoms it has been the subject of a great deal of investigation. The fact that exact wavefunctions describing the bound states of the hydrogen atom are known makes electron-hydrogen atom collision phenomena particularly amenable to calculation. However, the technical difficulties involved in obtaining a suitably pure and sufficiently concentrated source of dissociated hydrogen in the laboratory proved a considerable barrier to experimental work with atomic hydrogen. Many of these problems have now been overcome and the last decade has seen much effort directed towards experimental investigations of electron-hydrogen atom collisions.

Until the early 1970's experimental investigations of electron impact excitation of atoms were of two types. The first type of experiment consists of detection of the scattered electrons only. Experiments of this type yield values for total excitation cross-sections (Q), or if electrons are detected as a function of scattering angle, differential cross-sections (σ) as a function of incident electron energy(1). Such cross-sections represent sums of cross-sections for excitation of each degenerate or unresolved atomic state.

The first such experiment on the $n = 2$ states of atomic hydrogen was reported by Williams(2). This work provided relative values of $\sigma(2P) + \sigma(2S)$, where $\sigma(2P)$ is itself a summation over the three degenerate magnetic sublevels with $m_L = 0, \pm 1$, for energies in the range 50 - 200 eV. Williams and Willis(3) reported absolute measurements of this quantity for incident energies in the range 54 - 680 eV.

In the second type of experiment radiation resulting from the spontaneous decay of an atom which has been excited by electron impact is observed without regard to the scattered electrons. Such experiments can yield values for the total excitation cross-section, or if the percentage polarisation of the emitted radiation is measured, it is possible to obtain information on the total cross-sections for excitation of individual magnetic sublevels(1).

Measurements of $Q(2P)$ for atomic hydrogen have been performed by Long et al.(4), McGowan et al.(5) and Williams and Willis(6) and values of $Q(2S)$ obtained by Ott et al.(7) and Kauppcla et al.(8).

The experimental techniques described above are capable of yielding total and differential cross-sections summed over degenerate or unresolved atomic states or, alternatively, cross-sections for excitation to individual degenerate magnetic sublevels, averaged over all electron scattering angles. It is clear that an experimental technique that provided cross-sections for excitation to individual magnetic sublevels which were differential in electron scattering angle would pose an additional test of theory. The application of the electron-photon coincidence technique to the study of electron-atom collisions has provided such a test.

The method of detecting two particles in delayed coincidence has been in use for many years in the field of nuclear physics. It was used by Brady and Deutsch(9) to investigate the non-isotropic emission of gamma rays which had been predicted by Dunsworth(10). The first calculations of such an angular distribution(11) were very complicated until the introduction of the use of spherical tensor operators by Racah(12) and the density matrix formalism by Coester and Jauch(13) in the 1950's. The theory developed for nuclear studies is not directly applicable to atomic studies but many features of the theory have followed closely earlier developments in the field of nuclear physics.

The first full theoretical treatment of photon-particle coincidence measurements as applicable to atomic studies was given by Macek and Jaecks(14). The field has been further developed by Fano and Macek(15) and Blum(16). As in the case of nuclear studies the introduction of the density matrix formalism, suggested by Fano(17), and the use of spherical tensor operators(15), has simplified calculations of the angular distribution of the radiation. For a detailed account of such theory the reader is referred to Blum(16).

The electron-photon coincidence technique has now been applied in a wide variety of experimental situations and recent developments have been the subject of a review by Slevin(18).

In the course of the development of the theoretical analysis of electron-photon coincidence experiments it became apparent that this technique could yield information on additional target parameters such as alignment and orientation as well as permitting an investigation of the coherent nature of the excitation process.

Since the collision time is generally much shorter than any characteristic time associated with the excited state the excitation process is coherent and thus the ensemble of excited atoms may be described in terms of a linear superposition of a suitable set of basis states. The complex coefficients in this superposition are the scattering amplitudes. Experiments which measure cross-sections determine only the moduli squared of these amplitudes. It can be shown that experiments which possess axial symmetry can only yield values for cross-sections(15),(17) and thus no information on the relative phases of the scattering amplitudes can be obtained. In an experiment where both the scattered electrons and the emitted photons are detected in coincidence the incident and scattered electron directions define a plane, the scattering plane, so that the geometry possesses reflection symmetry. This lower symmetry has the consequence that quantities which depend on interference terms between the scattering amplitudes may be measured. Thus information on the relative phases of the amplitudes may be obtained. Such measurements may be expected to provide a particularly sensitive test of theory.

The first coincidence experiment in the field of atomic physics was carried out by Eminyan et al.(19) who studied the electron impact excitation of the 2^1P state of helium. Such measurements yield direct information on the relative phase of the amplitudes for excitation of the $m = 0$ and $m = 1$ magnetic substates. This work has been extended by several groups(20)-(28), while the excitation of the 3^1P state of helium has been the subject of a study by Standage and Kleinpoppen(29). The coincidence technique has also been used to study the 3^1D and 3^1P states of helium by van Linden et al.(30),(31).

The first coincidence study of atomic hydrogen was reported by Williams(32) who investigated the excitation and decay of the 2P state of hydrogen. The analysis of such an experiment is rather more complicated than the case of a singlet-singlet transition, (see for example, Chapter 6 of reference (15)), due to the presence of the atomic spin. Coincidence studies of the 2P state of hydrogen have been reported by a number of authors(33)-(39), while Frost and Weigold(37) and Williams(38) have extended the technique to yield information on the differential cross-section for excitation to the 2S state. These studies yield information on the coherence between states of the same orbital angular momentum but differing magnetic quantum number. However, in general, excitation by electron impact results in a coherent superposition of states of different orbital angular momentum. This thesis reports the first use of the coincidence technique to investigate the coherence between states of different orbital angular momentum.

A coherent superposition of states which are non-degenerate and which can decay to the same final state exhibit interference effects which result in oscillations in the emitted light intensity. Such oscillations are usually referred to as "quantum beats". Interference effects between fine and hyperfine levels, giving rise to quantum beat patterns in the emitted radiation, was first treated by Macek(40). Fine and hyperfine structure beats have been observed in a wide variety of atomic transitions in beam-foil experiments and have been reviewed by Macek and Burns(41). Quantum beats arising from the hyperfine structure of the $J = \frac{3}{2}$ level of the 3^2P state of sodium have been observed by Teubner$^{(42)}$. These beats however are the result of coherence induced by the fine-structure interaction rather than the excitation process as noted by Eck$^{(43)}$. Macek$^{(40)}$ pointed out that it was possible for beats to occur between states of different orbital angular momentum and such beats must arise from true coherence in the excitation process. Beats of this nature have been observed by Burns and Hancock$^{(44)}$ in a beam-foil experiment. They observed a quantum beat signal which was attributable to interference between the 3S and 3D states of atomic hydrogen. The effect of coherent excitation of the $n = 3$ states of hydrogen has also been observed by Mahan and Smith$^{(43)}$. Mahan and Smith observed that the intensity of Balmer-α radiation resulting from the electron impact excitation of the $n = 3$ states of hydrogen was dependent on the strength and direction of an applied electric field. The dependence on field strength is a consequence of the Stark-mixing of the $n = 3$ states, while the dependence on field direction is attributable to the effect of coherent excitation of states of opposite parity as discussed by Krotkov$^{(46)}$.

The coherent excitation of states of opposite parity in electron-hydrogen collisions has been discussed by Blum and Kleinpoppen$^{(47)}$ and Eck$^{(43)}$. The coherent excitation of the $n = 2$ states of hydrogen has received particular attention. The excitation of the 2P state has been the subject of extensive study, both experimental and theoretical. Interference terms between amplitudes describing the excitation of the 2S and 2P states do not give rise to an experimentally observable effect in the absence of external fields, since the 2S state cannot decay to the 1S ground state. The interference term between the amplitudes describing excitation to substates with magnetic quantum number $m_L = 0$ of the 2S and 2P states is of particular interest. Gabrielse and Band(48) show that the real and imaginary parts of this term are proportional to the electric dipole moment induced by the collision and its time derivative respectively. Information on this term can only be obtained in the presence of an external electric field to mix the 2S and 2P states.

This so-called S - P coherence term has been the subject of measurements in beam-foil experiments by Sellin et al.(49), Gaup et al.(50), in charge transfer processes by Sellin et al.(51), Havener et al.(52) and in atom-atom collisions by Krotkov and Stone(53).

This thesis reports the first attempt to employ the electron-photon coincidence technique to investigate the coherent excitation of states of opposite parity. The use of this method to obtain information on the S - P coherence term has the advantages that observations are free from problems due to cascade effects and the measurements relate to collisions in which electrons are scattered into a small range of angles.

The data reported in this thesis were obtained using deuterium rather than hydrogen in order to minimise any effects due to hyperfine structure.

The layout of this thesis is as follows. Chapter 1 is the present introduction. In Chapter 2 the relevant theory of electron impact excitation and subsequent decay of the $n = 2$ levels of atomic hydrogen is outlined. The form of the coincidence signal in both the zero field case and the case where excitation takes place in the presence of an electric field is obtained. Chapter 3 describes the apparatus used and Chapters 4 and 5 detail the analysis and results in the field free case and the case where excitation takes place in an electric field respectively.

The results have previously been reported by Back et al. (73).

CHAPTER 2

In this chapter the basic theory of electron impact excitation and the subsequent decay of an atom is outlined. The description of the excited atomic state prepared by the collision is discussed and the time evolution, including the effects of internal and external fields, of such a state considered. The extraction of important parameters relating to the collision from electron-photon coincidence measurements is then described.

I. Description of the Excited State

The description of the quantum mechanical state of an ensemble of atoms has been discussed by many authors, particularly Fano(17) and more recently Blum(16). Fano discussed the distinction between 'mixed' and 'pure' quantum mechanical states of a system. A pure state is one which may be represented by a single wavefunction or state vector. Such a state may be conveniently specified by expanding the state vector as a linear superposition of a suitable set of eigenstates. This requires that both the magnitudes and relative phases of the coefficients in the expansion be specified, (in the case of electron impact excitation these coefficients are just the scattering amplitudes). A mixed state, by contrast, cannot be assigned a single state vector but must be specified in terms of a suitable set of states and their appropriate statistical weights comprising the mixture. In this case the state is specified in terms of the squares of the amplitudes in the expansion, i.e. there is no definite phase relationship between the amplitudes and the state is often referred to as an 'incoherent' superposition of basis states. A pure state is referred to as a 'coherent' superposition since definite phase relationships exist between the amplitudes in the expansion. The lack of information inherent in a mixed state manifests itself in terms of an additional statistical averaging in predicting the result of an experiment.

The use of the terms coherent and incoherent above depend on the particular choice of basis states chosen. This point will be illustrated in the following discussion.

A convenient means of describing a mixed state is the density matrix formalism. This has been developed by a number of authors. The following discussion follows the approach taken by Blum$^{(16)}$.

The general density operator may be defined as

$$\rho = \sum_n |\chi_n\rangle\langle\chi_n| W_n \tag{2.1}$$

where W_n is the statistical weight attributed to each state $|\chi_n\rangle$ comprising the mixture, which may itself be a pure state. Expanding the $|\chi_n\rangle$ in terms of a basis $|\phi\rangle$

$$|\chi_n\rangle = \sum_i |\phi_i\rangle a_i^n \tag{2.2}$$

and taking the outer product the density matrix elements in the $|\phi_i\rangle$ representation are given by

$$\langle\phi_i|\rho|\phi_j\rangle = \sum_n a_i^n a_j^{n*} W_n \, . \tag{2.3}$$

The matrix (2.3), consisting of all relevant bilinear combinations of the a_i^n, contains all possible information on the system.

The diagonal elements of the matrix (2.3) are related to excitation cross-sections. The off-diagonal elements on the other hand contain the relative phase of amplitudes. For a system in a mixed state these terms average to zero over the atomic ensemble and so an incoherent superposition is represented by a diagonal matrix. For a coherent (or partially coherent) superposition of states the off-diagonal terms are in general non-vanishing. Therefore in order to obtain information on the coherent nature of the excited state and hence on the relative phases of the amplitudes it is necessary to determine the off-diagonal elements of the density matrix.

The density matrix describing $n = 2$ level of atomic hydrogen excited by electron impact may be obtained in the following way. Consider atoms initially in the ground state with angular momentum $L_o = 0$ and characterised by the quantum numbers $\gamma_o = n_o S_o M_{so}$ where S_o and M_{so} denote the spin and its third component and n_o all other quantum numbers necessary to specify the state. The initial state of the electrons is characterised by momentum p_o and spin component m_o. Consider a transition from the initial state of the system $\Gamma_o = \gamma_o p_o m_o$ to an excited state $\Gamma_1 = \gamma_1 p_1 m_1$, with $\gamma_1 = n_1 L M S_1 M_{s1}$. We characterise this transition by the scattering amplitude (Chapter 3: ref. (16))

$$f(\Gamma_1 \Gamma_o) = f(\gamma_1 p_1 m_1 ; \gamma_o p_o m_o) \; . \qquad (2.4)$$

These amplitudes may be normalised according to

$$|f(\Gamma_1 \Gamma_o)|^2 = \sigma(\Gamma_1 \Gamma_o) \qquad (2.5)$$

where $\sigma(\Gamma_1 \Gamma_o)$ is the cross-section for the transition $\Gamma_o \rightarrow \Gamma_1$.

The determination of the amplitudes $f(\Gamma_1\Gamma_o)$ requires a determination of both the magnitude and the phase.

The detection of electrons of fixed momentum p_1 which have been scattered through a particular angle, θ_e say, allows the dependence on n_1, p_1 and p_o to be dropped. The amplitudes (2.4) however still depend on the initial and final spins of atoms and electrons. We consider here the case where no spin analysis of atoms or electrons is carried out. The amplitudes in (2.4) must therefore be averaged over initial spin states and summed over the final spin states of the system giving the quantities

$$<f_{L'M'}\, f^*_{LM}> \;=\; \frac{1}{2(2S_o+1)} \sum_{\substack{m_o m_1 \\ M_{so} M_{s1}}} f(\Gamma_1{}'\Gamma_o) f(\Gamma_1\Gamma_o)^* \qquad (2.6)$$

where $\Gamma_1{}' = n_1 L'M'M_{s1} p_1 m_1$ and the brackets $<\;>$ denote that the left side of (2.6) represents spin-averaged quantities. This averaging process reflects the fact that since no analysis of the initial and final spin states is performed the initial and final states of the system are incompletely specified and are therefore mixed states, i.e. an incoherent superposition of spin states. However the excited state may be considered as being coherent with respect to the orbital angular momentum states. The quantities (2.6) may then be arranged in matrix form.

$$\rho = \left(\begin{array}{c:ccc} <f_{00}f_{00}^*> & <f_{00}f_{11}^*> & <f_{00}f_{10}^*> & <f_{00}f_{1-1}^*> \\ \hdashline <f_{11}f_{00}^*> & <f_{11}f_{11}^*> & <f_{11}f_{10}^*> & <f_{11}f_{1-1}^*> \\ <f_{10}f_{00}^*> & <f_{10}f_{11}^*> & <f_{10}f_{10}^*> & <f_{10}f_{1-1}^*> \\ <f_{1-1}f_{00}^*> & <f_{1-1}f_{11}^*> & <f_{1-1}f_{10}^*> & <f_{1-1}f_{1-1}^*> \end{array}\right) \qquad (2.7)$$

The above may be compared with the case of a singlet-singlet transition where the absence of spin makes the brackets < > in (2.6) redundant and the state may be specified completely by a single state vector, i.e. a pure state. The 2^1P state of Helium is such a case(19).

The matrix (2.7) can be divided into four submatrices as shown. The single element in the upper left is simply proportional to the excitation cross-section of the 2S state. The 3×3 matrix characterises the excitation of the 2P state. The diagonal elements are related to cross-sections for the excitation of the different magnetic sublevels of the 2P state, while the off-diagonal elements represent the coherence between these sublevels. The remaining elements characterise the coherence between the 2S and 2P states, the so-called 'interference terms'. Of particular significance is the 'S - P coherence term' $<f_{10} f^*_{00}>$. The $\mathrm{Re}<f_{10} f^*_{00}>$ is directly proportional to the permanent electric dipole moment induced by the collision, while the $\mathrm{Im}<f_{10} f^*_{00}>$ is its time derivative(48).

The 2S state cannot decay to the 1S ground state by electric dipole radiation. Therefore in the field-free situation the radiation is completely characterised by the 3×3 2P submatrix. If, however, an external electric field is applied the 2S and 2P states become mixed (Stark effect) and radiation from the subsequent decay is characterised by terms which depend on the 'S - P coherence term', as will be shown later.

Consider first the 3×3 2P submatrix. The diagonal elements are real numbers, the off-diagonal elements are complex quantities specified by a magnitude and a phase. The matrix (2.7) is therefore completely specified in terms of 15 real parameters. It is clear from (2.3) that ρ is Hermitian, thus

$$<LM'|\rho|LM> \quad = \quad <LM|\rho|LM'>^* \qquad (2.8)$$

This relationship reduces the number of independent parameters to 9. In the case of a system with symmetry about a plane, such as a coincidence experiment, where the scattering plane is defined by the directions of incident and scattered electrons, the atomic system must be invariant with respect to reflections in this plane, which implies

$$\begin{aligned} f(n_1 L M S_1 M_{s1} p_1 m_1 : n_o S_o M_{so} p_o m_o) &= \\ (-1)^{M+M_{s1}+m_1-M_{so}-m_o+S_1-S_o} & f(n_1 L - M_{s1} p_1 - m_1 : n_o S_o - M_{so} p_o m_o). \end{aligned} \qquad (2.9)$$

Since the case of interest is one in which no spin analysis is performed (2.9) must be spin averaged as before to yield the following condition for the density matrix elements.

$$\langle LM'|\rho|LM\rangle = (-1)^{M'+M} \langle L - M'|\rho|L - M\rangle \quad . \qquad (2.10)$$

Applying (2.8) and (2.10) to the case of the 2P submatrix, the density matrix $\rho(2P)$ may be completely specified by five real independent parameters: σ_o, σ_1, $\mathrm{Re}\langle f_{10}\, f_{11}^*\rangle$, $\mathrm{Im}\, \langle f_{10}\, f_{11}^*\rangle$ and $\langle f_{-1}\, f_1^*\rangle$ which is real. A further reduction in the number of independent parameters is possible in cases where spin-dependent terms in the Hamiltonian may be neglected, i.e. light atoms. Since in these cases total spin S and its component M_S must be conserved during the collision the additional condition

$$\langle LM'|\rho|L - M\rangle = (-1)^M \langle LM'|\rho|LM\rangle \qquad (2.11)$$

for the density matrix elements may be obtained (Chapter 3: ref. (16)). Therefore the matrix $\sigma(2P)$ for hydrogen is completely specified by four real independent parameters since $<f_{-1} f_1^*> = -\sigma_1$. The density matrix is commonly parameterised using the quantities

$$\begin{aligned} \sigma &= 2\sigma_1 + \sigma_o \\ \lambda &= \sigma_o/\sigma \\ R &= \mathrm{Re} <f_{10} f_{11}{}^*>/\sigma \\ I &= \mathrm{Im} <f_{10} f_{11}{}^*>/\sigma \end{aligned} \tag{2.12}$$

In the absence of spin, e.g. a singlet-singlet transition, $L = 1$, the number of independent parameters is reduced to three, since condition (2.9) reduces to $f_{LM} = (-1)^M f_{L-M}$. This reduction in the number of independent parameters necessary to specify the state is a consequence of the lack of information inherent in the mixed spin states.

When the angular symmetries of a system are of interest it is often useful to expand ρ in terms of irreducible tensor operators. The following treatment is taken from Blum$^{(16)}$.

Consider two ensembles of particles with angular momentum J and J'. The states of the joint system may be denoted by the total angular momentum K and its z-component Q. Applying the usual angular momentum coupling rules gives

$$|J'J\ K\ Q> = \sum_{M'M} (J'M',JM|KQ)|J'M'>|JM> \tag{2.13}$$

where the states $|JM>$ are orthonormal. Forming a set of operators, analogous to (2.1), $|J'M'><JM|$, we define a set of operators $T(J'J)_{KQ}$.

$$T(J'J)_{KQ} = \sum_{M'M} (-1)^{J-M} (J'M',\ J-M|KQ)|J'M'><JN| \tag{2.14}$$

where the Clebsh-Gordan coefficient vanishes unless the usual angular momentum coupling rules apply

$$|J' - J| \leq K \leq J' + J \qquad -K \leq Q \leq K\ . \tag{2.15}$$

The density operator ρ may be expanded in terms of the tensor operators $T(J'J)_{KQ}$

$$\rho = \sum_{\substack{J'J\\KQ}} \langle T(J'J)^{\dagger}_{KQ}\rangle\, T(J'J)_{KQ} \tag{2.16}$$

The coefficients in the expansion or 'state multipoles' are given by

$$\langle T(J'J)^{\dagger}_{KQ}\rangle = \mathrm{tr}\,\rho\, T(J'J)^{\dagger}_{KQ} \tag{2.17}$$

where tr is the trace of the operator product and $\dagger$ indicates the adjoint operator given by

$$T(J'J)^{\dagger}_{KQ} = (-1)^{J'-J+Q}\, T(JJ')_{K-Q}\ . \tag{2.18}$$

The elements of the density matrix are given by the expression

$$\langle J'M'|\rho|JM\rangle = \sum_{KQ} (-1)^{J'-M'}(2K+1)^{\frac{1}{2}} \begin{bmatrix} J' & J & K \\ M' & -M & -Q \end{bmatrix} \langle T(J'J)^{\dagger}_{KQ}\rangle \tag{2.19}$$

where the quantity in square brackets is a 3j-symbol. (19) may be inverted to yield

$$\langle T(J'J)^{\dagger}_{KQ}\rangle = \sum_{M'M} (-1)^{J'-M'}(2K+1)^{\frac{1}{2}} \begin{bmatrix} J' & J & K \\ M' & -M & -Q \end{bmatrix} \langle J'M'|\rho|JM\rangle \tag{2.20}$$

The two descriptions of the system are therefore equivalent.

Some basic properties of the state multipoles are quoted below.

The state multipoles transform under rotations through Euler angles ω according to

$$\langle T(J'J)^{\dagger}_{KQ}\rangle \quad = \quad \sum_{q} \langle T(J'J)^{\dagger}_{Kq}\rangle \, D(\omega)^{(K)^{*}}_{qQ} \quad . \qquad (2.21a)$$

Using equation (2.20) the hermicity condition (2.8) becomes

$$\langle T(J'J)^{\dagger}_{KQ}\rangle \quad = \quad (-1)^{J'-J+Q} \langle T(JJ')^{\dagger}_{K-Q}\rangle \quad . \qquad (2.21b)$$

Reflection invariance in a plane, the x-z plane, leads to the condition

$$\langle T(J'J)_{KQ}{}^{\dagger}\rangle \quad = \quad (-1)^{J'+J+K+Q} \langle T(J'J)^{\dagger}_{K-Q}\rangle . \qquad (2.21c)$$

It is easy to show that state multipoles with $J \neq J'$ describe the coherence between states of different angular momentum, while multipoles with $Q \neq 0$ describe the coherence between states of different magnetic quantum number M (Chap. 4: ref. (16)).

In the case of sharp angular momentum, i.e. $J' = J$ the state multipoles have a simple physical interpretation. The tensor with rank $K = 0$ is just a normalisation constant

$$\langle T(J)_{oo}\rangle \quad = \quad \frac{\mathrm{tr}\,\rho}{(2J+1)} \quad . \qquad (2.22)$$

The three components with rank $K = 1$ and $Q = 0, \pm 1$ transform as components of a vector

$$\langle T(J)^{\dagger}_{1Q}\rangle \quad = \quad \left[\frac{3}{(2J+1)(J+1)J}\right]^{\frac{1}{2}} \langle J^{\dagger}_{Q}\rangle \; \mathrm{tr}\,\rho \qquad (2.23)$$

where the operators $J^{\dagger}_{Q}$ are just the adjoint operators of the spherical angular momentum operators. The vector with components (2.23) is called the 'orientation vector' and is a measure of the anisotropy of the angular momentum distribution and thus determines the induced magnetic moment of the particles (Chap. 4: ref. 16)). For axially symmetric systems only $\langle T(J)^{\dagger}_{10}\rangle$ is non-vanishing.

The multipoles of rank $K = 2$ may be expressed in terms of quadratic combinations of the angular momentum components and form the 'alignment tensor'. The components of the alignment tensor are proportional to the spherical components of the electric quadrupole tensor $\langle Q_{2Q}\rangle$(48). Again all components with $Q \neq 0$ vanish if the system possesses axial symmetry.

The above state multipoles are also closely related to the orientation and alignment parameters introduced by Fano and Macek(15).

The above interpretation of the state multipoles is only valid in the case of sharp angular momentum, i.e. $J' = J$.

The complete set of state multipoles characterizing the 2P state of atomic hydrogen is given below:

$$\begin{aligned}
\langle T(1)^{\dagger}_{00}\rangle &= \frac{1}{\sqrt{3}}\,\sigma(2p) \\
\langle T(1)^{\dagger}_{10}\rangle &= \frac{i}{\sqrt{3}}\,\mathrm{lm}\,\langle f_{11}\, f^{*}_{10}\rangle \\
\langle T(1)^{\dagger}_{20}\rangle &= \sqrt{\frac{2}{3}}\,\langle |f_{11}|^{2} - |f_{10}|^{2}\rangle, \quad \langle T(1)^{\dagger}_{21}\rangle = -\sqrt{2}\,\mathrm{Re}\langle f_{11}\, f^{*}_{10}\rangle \\
\langle T(1)^{\dagger}_{22}\rangle &= \langle |f_{11}|^{2}\rangle
\end{aligned} \tag{2.24}$$

where $\sigma(2P) = \sum_{M} \sigma_{LM} = \sum_{M}\langle |f^{2}_{LM}|\rangle$ and conditions (2.21a - c) reduce the number of independent multipoles to five. It can be seen that in fact only four multipoles are independent in this case.

II. Time Evolution of the Excited State

The state multipoles (2.17) or equivalently the density matrix (2.3) provide a complete description of the excited atomic ensemble immediately after the collision. In cases where internal or external fields are present it is necessary to consider the time evolution of the state under the influence of these fields in order to extract information on the collision from electron-photon coincidence measurements.

Consider an ensemble of atoms in an excited state bescribed by a Hamiltonian $H = H_o + H'$ where H' denotes a perturbation which is assumed to be unimportant during the excitation process, i.e. the excitation time is short compared with any characteristic transition times caused by the perturbation H'. H' may be the fine of hyperfine interactions or an external field or any combination of these. At time $t = 0$ the atoms are described by the density matrix $\rho(0)$ or state multipoles $\langle T(J'J)^{+}_{KQ}\rangle$. The density matrix evolves in time according to

$$\rho(t) = U(t)\rho(0)U^{+}(t) \tag{2.25}$$

where the time evolution operator $U(t) = \exp[\frac{-i}{\hbar}Ht]$ (Chap. 2: ref. 16)). An initial state $|JM\rangle$ is transformed by $U(t)$ according to

$$|\phi(t)\rangle = U(t)|JM\rangle \tag{2.26}$$

which can be expanded in terms of a full set of eigenstates, $|jm\rangle$, of the Hamiltonian H_o. Expanding $\rho(t)$ gives

$$\rho(t) = \sum_{\substack{j'j\\kq}} \langle T(j'j:t)^{+}_{kq}\rangle\, T(j'j)_{kq} \tag{2.27}$$

where j' and j run over all possible angular momenta states at time t. Then

$$\begin{aligned}
\langle T(j'j:t)^{\dagger}_{kq}\rangle &= \mathrm{tr}\ \rho(t)T(j'j)^{\dagger}_{kq} \\
&= \mathrm{tr}\ U(t)\rho(0)U^{\dagger}(t)T(j'j)^{\dagger}_{kq} \\
&= \sum_{\substack{J'J \\ KQ}} \langle T(J'J^{\dagger}_{KQ}\rangle\ \mathrm{tr}[U(t)T(J'J)_{KQ}U^{\dagger}(t)T(j'j)^{\dagger}_{kq}] \\
&= \sum_{\substack{J'J \\ KQ}} \langle T(J'J)^{\dagger}_{KQ}\rangle\ G(J'J,\ j'j:t)^{Qq}_{Kk} \qquad (2.28)
\end{aligned}$$

which relates state multipoles at time $t = 0$, $\langle T(J'J)^{\dagger}_{KQ}\rangle$, to those at time t, $\langle T(j'j:t)^{\dagger}_{kq}\rangle$ via the set of 'perturbation coefficients' $G(J'J;j'j:t)^{Qq}_{Kk}$ defined by

$$G(J'J,j'j:t)^{Qq}_{Kk} = \mathrm{tr}[U(t)T(J'J)_{KQ}U^{\dagger}(t)T(j'j)^{\dagger}_{kq}] \qquad (2.29)$$

(Chap. 4: ref (16)).

For a state of sharp orbital angular momentum, L, and spin S_1, evolving under the influence of the fine structure interaction (2.29) may be evaluated to give

$$G(L,t)_K = \frac{1}{2S_1+1} \sum_{JJ'} (2J+1)(2J'+1) \begin{bmatrix} L & J' & S_1 \\ J & L & K \end{bmatrix}^2 \cos\left[\frac{(E_{J'}-E_J)t}{\hbar}\right] \qquad (2.30)$$

In this case the perturbation coefficients are independent of Q and the interaction does not mix multipoles of different rank K.

(2.30) can be seen to consist of a time independent part, $J' = J$ and an oscillatory part when $J' \neq J$, i.e. the state multipoles oscillate about some mean value under the influence of the fine structure interaction.

The case where hyperfine interactions must be included is dealt with in Blum(16) and leads to an essentially similar result to (2.30).

The perturbation coefficients may be determined in an identical manner to the above when an external field is applied. The perturbation due to the external field is included in the total Hamiltonian occurring in (2.25). For the case of an electric field applied to hydrogen atoms excited by electron impact to the $n = 2$ state the general theory has been given by Blum and Kleinpoppen(47).

Since the presence of the electric field causes the S and P states to become mixed by the Stark effect, the radiation emitted in a transition to the ground state is no longer characterised by the 3×3 submatrix which describes only the P state excitation but rather the full $n = 2$ density matrix (2.7) must be considered. Thus the observation of radiation emitted in such a transition offers the opportunity to obtain information on the S - P coherence term. Blum and Kleinpoppen(47) present the general theory of this decay in terms of state multipoles and perturbation coefficients similar to that outlined above for the field-free case. A new set of multipoles in the coupled representation $\langle T(L'J_i', LJ_i)^{\dagger}_{KQ}\rangle$ are defined and the form of the relevant perturbation coefficients obtained.

$$G(t)^{Qq}_{Kk} = \sum_{\substack{M_i'M_i \\ m_i'm_i}} \langle \ell'\tfrac{1}{2}j_i'm_i'|U(t)|L'\tfrac{1}{2}J_i'M_i'\rangle\langle L'\tfrac{1}{2}J_i'M_i'|T(L'J_i',LJ)_{KQ}|L\tfrac{1}{2}J_iM_i\rangle$$

$$\times \langle L\tfrac{1}{2}J_iM_i|U^{\dagger}(t)|\ell\tfrac{1}{2}j_im_i\rangle\langle \ell\tfrac{1}{2}j_im_i|T(\ell'j_i'\ell j_i)^{\dagger}_{kq}|\ell'\tfrac{1}{2}j_i'm_i'\rangle \ . \qquad (2.31)$$

The coefficients

$$a(\ell j_i L J_i : t) = \langle \ell\tfrac{1}{2}j_iM_i|U(t)|L\tfrac{1}{2}J_iM_i\rangle \qquad (2.32)$$

are just the probability amplitudes for finding a state $|\ell \tfrac{1}{2} j_i m_i\rangle$ at time t if at time $t = 0$ the system was in the state $|L\tfrac{1}{2}J_i M_i\rangle$

$$|L\tfrac{1}{2}J_i M_i\rangle \rightarrow |\psi(t)_{LJ_i}\rangle = U(t)|L\tfrac{1}{2}J_i M_i\rangle$$

$$= \sum_{\ell j_i} a(\ell j_i L J_i : t)|\ell\tfrac{1}{2}j_i m_i\rangle . \qquad (2.33)$$

The determination of the coefficients (2.32) requires the solving of the set of coupled differential equations

$$ih \frac{d}{dt} a(\ell j_i L J_i : t) = \sum_{\ell' j_i'} a(\ell' j_i' L J_i : t)\langle \ell'\tfrac{1}{2} j_i' M_i|H|L\tfrac{1}{2}J_i M_i\rangle$$

$$- \tfrac{1}{2}\, i\hbar\, \Gamma_{\ell j_i}\, a(\ell j_i L J_i : t) \qquad (2.34)$$

with the initial condition that

$$a(\ell' j_i' L J_i , 0) = \delta_{\ell' L}\, \delta_{j_i' J_i} \quad . \qquad (2.35)$$

The decay of the excited state has been included in (2.34) by writing the time evolution operator in the form

$$U(t) = \exp\left[- \frac{i}{\hbar} Ht - \tfrac{1}{2}\Gamma t\right]$$

where Γ is the decay matrix.

The solution of the equations (2.34) is straight forward for the case of the $n = 2$ states of atomic hydrogen when only the $S_{1/2}$ and $P_{1/2}$ states are included and has been done by the author. The $P_{3/2}$ state is often neglected in such a case since the $P_{3/2} - S_{1/2}$ energy separation is approximately ten times that of the $P_{1/2} - S_{1/2}$. However Burgdörfer(54) has pointed out that despite this fact, inclusion of the $P_{3/2} - S_{1/2}$ coupling can effect the lifetimes of the Stark mixed states by as much as 10%. The inclusion of the $P_{3/2} - S_{1/2}$ coupling in the treatment of Blum and Kleinpoppen(47) results in nine coefficients in equations (2.34). An analytic solution of these equations is difficult to obtain and so an alternative, numerical approach was adopted. Details of this are given later.

III. Decay of the Excited State

Photons emitted in a transition from an upper state, which may be considered as a superposition of angular momentum states $|J_1M_1>$, to a lower state, a superposition of states $|J_2M_2>$, may be described in terms of their polarization states. Using the helicity representation the basis states are $|\lambda>$, $\lambda = \pm 1$ where λ is the spin component along the direction of emission $\underline{n}$. The general polarisation state $|e>$ may be written

$$|e> \;=\; a_1|+1> \;+\; a_{-1}|-1> \quad . \tag{2.37}$$

The density matrix describing photons of frequency ω emitted in a direction $\underline{n}$ is given by

$$\rho_{\lambda\lambda'} \;=\; <\omega\underline{n}\lambda|\rho|\omega\underline{n}\lambda'> \quad . \tag{2.38}$$

Consider atoms which have been excited by electron impact. Immediately after the collision the atomic ensemble may be characterised by the density matrix $\rho(0)$, which evolves in time according to equation (2.25) into a density matrix $\rho(t)_{out}$ describing the state of the atoms plus radiation field at time t. The decay process may be described in first order perturbation theory and thus the time evolution operator is given by (Chap. 5: ref. (16))

$$U(t) \;=\; U(t_o)\left[1 - \frac{i}{\hbar}\int_o^t u(\tau)_o^{\dagger}\, V\, u(\tau_o)d\tau\right] \tag{2.39}$$

where $U(t_o)$ is the free time evolution operator and the operator V describes the interaction between the atoms and the virtual radiation field. The quantities of interest are the elements of the reduced density matrix $\rho(t)$ describing the polarisation state of the emitted photons

$$<\omega\underline{n}\lambda|\rho(t)\omega\underline{n}\lambda'> \;=\; \sum_{J_2M_2} <J_2M_2\omega\underline{n}\lambda|\rho(t)_{out}|J_2M_2\omega\underline{n}\lambda'> \quad . \qquad (2.40)$$

By applying equations (2.25) and (2.39) and using the dipole approximation (2.40) may be simplified to yield

$$\rho(\underline{n}t)_{\lambda'\lambda} \;=\; c(\omega) \sum_{\substack{J_2M_2\\ J_1'M_1'\\ J_1M_1}} <J_2M_2|r_{-\lambda}|J_1'M_1'><J_1'M_1'|\rho(0)|J_1M_1><J_1M_1|r^{\dagger}_{-\lambda}|J_2M_2>$$

$$\times\; \frac{1 - \exp[-i(E_{1'}-E_1)\frac{t}{\hbar} - (\gamma_{1'}-\gamma_1)\frac{t}{2}]}{i(E_{1'}-E_1)\hbar + (\gamma_{1'}+\gamma_1)/2} \qquad (2.41)$$

where $c(\omega) \;=\; \frac{e^2\omega^4 d\Omega}{2\pi c^3\hbar}$ and $-r_{-\lambda} \;=\; r^{\dagger}_{-\lambda} \;=\; e^{\dagger}_{\lambda}\cdot r$

and $E_{1'}$, $\gamma_{1'}$ and E_1, γ_1 denote the energy and decay constants of the states $|J_{1'}\, M_{1'}>$ and $|J_1M_1>$ respectively.

The density matrix (2.41) is usually normalised according to

$$\mathrm{tr}\,\rho(\underline{n}t) \;=\; \sum_{\lambda=\pm 1} \rho(\underline{n},t)_{\lambda\lambda} \;=\; I(t) \qquad (2.42)$$

where $I(t)$ is the total intensity, summed over all polarisations, emitted in the direction $\underline{n}$ as a function of time.

A general expression for $I(t)$ may be written in terms of state multipoles and perturbation coefficients

$$I(\underline{n}t) = c(\omega) \sum_{\substack{L_oL'L \\ KQ}} W(L_oL'L)C(K) \begin{vmatrix} 1 & 1 & K \\ L' & L & L_o \end{vmatrix} D^K_{QQ'}(\underline{n}) \langle T(L'L)^{\dagger}_{KQ} \rangle G(L'Lt)_K \tag{2.43}$$

where $W(L_oL'L) = \langle L_o \| \underline{r} \| L \rangle \langle L_o \| \underline{r} \| L' \rangle^* (-1)^{L_o+L+1}$ and $C(K)$ is a numerical factor.

The initial excited state of the atoms is described by the state multipoles which evolve under the influence of any internal and/or external fields according to the appropriate perturbation coefficients. The rotation matrix elements transform multipoles defined with respect to $\underline{n}$ as quantisation axis to a coordinate system $x - y - z$, usually the 'collision system'. The 6j-symbol and the term $W(L_oL'L)$ characterise the decay process.

(2.43) and its time integrated form then gives the form of the coincidence signal observed in electron-photon coincidence measurements of the type described in this thesis since it describes the intensity emitted in a particular direction by atoms having been. excited by electrons which are scattered in some particular direction θ_e (through its dependence on the scattering amplitudes in the $\langle T(L'L)^{\dagger}_{KQ} \rangle$).

It is clear from (2.43) and (2.30) that the presence of fine structure or hyperfine interactions will cause the light intensity emitted in some direction $\underline{n}$ to be modulated in time. This modulation is referred to as 'quantum beats'. In the general case where the excited state is a coherent superposition of states with different orbital angular momentum L more than one type of 'beat' term arises. Beats between states of different L are superimposed on beats between states of the same L but different total angular momentum J_1, the 'fine structure beats' (also hyperfine structure beats occur).

Observation of quantum beats requires that the two upper states must decay to the same final state. In the case of the $n = 2$ states of hydrogen beats between the S and P states are therefore only observable in the presence of an external field. In the field-free situation only the 2P state decays and hence only the fine structure beats are observable. However the period of these beats, ∿ 0.1ns, is well beyond the time resolution of existing coincidence experiments (although not of beam-foil experiments$^{(41)}$). The observable quantity in this case then is the time integral of (2.43).

The time dependence of (2.43), from (2.30), may be written as

$$\cos \omega t \; e^{-\gamma t} \tag{2.44}$$

where $\omega = (E_J - E_{J'})/\hbar$ and γ is a mean decay constant, $\gamma = (\gamma_J + \gamma_{J'})/2$ which may be integrated to yield

$$\int_0^\infty dt \cos \omega t \; e^{-\gamma t} = \frac{\gamma}{\gamma^2 + \omega^2} \tag{2.45}$$

where we assume that the instrumental time resolution is much greater than the lifetime of the excited state. For $J = J'$ (2.45) gives $^1/\gamma$ while for hydrogen the case where $J \neq J'$ gives

$$\frac{\gamma}{\gamma^2 + \omega^2} \qquad \frac{1}{\gamma} \; \frac{1}{1 + (^\omega/\gamma)^2} \simeq 0 \tag{2.46}$$

since $\omega >> \gamma$.

Therefore the fine structure beats may be neglected in this case. The angular correlation function for the 2P state of atomic hydrogen may then be obtained from (2.43) giving

$$I(\theta_\gamma)$$

$$= \frac{e^2\omega^4 d\Omega}{2\pi c^3\hbar}\,\frac{\sigma}{3\gamma}\,|\langle 0||\,r\,||\,1\rangle|^2\,\{\tfrac{1}{2}(1 - 3\lambda)\cos^2\theta_\gamma - \tfrac{1}{6}(1 - 3\lambda) - \sqrt{2}R\sin 2\theta_\gamma - \tfrac{1}{2}(1 - \lambda)\sin^2\theta_\gamma\} \qquad (2.47)$$

where σ, λ and R are as defined in (2.12) and (2.47) has been further specialised to the case of observation in the scattering plane, i.e. $\phi_\gamma = \pi$.

Thus a series of measurements of $I(\theta_\gamma)$ over a range of angles θ_γ may yield values for the important parameters λ and R for a particular electron scattering angle. (To obtain a value of I a measurement of the circular polarisation of the emitted light is necessary).

In principle the angular correlation function is also given by (2.43) in the case where an electric field is applied to the excited atoms. The effect of the external field is included in the perturbation coefficients as outlined in the previous section. It was pointed out in the last section that this calculation becomes difficult when the $P_{3/2}$ state is included. To overcome this the following numerical approach was followed.

IV. Decay of Stark Mixed States

Assuming the field plays no role during the collision and Russell-Saunders coupling is valid during the excitation the atoms then relax in to the $J - M_J$ coupling scheme. The field free Hamiltonian may be written in matrix form as

$$H_o = \begin{bmatrix} 0 & 0 & 0 \\ 0 & 1058 & 0 \\ 0 & 0 & 10969 \end{bmatrix} \tag{2.48}$$

where all energies are in MHz and the zero has been taken as the energy of the $P_{\frac{1}{2}}$ state. The eigenstates of the field free Hamiltonian are just the $P_{\frac{1}{2}}$, $S_{\frac{1}{2}}$ and $P_{3/2}$ states. In the presence of the electric field the Hamiltonian is modified according to

$$H = H_o + V \tag{2.49}$$

where $V = e\underline{\varepsilon}\cdot\underline{r}$ is the Stark operator. The Stark matrix elements $V_{ij} = \langle i|e\underline{\varepsilon}\cdot\underline{r}|j\rangle$ may be evaluated for a particular field strength, 250 V cm^{-1} in this case, applied in some direction, the z-direction, to give

$$H = \begin{bmatrix} 0 & 554 & 0 \\ 554 & 1058 & -786 \\ 0 & -786 & 10969 \end{bmatrix} \tag{2.50}$$

This matrix may be diagonalised numerically on a computer to yield new eigenvalues and new eigenstates $|\phi_i^m\rangle$, $i = 1,2,3$, $m = \pm\frac{1}{2}$ in terms of the field free basis states.

$$|\phi_i^m\rangle = a_i^m|P_{\frac{1}{2}}^m\rangle + b_i^m|S_{\frac{1}{2}}^m\rangle + c_i^m|P_{3/2}^m\rangle \quad . \tag{2.51}$$

The $P_{3/2}^m$, $m = \pm\,{}^3/2$ states are of course unaffected since the Stark operator is diagonal in m_J (see Fig. 1). The coefficients are related by the following expressions:

$$\begin{aligned} a_i^m/b_i^m &= -\,\langle P_{3/2}^m|e\varepsilon z|S_{\frac{1}{2}}^m\rangle/(E_{P_{\frac{1}{2}}} - E_i) \\ c_i^m/b_i^m &= -\,\langle P_{3/2}^m|e\varepsilon z|S_{\frac{1}{2}}^m\rangle/(E_{P_{3/2}} - E_i) \quad . \end{aligned} \tag{2.52}$$

Numerical values of the coefficients for $m = \pm \frac{1}{2}$ for a field strength of 250 Vcm^{-1} are given in the table below.

	$\vert\phi_1\rangle$	$\vert\phi_2\rangle$	$\vert\phi_3\rangle$
a_i	0.914 (1)	±0.406(0)	∓0.004(0)
b_i	∓0.405(0)	0.911(1)	-0.079(0)
c_i	∓0.028(0)	0.073(0)	0.997(1)
E_i(MHz)	-246(0)	1242(1058)	11031(10969)

Figures in parenthesis relate to the field free limit. The table shows clearly the strong mixing of the $P_{\frac{1}{2}}$ and $S_{\frac{1}{2}}$ states in forming ϕ_1 and ϕ_2. The weak mixing of the $P_{3/2}$ state is also evident as one would expect since the energy separations between the $S_{\frac{1}{2}}$ state and the $P_{\frac{1}{2}}$ and $P_{3/2}$ states are very different.

The decay rates of the Stark mixed states may be determined by noting that since the decay rate of the metastable $S_{\frac{1}{2}}$ state is negligible compared with that of the P states the ϕ_i^m states may be considered to decay only through their P-component. The decay rate Γ_i^m is then equal to the probability of finding the state in its P-components times the rate of decay Γ_P

$$\Gamma_i^m = \frac{|a_i^m|^2 + |c_i^m|^2}{|a_i^m|^2 + |b_i^m|^2 + |c_i^m|^2} \Gamma_P \qquad (2.53)$$

giving

$$t_i^m = \frac{1 + |a_i^m|^2/|b_i^m|^2 + |c_i^m|^2/|b_i^m|^2}{|a_i^m|^2/|b_i^m|^2 + |c_i^m|^2/|b_i^m|^2} t_p \qquad (2.54)$$

where $t_i^m = (\Gamma_i^m)^{-1}$ is the lifetime of the state or in terms of lifetimes of normalised eigenstates

$$t_i^m = \frac{1}{|a_i^m|^2 + |C_i^m|^2} t_p \qquad (2.55)$$

which is in fact independent of m. $t_p = 1.60\text{ns}$.

The lifetimes of the states ϕ_1 and ϕ_2 are determined mainly by the ratios a_1/b_1 and a_2/b_2 in (2.54), but for ϕ_2 the coupling with the $P_{3/2}$ state is large enough to significantly affect the lifetime of this state (see table). This is the most important consequence of including the coupling to the $P_{3/2}$ state. For the field strength employed in the work reported in this thesis of 250 Vcm^{-1} lifetimes of the states $|\phi_1>$, $|\phi_2>$ and $|\phi_3>$, as given by (2.55) are 1.91, 9.39 and 1.61ns respectively compared with values of 1.60ns, $^1/7$s and 1.60ns in the field free limit. The unperturbed $m_J = \pm\, ^3/2$ levels of the $P_{3/2}$ state decay with a lifetime of t_p.

The state of the atoms immediately after the collision may be written as

$$|\psi> = \sum_{\substack{i=1,2,3 \\ m=\pm\frac{1}{2}}} g_i^m|\phi_i^m> + \sum_{m=\pm\,^3/2} f^m|P^m_{3/2}> \qquad (2.56)$$

Alternatively we may write

$$|\psi> = \sum_{LM} f_{LM}\, Y_{LM}[|\alpha> + e^{i\delta}|\beta>] \qquad (2.57)$$

where f_{LM} are direct scattering amplitudes, exchange processes having been neglected. This is justified since these effects are only expected to be significant at low energies while the work reported in this thesis was carried out at an incident energy of 350 eV (approximately 35 times threshold). The Y_{LM} are spherical harmonic functions and $|\alpha>$ and $|\beta>$ denote the two possible atomic spin states in the usual way. The quantity δ is the relative phase between different spin states. (2.57) thus describes a pure spin state. Since the case of interest is one in which atoms and electrons are initially unpolarised and no analysis of final spin states is performed δ is strictly a random phase factor to be averaged over the atomic ensemble in subsequent calculations.

Equating (2.56) and (2.57) and forming the products $<\phi_i^m|\psi>$ allows the coefficients g_i^m and f^m to be expressed in terms of the scattering amplitudes f_{LM} and the coefficients a_i^m, b_i^m amd c_i^m. For $m = + \frac{1}{2}$ and $m = + {}^3/2$ this procedure gives

$$g_i^{\frac{1}{2}} = b_i^{\frac{1}{2}} f_{00} + (\sqrt{2/3}\, c_i^{\frac{1}{2}} - \sqrt{1/3}\, a_i^{\frac{1}{2}}) f_{10} + (\sqrt{1/3}\, c_i^{\frac{1}{2}} + \sqrt{2/3}\, a_i^{\frac{1}{2}}) f_{11}\, e^{i\delta}) \qquad (2.58)$$

$i = 1,2,3$

$$f^{3/2} = f_{11} \; .$$

(This calculation is included in full in Appendix A.)

Terms including $e^{i\delta}$ when averaged over the atomic ensemble vanish since the state is an incoherent mixture of spin states.

The probability of decay to the $S_{\frac{1}{2}}$ ground state is given by the square of the dipole matrix element

$$P \quad \propto \quad |<1S_{\frac{1}{2}}|e \cdot r|\psi>|^2 \qquad (2.59)$$

The state $|\psi>$ is given by (2.56). The $1S_{\frac{1}{2}}$ ground state consists of the two degenerate magnetic sublevels, $m_J = \pm \frac{1}{2}$. In evaluating (2.59) we must apply the usual quantum mechanical rules regarding the way in which the different possible decay paths are combined. These rules may be stated as follows$^{(41)}$ – (1) for *different* paths to the *same* final state, we add amplitudes and then square the sum, i.e. the amplitudes are combined coherently. This has the consequence that different initial states decaying to the same final state give rise to interference effects or quantum beats. (2) for paths to *different* final states amplitudes are squared and then the individual probabilities summed, i.e. these contributions to the total decay probability are added incoherently and thus do not give rise to interference terms.

Following the above rules we sum incoherently over the two lower states and (2.59) may be written

$$P \propto \sum_{m_1} |\langle 1S_{\frac{1}{2}}^{m_1}|e\cdot r|\psi\rangle|^2 \qquad (2.60)$$

and summing coherently over the upper states

$$P \propto \sum_{m_1} \Big| \sum_{im_2} \langle 1S_{\frac{1}{2}}^{m_1}|e\cdot r|\phi_i^{m_2}\rangle\Big|^2 \qquad (2.61)$$

where i and m_2 must run over $i = 1,2,3$ plus the $m = \pm\, ^3/2$ levels of the $|P_{3/2}\rangle$ state.

Considering first the sum over i. This procedure leads to two types of term. Four terms of the type $Y^2e^{-\gamma t}$ representing the usual exponential decay of $|\phi_1^m\rangle$, $|\phi_2^m\rangle$, $|\phi_3^m\rangle$ and $|P_{3/2}^m\rangle$ states and interference terms of the form $XY \cos \omega t\ e^{-\gamma t}$. The latter category result in the emitted light being modulated in time at a frequency ω determined by the energy difference between the two states involved. In this work the period of even the slowest beats, i.e. the $|\phi_1^m\rangle - |\phi_3^m\rangle$ beat period of ∿ 0.6ns, was shorter than the time resolution of the apparatus and are therefore assumed to average to zero.

The decay of the excited state is then described by the expression

$$I(t) = C_1 e^{-\gamma_1 t} + C_2 e^{-\gamma_2 t} + C_3 e^{-\gamma_3 t} + C_4 e^{-\gamma_p t} \qquad (2.62)$$

where $\gamma_i = {}^1/t_i$, t_i = mean lifetime of the state $|\phi_i>$

and $\gamma_p = {}^1/t_p$, $t_p = 1.60\text{ns}$.

However $t_3 \approx t_p$ (pg 22), we may therefore write

$$I(t) = C_1 e^{-\gamma_1 t} + C_2 e^{-\gamma_2 t} + [C_3 + C_4] e^{-\gamma_3 t} \qquad (2.63)$$

where the coefficients C_i are given by the expression.

$$C_i = \sum_{m_1} \Big| \sum_{m_2} <1S_{\frac{1}{2}}^{m_1}| e \cdot r | \phi_i^{m_2} >\Big|^2 \qquad (2.64)$$

(2.63) may be further expanded in terms of two orthogonal polarisation states of the emitted light $e_\perp$ and $e_{||}$ to give

$$C_i = \sum_{m_1} \Big| \sum_{m_2} <1S_{\frac{1}{2}}^{m_1}|e_\perp \cdot r|\phi_i^{m_2}>\Big|^2 + \Big|\sum_{m_2} <1S_{\frac{1}{2}}^{m_1}|e_{||}\cdot r|\phi_i^{m_2}>\Big|^2 \qquad (2.65)$$

The evaluation of these coefficients is carried out in Appendix A for a field strength of 250 Vcm^{-1}, Photons are assumed to be emitted in the scattering plane at right angles to the incident electron beam. For this case the result is

$$\begin{aligned} C_1 &= K[1.68|f_{00}|^2 + 3.11|f_{10}|^2 + 5.46|f_{11}|^2 + 4.58 \text{ Re } <f_{00}f_{10}^*>] \\ C_2 &= K[1.50|f_{00}|^2 + 0.06|f_{10}|^2 + 0.25|f_{11}|^2 - 0.58 \text{ Re } <f_{00}f_{10}^*>] \qquad (2.66) \\ [C_3 + C_4] &= K[0.09|f_{00}|^2 + 9.96|f_{10}|^2 + 8.00|f_{11}| - 1.93 \text{ Re } <f_{00}f_{10}^*>] \end{aligned}$$

where $|f_{LM}|^2 = \sigma_{LM}$ and K is a constant depending on experimental parameters.

(2.66) shows how the coefficients occurring in the expression for the emitted intensity, (2.62), depend on an interference term, the $S - P$ coherence term, in addition to cross-sections. Finally it should be noted that the above calculation has been carried out neglecting the quantum beat terms.

CHAPTER 3

EXPERIMENTAL

I. Introductory Remarks and Vacuum System

The work described in this thesis was carried out on an existing electron-photon coincidence apparatus(36). For the present work two major modifications were necessary: (1) the facility to apply a highly uniform electric field of a few hundred volts per centimetre to the interaction region and (2) the complete redesign of electron and photon detectors to incorporate micro-channel plates (M.C.P.) instead of channeltrons (C.E.M.) in order to achieve time resolution of the order of half a nanosecond.

This chapter describes the experimental arrangement used, with particular attention being paid to the steps taken to meet the two requirements mentioned above.

A number of problems were encountered in trying to devise a mechanism for applying a uniform field to the interaction region and a satisfactory solution was found only after considerable effort. This is described in Section IV. The various steps taken to achieve subnanosecond time resolution are described in detail in the following sections.

In discussing the time resolution of the apparatus it is useful to follow the analysis of Völkel and Sandner(56) who gave an expression for the different contributions to the time resolution of a coincidence experiment

$$\Delta t = \Delta t_{VOL} + \Delta t_{ENERGY} + \Delta t_{GEOM} + \Delta t_{DET} + \Delta t_{ELEC} \qquad (3.1)$$

Δt_{VOL} is the uncertainty in the particles' transit time due to the finite extension of the interaction volume. In the case of an electron-photon coincidence experiment this term is only of relevance to the electron channel since the photon transit time, and hence transit time spread, is negligible compared to that of the much slower electrons. This term is considered in detail in Section IV.

Δt_{ENERGY} denotes the uncertainty in the transit times of the electrons due to the finite energy resolution of the analyser, while Δt_{GEOM} refers to transit time spread arising from the finite acceptance angle of the analyser. Section V deals with the contributions to the time resolution made by these terms.

Finally, Δt_{DET} and Δt_{ELEC} represent the timing uncertainty due to the detectors and the electronics through which the signals are processed, respectively. These two aspects are of great importance in both electron and photon channels and are covered in Sections V, VI and VII.

Völkel and Sandner point out that not all these contributions are independent and so (3.1) refers to the base width of the time distribution rather than the full-width-half-maximum (F.W.H.M.), which is the quantity which has been taken as a measure of the timing resolution in this thesis. This means that simply summing the contributions in (3.1) does not provide a good estimate of the time resolution. It is clear, however, that the terms occurring in (3.1) should be minimised where possible.

The experimental arrangement is shown in schematic form in Fig. 2. The experiment was housed in a cylindrical stainless steel vacuum tank, 90 cm in diameter by 50 cm high, pumped by an oil diffusion pump with a pumping speed of 700ℓ s^{-1}. This gave background pressures of typically 4×10^{-7} torr. with hydrogen gas flowing into the system. Two sets of μ-metal liners were used to shield against the earth's magnetic field. The residual magnetic field at the interaction region was measured to be less than 30mG. with this arrangement.

II, The Electron Gun

The electron gun is shown in Fig. 3. The cylindrical lens elements were manufactured from non-magnetic stainless steel with molybdenum apertures. The cathode was a tungsten filament, 0.04mm thick by 0.7mm wide, carrying a current of typically 6A.

The gun consisted of three stages. A Pearce diode configuration provided the extraction stage. This was followed by a set of horizontal and vertical deflector electrodes to allow corrections to be made for any mechanical misalignment of the lens system. Elements I, II and III constituted the second stage, an accelerating three element lens to focus the electron beam onto a 0.3mm aperture. Another set of deflector electrodes then allowed the electron beam to be steered to intersect the atom beam. The third stage was a decelerating three element lens, formed by IV, V and VA, which focussed the beam at the interaction region. The final energy of the beam was established by VI, which was normally held at ground potential, the cathode being biased negative with respect to ground. Voltage ratios for the lenses are given in Fig. 3.

The gun was designed to provide beam energies from about 35 eV to a few hundred eV with beam currents of the order of 1 μA, and a cross section of about $1mm^2$.

The study reported in this thesis was carried out using a beam energy of 200 eV.

The angular divergence of the beam was measured to be ± 0.8° (FWHM).

III. Atomic Hydrogen Source

Atoms were produced by dissociating hydrogen molecules in a radio-frequency discharge. The source has previously been described by Slevin and Stirling(57).

The discharge tube, shown in Fig. 4, was constructed from Pyrex since this is one of the few surfaces which exhibits a low recombination coefficient. The tube was 240mm long with a bore of 18mm, terminated at each end by a 2mm capillary in order to contain the discharge. The atoms effuse from the discharge region through a 30mm length of 1mm capillary. The discharge tube was enclosed in a water jacket in order to reduce the discharge temperature and to inhibit recombination at the tube wall(58).

Since the presence of any impurities on the tube wall can greatly increase recombination, great care was taken to ensure that the tube wall was clean. Prior to installation the tube was cleaned by successive washing with hot chromic acid, acetone, HF and distilled water. Once installed the following precautions were taken to minimise the risk of contaminants entering the tube. Hydrogen gas was fed to the discharge using a palladium leak to prevent the flow of contaminants from the gas line, a liquid nitrogen trap was used in the roughing line, during roughing from atmospheric pressure to guard against contamination by pump oil and the pressure in the tube was maintained positive with respect to the scattering chamber whenever possible. With these precautions one tube has provided well over one year of trouble free operation.

The tube was mounted in a small vacuum tank consisting of two 100mm flanges separated by a bellows for alignment purposes, with additional ports for R.F., gas and water feedthroughs (Fig. 5).

The discharge was excited by feeding 10-15 watts of R.F power into a coaxial cavity resonant at about 35 MHz. The cavity consisted of a copper cylinder surrounding the discharge tube and a twelve turn helix of constant pitch (Fig. 4). The cavity and R.F. generator were carefully designed to ensure that most of the power is absorbed in the discharge with less than 10% power reflected. The design of the R.F. generator minimised the propagation of unwanted R.F. signals by employing careful screening of oscillator and driver stages, narrow band amplifying stages and sharply tuned filters. To further reduce any R.F. noise in the system, the discharge tube and cavity were enclosed in a carefully grounded μ-metal shield (Fig. 5).

Despite these precautions however it was discovered that interference from the R.F. was producing structure in the coincidence spectra. This problem was eventually overcome by modulating the R.F. power in conjunction with the time to amplitude converter (T.A.C.) in the following way. The R.F. generator had the facility to have the output switched on and off by means of a +10v pulse. A similar facility on the T.A.C. allowed the R.F. power to be modulated at a frequency of about 1 kHz with a 50% duty cycle, while the T.A.C. was only enabled during that part of the cycle when the R.F. power was off. Using this technique the structure in the coincidence spectra due to R.F. interference was eliminated although at the cost of doubling the integration time.

The dissociation fraction obtained from the source has been measured and reported by Slevin et al.(39). The method employed was to observe the rate of coincidences between scattered electrons and emitted photons as a function of the energy lost by the electrons. The result is plotted in Fig. 6. With the discharge off, a broad peak was observed at an electron energy loss of about 12.9 eV corresponding to the excitation and decay of molecular states. The Franck-Condon factors for the decay of these states allow the wavelength of the corresponding photons to fall within the bandpass of the photon detector. With the discharge on, a large peak occurred at an energy loss of 10.2 eV, corresponding to excitation of the $n = 2$ states of atomic hydrogen, and a much smaller broad peak centred about 12.3 eV was observed, corresponding to excitations of atomic states with $n \geq 3$ and a molecular component. The data shown permit a lower limit of 92% to be put on the dissociation fraction of the source.

The atomic density in the interaction region can be calculated from a knowledge of the relevant dimensions and pressures employed in the source. For the pressures used in this work, typically 10^{-1} torr., this gives a density of the order of 10^{12} atoms cm^{-3}. The gas density in the interaction region is limited by the need to avoid resonance trapping of the Lyman-α radiation(1). Resonance trapping is the absorption of a Lyman-α photon by a ground state atom within the interaction volume. The atom then emits a photon which is correlated in time with the scattered electron and thus gives rise to a coincidence count, but which does not relate directly to the original collision.

This effect may be checked for directly by simply determining the lifetime of the 2P state from the coincidence peak as described in the results section of this thesis. Since resonance trapping results in an apparent increase of the lifetime of the state it is sufficient to determine a pressure region in which the measured lifetime is independent of pressure. The beam produced by the hydrogen source was not well collimated but in fact was highly divergent. This feature is discussed in the next section.

IV. The Interaction Region

The experimental geometry is shown in Fig. 7. The interaction region was formed by the electron and hydrogen atom beams crossing at right angles. Scattered electrons were detected in the plane perpendicular to the hydrogen atom beam, the 'scattering plane'. Lyman-α photons were detected in the scattering plane at right angles to the incident electron beam. A pair of capacitor plates allowed an electric field to be applied to the interaction region parallel to the incident electron beam.

The capacitor plates were manufactured from 1mm thick molybdenum. The electron beam entered through a knife-edged 1mm diameter hole and scattered electrons exited via a 1 × 3mm slot in the second plate. The field plates were mounted on a P.T.F.E. block which located on the top of the hydrogen tube. Since the hydrogen source did not produce a well collimated beam of atoms, it was necessary for the interaction region to be as close as possible to the exit of the hydrogen tube. In order to ensure that collisions took place in a uniform electric field it was necessary to devise a method of screening the interaction region from the nozzle of the hydrogen tube which was fixed at earth potential.

Initially an attempt was made to establish the correct potential distribution by placing a high resistance surface between the plates.

To this end, a P.T.F.E. surface, coated with a suspension of graphite in ethanol, was installed between the plates. The hydrogen beam emerged from a 0.8 mm diameter hole in the centre of the P.T.F.E. block. However, this method did not produce a sufficiently uniform coating and so the P.T.F.E. block was replaced by a ceramic block with the expectation that this might provide a better surface for the application of the conducting layer. A number of techniques were tried in order to obtain a uniform coating. Application by brush and spray both proved unsuccessful, the resulting coatings were highly non-uniform. A thin layer of gold applied in a vacuum coating unit was also tried but obtaining a uniform but sufficiently thin layer proved difficult. A technique used to coat the surface of solid state detectors was used to apply the graphite suspension(59). This technique consisted of suspending the ceramic block in the graphite suspension in a large burette, with the surface to be coated vertical. As the fluid is allowed to slowly drain away, a coating is deposited on the vertical surface, the thickness of the coating being determined by the rate at which the fluid is allowed to drain away. This method proved more successful in obtaining a uniform coating but the resistance of this coating was too low. The Joule heating of the coating due to the relatively large current being drawn, destroyed the surface after a few hours operation.

Since attempts to obtain a uniform resistive surface between the plates met with no success, the field plates were redesigned to incorporate a set of closely spaced grid wires to screen the interaction region from the hydrogen tube nozzle. A number of designs were tried, culminating in that shown in Fig. 8.

In this configuration the field plates consisted of two molybdenum plates, 25 × 30mm by 1mm thick, 12mm apart mounted on a P.T.F.E. block which located on the hydrogen tube nozzle, as before. Again entrance and exit apertures for the incident and scattered electrons were provided by a 1mm diameter hole and a 1 × 3mm slot respectively. In order to improve the collimation of the atomic beam a stainless steel cone, with P.T.F.E. insert, was mounted on the P.T.F.E. block (Fig. 8). The cone was grounded to prevent charge accumulating on it. This arrangement was designed to operate in the following way. Since P.T.F.E., unlike metals, possesses a low recombination coefficient for atomic hydrogen, atoms passing through or striking the P.T.F.E. insert do not recombine and diffuse out to the interadion region. Atoms which strike the metal cone are more likely to combine to form molecules which are then pumped away via the four holes in the cone wall.

In order to minimise any non uniformities introduced by the grounded atomic beam collimator or fringing fields at the plate edges a set of grid wires, spaced 1mm apart, surrounding the region between the plates was incorporated as shown (Fig. 8). The grid consisted of ten 0.1mm diameter gold wires spotwelded onto stainless steel washers mounted on ceramic rods between the plates. The steel washers were insulated from one another by 0.1mm thick mica washers. The correct potential was established on each wire by means of a resistance chain.

The data relating to the Stark mixing coefficients were obtained using the set of plates described above, operated with the entrance plate at ground potential and the exit plate at +300V, giving an electric field strength of 250Vcm^{-1}. Electrons entered the field region at the energy of 200 eV and so collisions took place at an energy of 350eV. The finite size of the interaction region, however, estimated to be 2 - 3mm in the direction of the electric field, resulted in an uncertainty of about ±(25 - 37)eV in the collision energy.

The presence of the electric field introduced the further complication that scattered electrons leaving the interaction region followed parabolic trajectories. This effect was taken into account and is dealt with in Chapter 5.

An estimate of the uniformity of the electric field throughout the interaction volume was obtained using a numerical method described by Grossberg(60). The result showed the field to be uniform to better than 1% throughout the interaction volume.

In an attempt to further improve the time resolution, by reducing the contribution Δt_{VOL} in equation (3.1), it was decided to install a mask between the photon detector and the interaction region to limit the linear extent of the effective interaction region to 1mm. It was estimated that this reduction in size of the interaction region would reduce Δt_{VOL} from 0.3ns to approximately 0.1ns. It was clear from the results that Δt_{VOL} was a significant contribution, as evidenced by the fact that the time resolution was a function of electron scattering angle. It was not possible to modify the existing set of field plates to incorporate a mask and it proved necessary to redesign the entire field plate assembly. The new set of plates incorporated a 0.4mm wide slit to limit the field of view of the photon detector. With these plates installed a beat pattern was observed.

In addition to the Stark measurements, the parameters λ and R were determined for the field free case by making angular correlation measurements. For these measurements the field plates themselves were removed, leaving the atomic beam collimator. In order to ensure a similar electron beam geometry a 1mm diameter knife-edged electron beam collimator was installed at the same location as the entrance field plate had been.

V. The Electron Detector

Scattered electrons were analysed and selected for the appropriate energy loss and detected using a microchannel plate detector.

A set of optics focussed scattered electrons onto the entrance slit of the analyser which consisted of two 127° cylindrical electrostatic analysers in series. A further set of optics then focussed the energy selected electrons onto the microchannel plate detector. This arrangement was mounted on a belt driven turntable, allowing it to be rotated in the scattering plane about the atomic·beam.

Va. Electron optics

The input electron optics consisted of six elements (Fig. 2). The design and construction of these elements has been described by Mazeau(61). The lens elements were constructed from Arcap, mounted on four ceramic rods and insulated from one another by thin pieces of mica.

Elements V1, V2 and V3 formed a three element aperture lens of the type described by Read(62). V4 and V5 were split, horizontally and vertically respectively, to allow scattered electrons to be steered onto the entrance slit of the energy analyser. VO acted to shield the interaction region from the potentials applied to the lens elements, while the cone prevented stray electrons, i.e. electrons other than those scattered from hydrogen atoms, entering the detector. The cone defined the geometric solid angle of the detector which was typically 2×10^{-2} sr.

Voltage ratios for the three aperture lens are given in Read(62). However, in practice, all elements were operated with a view to optimising the time resolution and not necessarily maximising the scattered electron count rate. Voltage ratios were determined on a trial and error basis by examining the time resolution of the apparatus for various applied voltages. In general it was found to be desirable to operate all elements at as high a potential as possible in order to minimise electron transit times and hence transit time spreads.

The output optics were of similar design, consisting of a two aperture lens followed by two split steering electrodes. As for the input optics operating voltages were determined empirically for optimum time resolution.

Vb. Energy analyser

Scattered electrons were energy selected for the appropriate energy loss, 10.2 eV corresponding to excitation of the $n = 2$ level of atomic hydrogen, using two 127° cylindrical electrostatic analysers operated in series (Fig. 2). The construction of the analysers has been described by Mazeau(61). Two 127° sectors were used rather than one in order to provide the increased discrimination against the unscattered electron beam necessary to get into small electron scattering angles. The two analysers also gave a more convenient mechanical arrangement.

The analyser was operated in a low energy resolution mode since the atomic $n = 2$ energy loss and that of the nearest inelastic channel were separated by about 2 eV. Any contribution to the coincidence signal arising from scattering channels other than $n = 2$ atomic states was checked for directly in the following way. A coincidence spectrum was collected with the R.F. power to the hydrogen source switched off and the energy analyser tuned to the $n = 2$ atomic energy loss. No significant coincidence signal was observed, suggesting that any molecular component was negligible. The mode of operation of the analyser was therefore mainly determined by the need to minimise the contributions Δt_{ENERGY} and Δt_{GEOM} in equation (3.1).

The term Δt_{ENERGY} arises from the fact that electrons transmitted by the analyser have a finite spread in energy and therefore in transit times. It is therefore desirable to operate with high energy resolution from the point of view of minimising this term. To this end the input, intermediate and output slits of the analyser were reduced to 0.4mm from their initial values of 0.4mm, 1.0mm and 0.5mm respectively. The reduction in slit sizes was limited by the need to maintain a sufficiently large electron count rate to avoid prohibitively long integrating times.

Δt_{GEOM} arises from the different paths around the analyser followed by monoenergetic electrons which enter at different angles. The resulting spread in transit times depends therefore on the angular divergence of electrons entering the analyser and the total transit time around the analyser. The first of these factors will depend on the operation of the input electron optics in this case and has therefore been dealt with in the last section. The second factor suggests that the analysis energy, E_o, should be large.

It was observed that the time resolution improved as E_o was increased. However, increasing E_o degrades the energy resolution and thus the maximum permissible value of E_o was limited by the need to retain some discrimination against the molecular states lying about 2 eV above the $n = 2$ atomic states in energy. The optimum value of E_o was found to be 135 eV.

Völkel and Sandner(56) describe a method of reducing Δt_{GEOM} by placing the microchannel plate detector at an angle to compensate for the different transit times round the analyser. This technique is not, however, applicable in this case since the trajectories of the transmitted electrons are altered by the output optics.

Vc. Microchannel plate detector

Electrons having lost the appropriate energy were detected by a microchannel plate detector (Fig. 2). A microchannel plate is an array of 10^4 - 10^7 miniature electron multipliers oriented parallel to one another. Channel diameters are usually in the range 10 - 100μm with length to diameter ratios between 40 and 100. The channels are inclined at an angle to prevent transmission of the incident beam. The array of channels is made from a semi-conducting lead glass and so each channel may be considered to act as a continuous dynode structure which acts as its own dynode resistor chain. Nichrome or inconel on front and rear surfaces act as input and output electrodes(63).

Microchannel plates are now widely used to detect both charged particles and photons. They exhibit high gain, 10^4 typically per plate, very low 'dark' count rates, long useful life and of particular importance for this study, excellent timing characteristics. Transit time variations of the charge cloud inside the multiplier, Δt_{DET} in equation (3.1), for M.C.P. have been found to be less than 150ps compared with 2 - 3ns for single channel electron multipliers(64).

The M.C.P. detector is shown in Fig. 9. It consisted of three microchannel plates cascaded in a chevron arrangement, discussed in more detail later, and a matched 50Ω conical anode also discussed later. The plates were housed in P.T.F.E. with copper electrodes permitting the application of the plate potentials. The outer cone of the anode was made from stainless steel, while the central collector was copper, to allow it to be soldered into the 50Ω connector This assembly was housed in an aluminium box. Two fine mesh grids were positioned as shown in front of the plate assembly. The first grid was grounded and simply acted to screen the output optics from the M.C.P. The voltage on the second grid, labelled V_T in Fig. 9, could be varied externally as could V_{CH}, the voltage on the front of the first M.C.P. for reasons discussed later. Both grids were 10mm in diameter to reduce the effective size of the M.C.P. used to that of the central collector of the conical anode. A resistance chain housed in a separate box within the vacuum system established the correct potentials on the M.C.P. and collector. High voltage, typically 1000v per plate and a plate-collector voltage of 500v, was supplied by a Nuclear Enterprises high voltage supply type NE4701.

The M.C.P. used in the detector were of two similar types, Mullard G12-25SE and Varian 8900CAH. Both types are 0.5mm thick by 25mm in diameter with a nominal channel diameter of 12μm and a channel spacing (centre to centre) of 15μm. The open area of the plates was about 60% with a useful diameter of approximately 19mm. The Mullard plates have a channel bias angle of 8° and a gain of typically 5×10^3 at 1000v, while the Varian plates have a channel bias angle of 5° and exhibit a higher gain of 2×10^4 at 1000v.

Coincidence spectra obtained in the early stages of this study, with zero electric field applied to the interaction region, exhibited structure in what should have been a single exponential decay. In an attempt to discover the cause of this structure the nature of the pulses from the M.C.P. detector was investigated.

Three effects which could give rise to badly shaped pulses from the M.C.P. detector were considered.

Firstly, 'positive ion feedback' can produce spurious pulses(63). Ion feedback is caused by the production of positive ions within the channels by cascading secondary electrons colliding with residual gas molecules. These ions are then accelerated by the plate voltage. This process can lead to 'after pulsing' which can become a serious problem at higher gains since the ions are more likely to obtain sufficient energy to produce spurious pulses. It is this effect which limits the gain of a single M.C.P. to about 10^4. In order to overcome this problem, two plates are normally used coupled in cascade with the second plate being rotated through 180° with respect to the first to form a chevron arrangement (Fig. 9). This arrangement allows gains of 10^8, or more depending on how many plates are cascaded, to be achieved without encountering problems due to ion feedback. A more recent approach to tackling this problem has been the development of M.C.P. in which the channels are curved(65).

Originally a chevron arrangement of two Varian 8900CAH plates were used in the electron M.C.P. detector but a third plate, a Mullard G12-25SE, was later added. This served the dual purpose of allowing each plate to be operated at a lower gain, thus reducing the possibility of ion feedback occurring, and also permitted the elimination of the pulse amplifiers to investigate the possibility that these may have been limiting the time resolution.

Structure on the coincidence spectrum can also arise from 'ringing' on the electron signal cable. This effect is a problem which can be encountered with any type of detector. It is caused by multiple reflections of the output pulse by impedance mismatches on the output cable. If the counting circuitry is triggered on the leading edge of the original output pulse then the dead time of the electronics ensures that any subsequent ringing will not produce a count in the electron channel. If, however, for any reason the counting circuitry does not trigger on the leading edge of the original pulse, and if the ringing is of sufficient amplitude, then an electron count may result from the circuitry triggering on one of the reflected pulses. The reflected pulses will clearly have a different timing to original pulses, thus leading to structure in the coincidence spectrum.

Observation of the pulses from the M.C.P. detector using a fast oscilloscope revealed large amplitude ringing on the signal line. In an attempt to reduce this ringing the original flat metal plate collector was replaced by a co-axial anode designed to be impedance matched to the 50Ω signal cable. Details of the design are given in Wiza(63). This modification did significantly reduce the amplitude of the ringing but did not entirely eliminate the structure in the coincidence spectrum.

Finally a feature which is specific to M.C.P. was investigated. Electrons incident on the face of the M.C.P. may be regarded as consisting of two groups, those that enter a channel and produce a secondary electron cascade, and those that strike the area between channels, also giving rise to secondary electrons. In the interests of efficiency it is normal practice to establish an electric field in front of the M.C.P. such that all secondary electrons produced by this second group are accelerated back towards the M.C.P. Hence the inclusion of the grid V_T (Fig. 9). In this way all secondary electrons produced will produce an output pulse. However, these two groups of electrons produce pulses with different characteristic timing and thus may result in structure in the coincidence spectrum.

This effect was investigated by varying the potential V_{CH} while keeping V_T at ground. It was found that with V_{CH} a few hundred volts negative with respect to ground, a single coincidence peak without structure was observed. As V_{CH} was increased beyond ground potential a second coincidence peak, increasing in amplitude as V_{CH} increased, appeared in the coincidence spectrum. The two peaks were separated in time by about 7ns. It was therefore decided to operate the plates with V_T at ground potential and V_{CH} at about -170v with respect to ground. This mode of operation of course resulted in the electron count rate being reduced by about 50%.

In addition to the effects discussed above, it was found that the voltage between the last M.C.P. and the anode was important in obtaining a good pulse shape. On reducing this voltage from 1000v to 250v the pulse shape, and the time resolution, improved significantly.

Typical electron count rates occurring in the work reported in this thesis were 1 - 2 kHz.

VI Photon Detector

Lyman-α photons were detected using a M.C.P. detector of similar design to the electron detector (Fig. 10). The photon detector was mounted on a turntable, allowing it to be rotated in the scattering plane about the atomic beam. The turntable was belt-driven from a stepping motor which could be controlled by computer. The detector consisted of a LiF window, 6mm thick, sandwiched between two grounded fine mesh grids to prevent charging, followed by another fine mesh grid, V_k in Fig. 10, as in the electron detector. The M.C.P., the housing and the matched 50Ω co-axial anode were all identical to those used in the electron detector. The front surface of the first M.C.P. had a coating of CsI, evaporated on using a vacuum coating unit, to act as a photocathode. The bandwidth of the detector was thus determined by the short wavelength cut-off of the LiF window(66), about 105nm and the long wavelength limit of the CsI(66), about 250nm.

The discussion in the previous section with regard to pulse shape is of relevance to the photon detector as well. Similar precautions were taken with the photon detector to ensure good pulse shape, i.e. co-axial anode and the use of three cascaded M.C.P. However the situation with the electric field in front of the M.C.P. was somewhat different in this case. It was found that applying a field to accelerate all secondary electrons back towards the M.C.P.

did not in this case adversely affect the timing or the shape of the coincidence peak. In practice the grid, V_K, was operated at a potential of -400v with respect to ground while the front of the first M.C.P. was operated at ground potential. This result may be understood in the following way. Firstly, the CsI photocathode was applied in such a way as to prevent any significant amount entering the channels themselves. Since the uncoated glass is of very low efficiency at this wavelength, typically less than 1%, it may be assumed that the majority of pulses arise from photons striking the surface between channels. Secondly, the fact that photons and not electrons were being detected in this case meant that a much larger field could be applied thus reducing any timing differences between the two groups.

Typical count rates were of the order of 10 kHz.

VII <u>Electronics</u>

Pulses from the electron and photon detectors were processed using conventional fast electronics (Fig. 2).

Initially output pulses were fed into a preamplifier, a Lecroy W100B wideband pulse amplifier with a gain of ten and risetime of less than 2ns. These were later eliminated in order to ensure that the fast rise time pulses from the M.C.P. were not being distorted, thereby limiting the time resolution. Pulses were then fed directly to a set of Ortec AN302/NL Quad D.C. non-inverting amplifiers, bandwidth 300 MHz and a gain of four. Two stages of amplification were used for both electron and photon pulses. At one stage these amplifiers were also eliminated to ensure that they were not limiting the time resolution but were then reinstalled as it was clear that this was not the case. The amplified pulses were then fed into constant fraction discriminators (C.F.D.). The adjustment and performance of these units proved to be critical in obtaining good time resolution. A great deal of work was done in this area and this is discussed in detail below. Outputs from the C.F.D. were fed into an Ortec 467 time to amplitude convertor (T.A.C.). The voltage ramp of the T.A.C. was started by the pulses from the electron detector and stopped by the pulses from the photon detector, suitably delayed. The T.A.C. output was recorded on a Canberra FT8100 multi-channel analyser (M.C.A.). The M.C.A. was interfaced to a D.E.C. P.D.P.11 computer, allowing coincidence spectra to be transferred and stored on disk for analysis.

Constant fraction discriminators were used in order to eliminate timing variations which arise from input pulses of varying amplitude and rise time. Fig. 11 illustrates the way in which two pulses of differing amplitude and rise time will generate identical timing responses from the C.F.D. The input pulse is split, one part being delayed, the other attenuated. These two signals are then furnished to the inputs of a differential amplifier. The C.F.D. output is triggered when the differential amplifier output changes polarity, i.e. when the amplitude of the delayed pulse equals a preset fraction, 30% in this case, of the attenuated pulse as shown in Fig. 11.

The operation of the C.F.D. can be monitored in two ways. Firstly the output of the differential amplifier may be observed directly on a fast oscilloscope and the variation in time of the 'zero-crossover' monitored. This variation, the 'time-walk', may then be adjusted for a mininum via an external adjustment to the walk compensation network.

Alternatively, the arrangement shown in Fig. 12 may be used. An input pulse is split and applied to the inputs of the two C.F.D., the output of one going to start the T.A.C. while the other output is delayed and used to stop the T.A.C. The T.A.C. output may then be observed on the M.C.A. This technique does not measure the 'time-walk' of the C.F.D. as in the previous case but rather the timing uncertainty due to the combination of electronics forming the coincidence circuitry. This technique therefore is of great use since if real electron or photon pulses are input, information is obtained on the timing uncertainty arising from the operation of the M.C.P. detectors and associated electronics. It thus provides an effective measure of $\Delta t_{DET} + \Delta t_{ELEC}$ in equation (3.1).

In particular the problem of poor pulse shape manifested itself very clearly using this technique. It was found that the pulses from the electron M.C.P. detector gave rise to signals with two distinct characteristic timings. This result can only arise from the C.F.D. being triggered on different parts of the input pulse. Careful adjustment of the C.F.D. and the measures taken to improve the pulse shape described in Section V eliminated this effect. With this problem overcome and the C.F.D. adjusted, timing variations arising from the operation of the M.C.P. detectors and the electronics of less than 300ps and 500ps was achieved for photon and electron pulses respectively.

The data reported here were obtained using Ortec 473 C.F.D. In later work a more recent model, the 934 Quad C.F.D., was used and with this a significant improvement was achieved. Using the method described above Δt_{DET} and Δt_{ELEC} was found to be reduced to 150ps and 250ps for photon and electron channels respectively. The decay curve shown in Chapter 5 with the beat pattern visible was obtained using the 934 Quad C.F.D.

CHAPTER 4

DETERMINATION OF λ AND R

The experimental data were in the form of a pulse height spectrum from the T.A.C. collected on the M.C.A. The typical form of such a coincidence spectrum is shown in Figure 13. The procedure for the collection of data and the subsequent analysis of the coincidence signal are described below.

I. Angular Correlation Measurements

In order to determine the parameters λ and R from equation (2.47) it was necessary to determine the photon count rate arising from the spontaneous decay of atoms which have scattered electrons into a particular direction θ_e as a function of θ_γ, the direction of the emitted photons. By detecting electron-photon pairs in coincidence the desired quantity is the coincidence rate as a function of θ_γ.

The coincidence spectrum of Figure 13 consists of a peak resting on a background. The background, arising from chance coincidences, is in fact a decaying exponential rather than uniform. This is due to the statistical nature of the operation of the T.A.C. It can be shown the background is of the form(67)

$$B(t) = Ke^{-\dot{N}_\gamma t} \tag{4.1}$$

where K is a constant depending on experimental parameters and $\dot{N}_\gamma$ is the photon count rate. For the measurements reported in this thesis the photon count rates and time window were such that the factor $e^{-\dot{N}_\gamma t} \approx 1$. This effect may therefore be neglected and the background is assumed to be uniform in the following analysis.

The number of real coincidences was determined from a coincidence spectrum (Fig. 13) according to

$$N_{real} = I_B - \frac{\Delta t_B}{\Delta t_A} I_A \qquad (4.2)$$

where $I_{A(B)}$ = total number of counts in area A(B)

$\Delta t_{A(B)}$ = width of area A(B).

The rate of real coincidences, $\dot{N}_{real}$, will be sensitive to small variations in electron beam current, target density and electron detector efficiency. To overcome this $\dot{N}_{real}$ was normalised according to

$$\eta = \frac{\dot{N}_{real}}{S} \qquad (4.3)$$

where S is the total number of start pulses received by the T.A.C. which successfully initiated the T.A.C. ramp. Since the quantity S itself is directly proportional to electron beam current, target density and electron detector efficiency the normalised coincidence rate, η, will be independent of any small fluctuations in these quantities. η will of course still be sensitive to any changes in the efficiency of the photon detector. This point is discussed later.

From equations (4.2) and (4.3) and assuming that Poisson statistics apply, the statistical uncertainty in η may be written as

$$\sigma = \frac{\sqrt{I_B + \left(\frac{\Delta t_B}{\Delta t_A}\right)^2 I_A}}{S} \qquad (4.4)$$

The determination of η as a function of θ_γ for a given electron scattering angle θ_e was performed under computer control. η was measured at six values of θ_γ covering a range of approximately 90°. Since η depends on the efficiency of the photon detector short integration times, typically ten minutes, and repeated scans of the photon detector were employed in order to minimise the effect of any variations in detector efficiency. Total integration times ranged from a few hours at small electron scattering angles to about forty hours at large scattering angles.

The parameters λ and R were obtained by fitting equation (2.47) to the data using a non-linear least squares fitting procedure. A standard routine from the N.A.G. library was used to do this. A χ^2 test was performed to measure the quality of the fit. Typical values of χ^2 for the data reported here were in the range 40 – 70%.

λ and R were determined in this way at incident energies of 100 eV and 350 eV for $0° < \theta_e < 15°$ and $0° < \theta_e < 8°$ respectively.

II. Results

Figures 14 and 15 show two typical angular correlation curves recorded at incident electron energies of 100 eV and 350 eV and electron scattering angles of 10° and 6.4° respectively. The full curves represent least square fits of equation (2.47).

Figures 16 and 17 show the parameters λ and R respectively as a function of electron scattering angles at an incident electron energy of 100 eV. Also shown are various theoretical predictions for these parameters. The data for the λ parameter is clearly in excellent agreement with all these predictions except the On-Shell-Fadeev-Watson

(O.S.F.W.) calculations of Fargher(68). This disagreement is not surprising since this approximation is expected only to be accurate in the region of high momentum transfer. The present data also agree well with the data of Hood et al.(34). The deep minimum in λ observed at $\theta_e = 10°$ by Slevin et al.(36) was not observed. The very low value of λ observed by Slevin et al. may be attributed to the presence of resonance trapping. In the case of the R parameter the agreement is not particularly good with any of these calculations and it is not possible to distinguish between the theoretical curves shown on the basis of the present data.

The same parameters, measured at an incident energy of 350 eV, are shown in Figures 18 and 19. Shown on the same figures are the predictions of a distorted wave second Born calculation of Walters(70) and in the case of the λ parameter an O.S.F.W.(71) calculation of Fargher and Roberts. Both theories disagree markedly with the data. Again the disagreement with the O.S.F.W. calculation is not surprising at these small electron scattering angles but significantly the Second Born approximation is expected to perform well at such high energies. This approximation does not agree well with the data for the R - parameter.

III. Error Analysis

One potential source of error in the determination of λ and R is resonance trapping of the Lyman-α radiation. Assuming that resonance trapped radiation is emitted isotropically, the effect would be to 'flatten out' the angular correlation curve. The degree of resonance trapping was therefore checked for by selecting θ_γ for a maximum in the angular distribution, since this effect will clearly be more pronounced at a maximum or minimum, and recording the normalised coincidence rate η as a function of target density. Figure 20 is a plot of η versus the hydrogen gas pressure in the source. It can be seen that η is constant up to a pressure of about 1.5×10^{-1} torr. and then begins to decrease as the degree of resonance trapping becomes significant. All data reported here were obtained using a source pressure of about 1.2×10^{-1} torr.

The effect of the finite acceptance angles of the electron and photon dectectors must also be considered. The finite acceptance angle of the electron detector means that the experimentally determined values of λ and R must be considered to be averaged over the small range of scattering angles accepted by the detector. For the case of the angular correlation measurements reported here the acceptance angle of the electron detector was approximately 1°. The effect of the finite acceptance angle of the photon detector can be taken into account exactly in principle by integrating equation (2.47) over the circular aperture of the photon detector. This calculation has been performed by Eminyan et. al.(19) for the case of the 2^1P state of helium. This effect can be of importance when angular distributions with deep minima are being measured as is the case for the 2^1P state of helium. However the presence of the fine structure interaction in atomic hydrogen reduces the amplitude of the variations in η and thus the effect of the photon detector acceptance angle will be less than for helium.

The recorded angular correlation curves would also be sensitive to photons of the correct wavelength being detected after being scattered from nearby surfaces. However the fact that reflection coefficients at this wavelength are small and the quality of the fit of the data to equation (2.47) suggest that any effect of this kind must be very small.

Spurious electronic noise would also affect the observed coincidence rates. The uniformity of the background of random coincidences indicates that such contributions were not significant.

Finally, it was noted in Section I that the normalised coincidence rate is dependent on the efficiency of the photon detector. The data collection procedure outlined in Section I should reduce the effect of any long term variations in detector efficiency. The reproducibility of the data and the quality of the fits to equation (2.47) are a strong indication that no significant drift in detector efficiency occurred.

CHAPTER 5

STARK FIELD MEASUREMENTS

Equation (2.63) describes the time dependence of the light intensity emitted in the direction θ_γ by those atoms having been excited to the $n = 2$ level by electrons which have been scattered in the direction θ_e. It is therefore possible to determine the coefficients C_i by establishing the coincidence rate as a function of time for a given θ_e and θ_γ. The following sections describe the form of the coincidence signal and the analysis necessary to obtain values of these coefficients.

I Form of the Coincidence Signal for a Single Decay

A single exponential decay may be described by

$$\begin{aligned} I(t) &= 0 && (t < 0) \\ &= \gamma^{-1}\exp(-\gamma t) && (t \geq 0) \end{aligned} \tag{5.1}$$

where the time of excitation has been taken as $t = 0$, and γ, the decay constant, is given by τ^{-1} where τ is the mean lifetime of the decay. The observed form of the coincidence signal as a function of time arising from such a decay, $Y(t)$, will be given by the convolution of (5.1) with the prompt resolution curve, $P(t)$, of the apparatus(72)

$$Y(t) = \int_{-\infty}^{\infty} P(t - t')I(t')dt' \quad . \tag{5.2}$$

Assuming $P(t)$ to be of Gaussian form(73)

$$P(t) = \frac{h}{\sqrt{\pi}} \exp(-h^2t^2) \tag{5.3}$$

where $h = \frac{1}{\sigma\sqrt{2}} = \frac{1}{\text{F.W.H.M.}}$ and σ is the standard deviation, (5.2) may be evaluated to yield

$$Y(t) = B + C(1 + \text{erf}[h(t-t_o) - {}^{\gamma}/2h])\exp({}^{\gamma^2}/4h - \gamma[t-t_o]) \tag{5.4}$$

where erf(x) is the normalised error function, the excitation has been assumed to take place at $t = t_o$ and the background of random coincidences B, assumed to be uniform, has now been included.

Equation (5.4) gives the form of the coincidence signal observed in the case of the excitation and decay of the $n = 2$ level of atomic hydrogen in the absence of external fields. By fitting (5.4) to the coincidence spectra, using a suitably adapted version of the routine mentioned in the last chapter, values of the background B, the amplitude C, the time of excitation t_o, the F.W.H.M. of the apparatus function and the lifetime γ^{-1} were obtained.

Determination of the lifetime of the decay in this way provided a check for the possible presence of resonance trapping as described in Chapter 3. The F.W.H.M. of the Gaussian apparatus function was taken as a measure of the instrumental time resolution. A χ^2 test established that the spectrum was free from any systematic structure.

II Form of the Coincidence Signal for a Three Exponential Decay

In the case where an electric field is applied to the interaction region the expression for I(t) with $t \geq 0$ in (5.1) must be replaced by (2.63) resulting in two additional terms occurring in the expression for Y(t)

$$Y(t) = B + \sum_{i=1,2,3} [D_i(1+\mathrm{erf}[h(t-t_o) - \gamma_i/2h])\exp(\gamma_i^2/4h^2 - \gamma_i[t-t_o])] \tag{5.5}$$

Initially it was attempted to extend the fitting routine to this more complicated expression to obtain values for the nine parameters, B, t_o h, D_i and γ_i. This approach was not successful and the process did not converge. It was therefore decided to fix the three lifetimes at their theoretical values predicted by equation (2.54). For a field strength of 250V cm^{-1} this gave $t_1 = 1.91$ns, $t_2 = 9.39$ns and $t_3 = 1.60$ns. It was then possible to fit values of B, t_o, h and the coefficients D_i to the data. However since the lifetimes t_1 and t_3 are not very different the coefficients D_1 and D_3 could not be obtained with any reasonable degree of accuracy, i.e. there were many combinations of D_1 and D_3 which produced a good fit. The sum $(D_1 + D_3)$ could however be obtained to sufficient accuracy.

The quantities D_2 and $(D_1 + D_3)$ were determined for five different electron scattering angles in the range $1° < \theta_e < 6°$ at an incident electron energy of 350 eV and an electric field strength of 250V cm^{-1} applied parallel to the direction of the incident electron beam. All spectra were obtained for $\theta_\gamma = 90°$. The photon detector angle was restricted to this one value by the geometry of the interaction region. Typical integration times varied from about six to twelve hours.

The quantities D_2 and $(D_1 + D_3)$ are unnormalised in the sense that they depend on experimental parameters such as electron beam current, target density etc. They were therefore normalised to the total area under the coincidence peak Y. This was determined by subtracting the fitted value of the background B from each channel over a time interval chosen such that the decay was 98% complete to give the new quantities

$$R_2 = \frac{D_2}{Y} t_p$$

$$R_{13} = \frac{D_1 + D_3}{Y} t_p \tag{5.6}$$

where t_p is the field free lifetime of the P state.

To facilitate the comparison of the experimentally determined quantities, R_2 and R_{13}, with various theoretical predictions the expression (2.63) was normalised to the total transition probability $\mathbb{P}$, given by

$$\mathbb{P} = \int_0^T I(t)dt \tag{5.7}$$

where T is the total time of observation. Taking T large compared with t_2 (5.7) may be evaluated to give

$$\mathbb{P} = C_1t_1 + C_2t_2 + (C_3+C_4)t_3 \quad . \tag{5.8}$$

It is possible to define the dimensionless parameters

$$\begin{aligned} M(t) &= \frac{I(t)t_p}{\mathbb{P}} \\ &= \frac{C_1e^{-t/t_1} + C_2e^{-t/t_2} + (C_3 + C_4)e^{-t/t_3}}{C_1 \, t_1/t_p + C_2 \, t_2/t_p + (C_3 + C_4)} \\ &= M_1e^{-t/t_1} + M_2e^{-t/t_2} + M_3e^{-t/t_3} \end{aligned} \tag{5.9}$$

The quantities R_2 and R_{13} must of course be considered to be averaged over the angular acceptance of the electron detector. For this set of measurements the electron detector was much closer to the interaction region resulting in a geometric acceptance angle of ±3.5°. This was in fact increased by the effect of the electric field on the trajectories of the scattered electrons to give an effective acceptance angle of approximately ±4°. The effect of the electric field on the electron trajectories was calculated and is given in Appendix B. The quantities M_2 and M_{13} $(= M_1 + M_3)$ were averaged over the appropriate angular range to permit direct comparison with the experimentally determined values of R_2 and R_{13}.

III. Results

Figure 21 shows a coincidence spectrum recorded with zero electric field. The full curve is a least squares fit of equation (5.4) to the data. The lifetime obtained from the fit was 1.61 ± 0.03ns in excellent agreement with the accepted value of 1.60ns (55). The F.W.H.M. of the apparatus function was 1.08 ± 0.03ns for the curve shown. The F.W.H.M., which is a measure of the apparatus time resolution, varied in the range 1.1 - 0.6ns as the electron scattering angle varied from 1.5° to 5.5°. This figure may be compared with the best previously reported time resolution of 3ns (35). The systematic improvement in time resolution may be attributed to geometric factors, the main contribution being the reduction in the effective size of the interaction region as θ_e increases.

Figure 22 shows a coincidence spectrum obtained with an electric field of 250V cm^{-1} applied to the interaction region. The full curve represents a least squares fit of equation (5.4) with a fixed lifetime of 1.60ns. It is clear that the decay contains elements with lifetimes greater than 1.60 ns.

On fitting the data in Figure 22 to equation (5.5) a much better fit was obtained. The value obtained for the F.W.H.M. was 0.58 ± 0.02ns.

The values of F.W.H.M. obtained with an electric field applied were consistently smaller than those for the corresponding field free case. This is not surprising since the electric field will accelerate the scattered electrons away from the interaction region thus reducing their transit times and hence transit time spreads. Again the values obtained for the F.W.H.M. showed a systematic improvement with increasing electron scattering angle, varying from 0.82 - 0.57 ns as θ_e varied from 1.5° to 5.5°.

Values of R_2 and R_{13} and various theoretical predictions of M_2 and M_{13} are given in Table 1. These quantities are plotted against mean electron scattering angle in Figures 23 and 24. Both parameters are in excellent agreement with distorted wave second Born calculations of Walters(70) with the exception of one point for R_2 at $\theta_e = 3.3°$. The agreement for both the Fadeev-Watson(71) and the plane wave second Born(71) calculations is quite poor. In the case of the Fadeev-Watson calculation this is not surprising at such small electron scattering angles. In the case of the second Born calculations the data strongly suggest that it is necessary to include distorted waves to obtain agreement.

The quantities M_2 and M_{13} were evaluated for direct scattering amplitudes and the case where the possibility of exchange processes is included. The results were not significantly different, confirming that the assumption made in Chapter 2, that exchange processes may be neglected, is a reasonable one.

Figure 26 shows a decay curve recorded with an electric field of 250V cm^{-1} applied to the interaction region. This curve was obtained with the modified set of field plates described in Chapter 3. There is clear evidence of periodic structure in the decay. The period of this structure of approximately 0.6ns in is reasonable agreement with the predicted value of the period of the $\phi_1 - \phi_2$ beat pattern of 0.67ns The data shown however was not of sufficient quality to permit a quantitative analysis of the beat structure.

IV Error Analysis

The potential sources of error discussed in Chapter 4 also apply to the Stark field measurements.

The value of 1.61ns obtained for the lifetime of the decay in the field free case suggests that no significant degree of resonance trapping occurred.

The effect of the finite acceptance angle of the electron detector again means that the experimentally determined quantities R_2 and R_{13} must be considered to be averaged over the range of scattering angles accepted by the detector. This effect was taken into account in comparing the results with theory as discussed in Section II.

The effect of the acceptance angle of the photon detector on the results has not been included. In principle, this could have been done in a manner similar to that mentioned in Section III of Chapter 4. However the method of calculation in this case was not particularly amenable to performing the necessary integration. Because of the flatness of the angular correlation function, mentioned in the last chapter, it is unlikely that the finite acceptance angle of the photon detector could affect the results significantly.

The results would also be affected by any sources of stray coincidences but for the data presented here the quality of the fits to the calculated shape of the coincidence signal suggest that any such effects must be small.

V Determination of the Relative Phase of f_{10} and f_{00}

The relative phase of the amplitudes f_{10} and f_{00}, δ, may be obtained by determining the phase of the quantum beat pattern resulting from the interference between the decays of ϕ_1 and ϕ_2 states. The beat term may be written in the form$^{(43)}$

$$A \cos \omega t + B \cos(\omega t + \delta) \tag{5.10}$$

where $\omega = \dfrac{E_{\phi 1} - E_{\phi 2}}{\hbar}$ and the quantities A and B are combinations of the scattering amplitudes and the mixing coefficients and are therefore constants for a given electron scattering angle and field strength. (5.10) may be rewritten in the form

$$C \cos(\omega t + \phi) \ . \tag{5.11}$$

The phase δ is related to the phase of the beats by the expression

$$\delta = \tan^{-1} \left(\frac{\sin\phi}{\cos\phi - A}\right) \ . \tag{5.12}$$

The above analysis is of course only valid when exchange processes can be neglected, and indeed δ is defined only in this context.

Although observation of the $\phi_1 - \phi_2$ beat pattern provides the most direct method of determining the relative phase δ it is possible in principle to obtain a value for δ from the combination of measurements reported in this thesis. The parameters M_2 and M_{13} may be written in the form (see Appendix C)

$$M_2 = \frac{[1.5(\sigma_{s1}/\sigma_{p1}) + 0.06\alpha + 0.25 - 0.58(\varepsilon/\sigma_{p1})]1.6}{[17.3(\sigma_{s1}/\sigma_{p1} + 22.6\alpha + 25.7 + 3.4(\varepsilon/\sigma_{p1})]}$$

$$M_{13} = \frac{[1.77(\sigma_{s1}/\sigma_{p1}) + 13.06\alpha + 13.46 + 2.66(\varepsilon/\sigma_{p1})]1.6}{[17.3(\sigma_{s1}/\sigma_{p1}) + 22.6\alpha + 25.7 + 3.4(\varepsilon/\sigma_{p1})]} \qquad (5.13)$$

where $\frac{\sigma_s}{\sigma_{p1}} = \frac{|f_{00}|^2}{|f_{11}|^2}$, $\alpha = \frac{|f_{10}|^2}{|f_{11}|^2} = \frac{2\lambda}{1-\lambda}$

$$\varepsilon = \mathrm{Re}(f_{00}\, f_{10}^{*})$$

The quantity α may be obtained from measurements of the λ parameter, allowing the expressions (5.13) to be solved to yield values for σ_s/σ_{p1} and ε/σ_{p1}. The phase δ is then given by (see Appendix C)

$$\delta = \cos^{-1}\left[\frac{\varepsilon/\sigma_{p1}}{(\alpha\ \sigma_s/\sigma_{p1})^{\frac{1}{2}}}\right] \qquad (5.14)$$

The above analysis was performed on the data but the uncertainties involved did not allow meaningful values of δ to be determined.

CHAPTER 6

CONCLUSION

The previous chapters illustrate how a study of the time evolution of the Stark mixed $n = 2$ states of atomic hydrogen give rise to experimental observables which depend on a term arising from the interference between amplitudes describing the excitation of the $m = 0$ substates of the 2S and 2P states. This term is of particular interest since it represents the only term of the $n = 2$ density matrix still to be determined and is in fact proportional to the permanent electric dipole moment induced by the collision. This thesis reports the first attempt to investigate the coherent excitation of states of opposite parity using the coincidence technique. The data reported here relates to a combination of scattering amplitudes including a term which depends on $\mathrm{Re}(f_{00} f_{10}^{*})$. The data are however not of sufficient quality to isolate this term. The results are in excellent agreement with the predictions of a distorted wave second Born calculation of Walters$^{(70)}$ as one might expect at this energy.

A quantum beat signal arising from the interference in the decay of the Stark mixed 2S and 2P states has been observed but again the data are not of sufficient quality to allow a quantitative analysis of the beat battern. Such an analysis would yield information on the relative phase of scattering amplitudes of opposite parity.

Angular correlation measurements have also been made at incident electron energies of 100 eV and 350 eV. The results for the λ parameter at 100 eV are in very good agreement with theory and the data of Hood et al.$^{(34)}$, and in particular contradict the very small value of

λ measured at $\theta_e = 10°$ by Slevin et al.(36). Results for the R parameter are not in particularly good agreement with the theoretical predictions considered here. The data for λ and R at an incident energy of 350 eV is in very poor agreement with the theoretical predictions. This is somewhat surprising in the case of the second Born calculation of Walters(71) since this relatively sophisticated calculation is expected to perform well at such high energies.

Although this study has failed to isolate the S - P interference term and therefore does not represent a particularly convincing test of theory it does represent a new application of the coincidence technique. A comprehensive theory, applicable to the coincidence technique, for the excitation and decay of Stark mixed states is derived and presented. An analysis is given of the main factors affecting the experimental time resolution and methods by which these can be minimised have been demonstrated. The time resolution achieved in this work of 0.58ns represents a considerable improvement on the previously reported best resolution of 3ns(35). This time resolution should in principle be sufficient to make a measurement of the beat pattern with period about 0.6ns as indeed Figure 25 confirms. The major problem may be a lack of long term stability of the apparatus. Since integration times for this type of measurement are generally quite long, up to a few days, with the present set up, great demands are made on the stability of the system.

A successful measurement of the S - P interference terms seems most likely to be obtained by shortening the integration times involved and improving the stability of the apparatus.

$\theta_{e(\text{mean})}$	R_{13}				$R_2 \times 10^2$			
	Experiment	DWSB	PWSB	OSFW	Experiment	DWSB	PWSB	OSFW
1.45°	0.883 ± 0.021	0.860	0.848	0.524	1.54 ± 0.4	1.38	1.56	7.35
2.55°	0.826 ± 0.025	0.846	0.848	0.554	1.55 ± 0.5	1.64	1.56	6.80
3.65°	0.790 ± 0.022	0.820	0.845	0.588	1.21 ± 0.4	2.06	1.57	6.22
4.75°	0.761 ± 0.027	0.787	0.842	0.622	2.70 ± 0.5	2.61	1.58	5.67
5.95°	0.769 ± 0.021	0.744	0.830	0.636	3.19 ± 0.5	3.15	1.57	5.23

TABLE 1: The parameters R_{13} and R_2 as a function of mean electron scattering angle.

DWSB: Distorted Wave Second Born calculation of Walters(70)

PWSB: Plane Wave Second Born calculation of Fargher and Roberts(71)

OSFW: On Shell Fadeev Watson calculation of Fargher and Roberts(71)

θ_e	θ_e'
0.5	0.445
1.0	0.890
1.5	1.33
2.0	1.78
2.5	2.22
3.0	2.67
3.5	3.11
4.0	3.56
4.5	4.00
5.0	4.45
5.5	4.89
6.0	5.34
6.5	5.78
7.0	6.23
7.5	6.69
8.0	7.12

TABLE 2: Modification to electron trajectories due to the effect of the electric field calculated according to equation (B.14). θ_e is the true electron scattering angle and θ_e' the apparent scattering angle (See Figure 26).

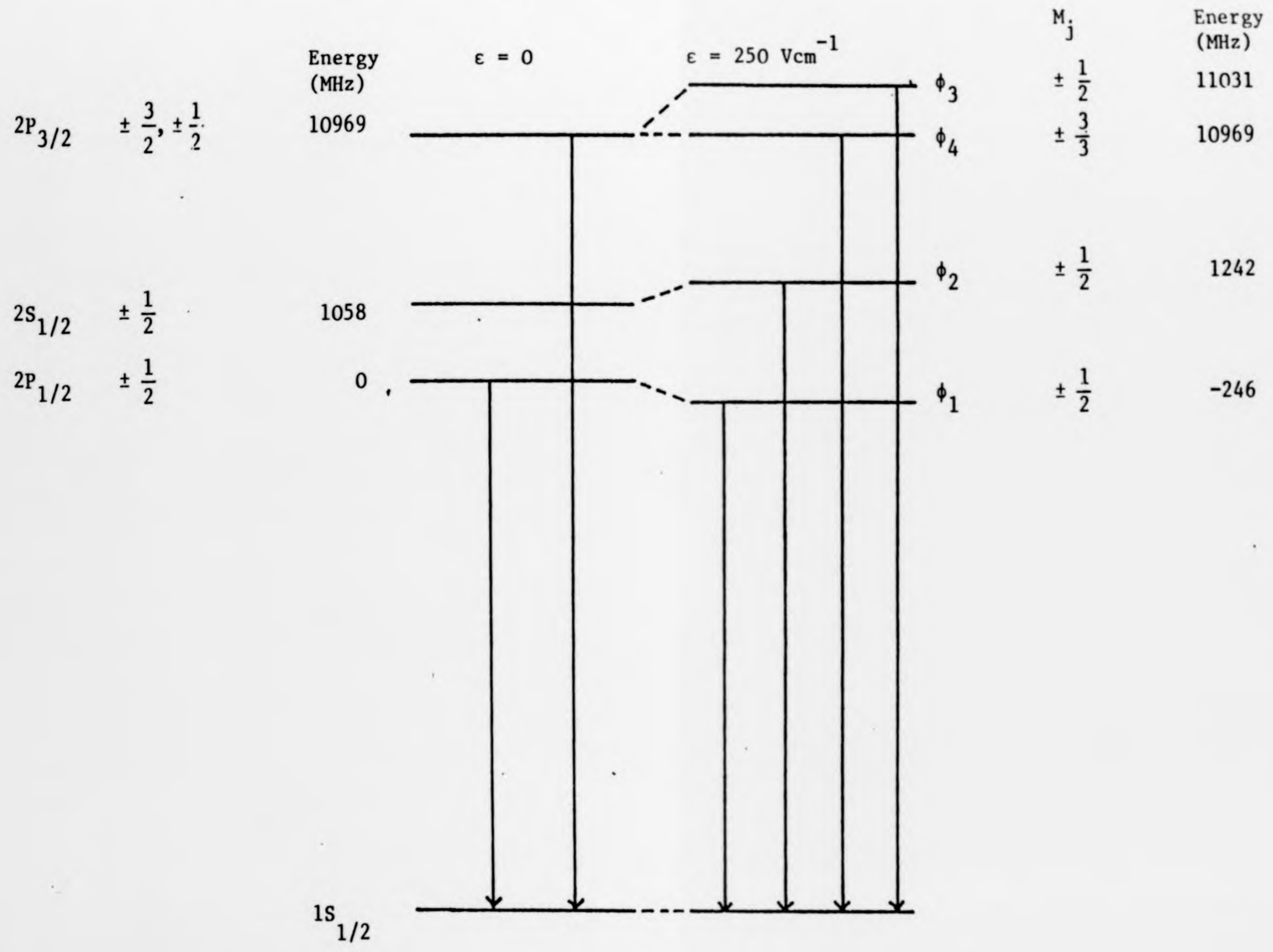

Energy level diagram

Figure 1.

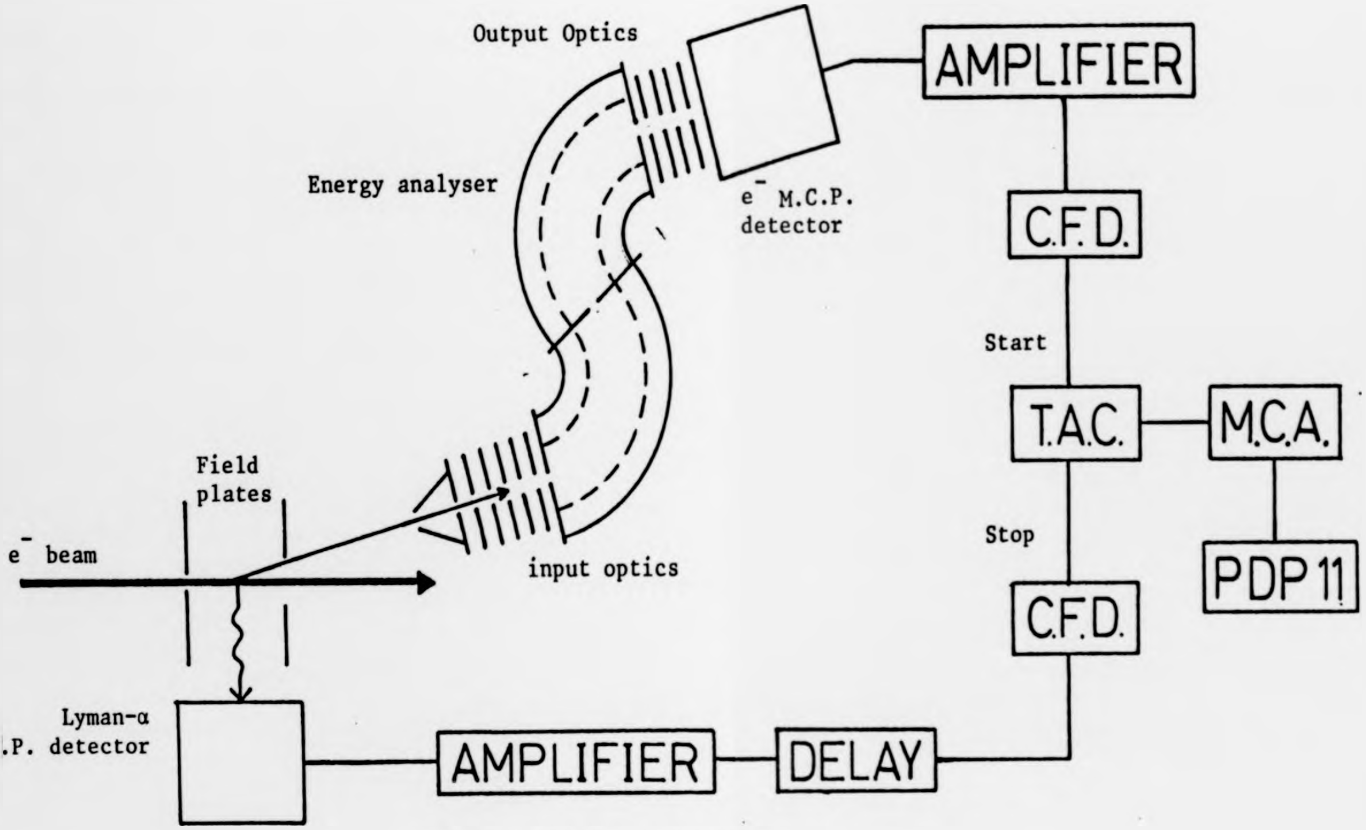

Experimental arrangement

Figure 2.

Element	Voltage*
I	78
II	300
III	70
IV	$4 \times E^{\dagger}$
V	$\frac{3}{2} \times E$
VA	$\leqslant 3/2 \times E$ $\geqslant E$
VI	E

*All voltages are w.r.t. cathode

†E = beam energy in eV

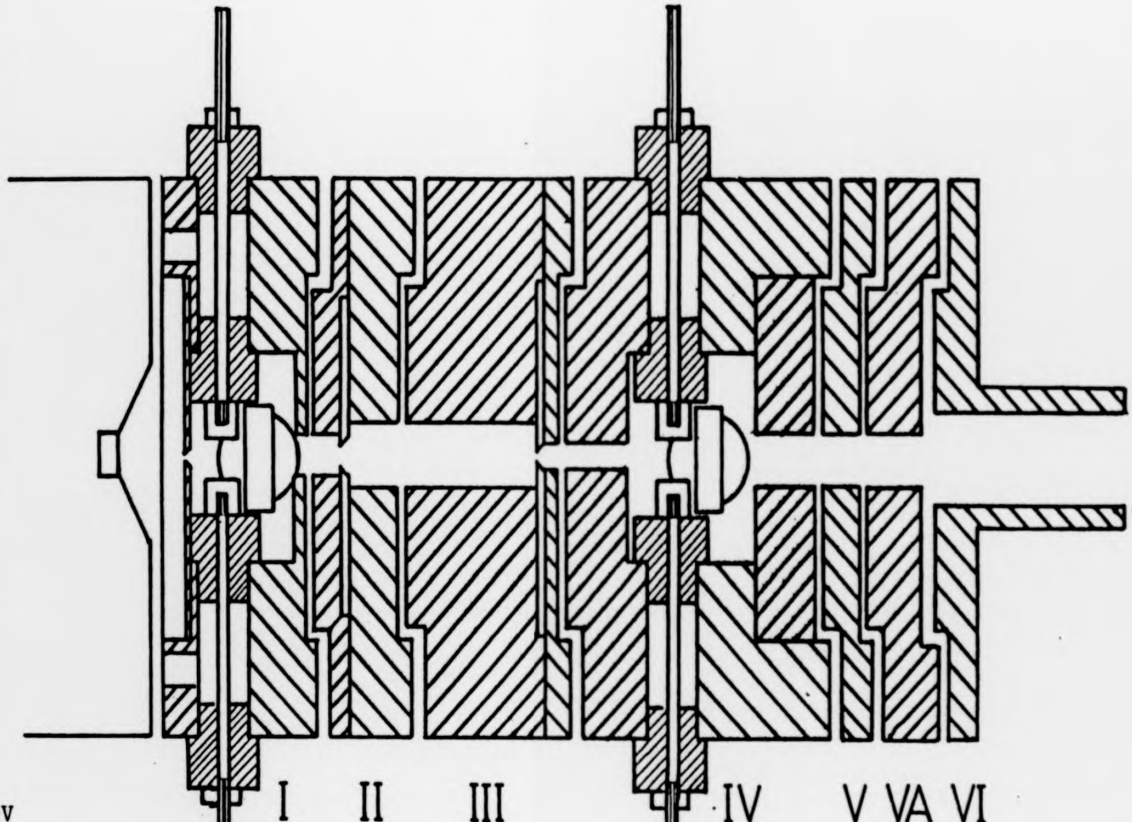

Electron gun

Figure 3.

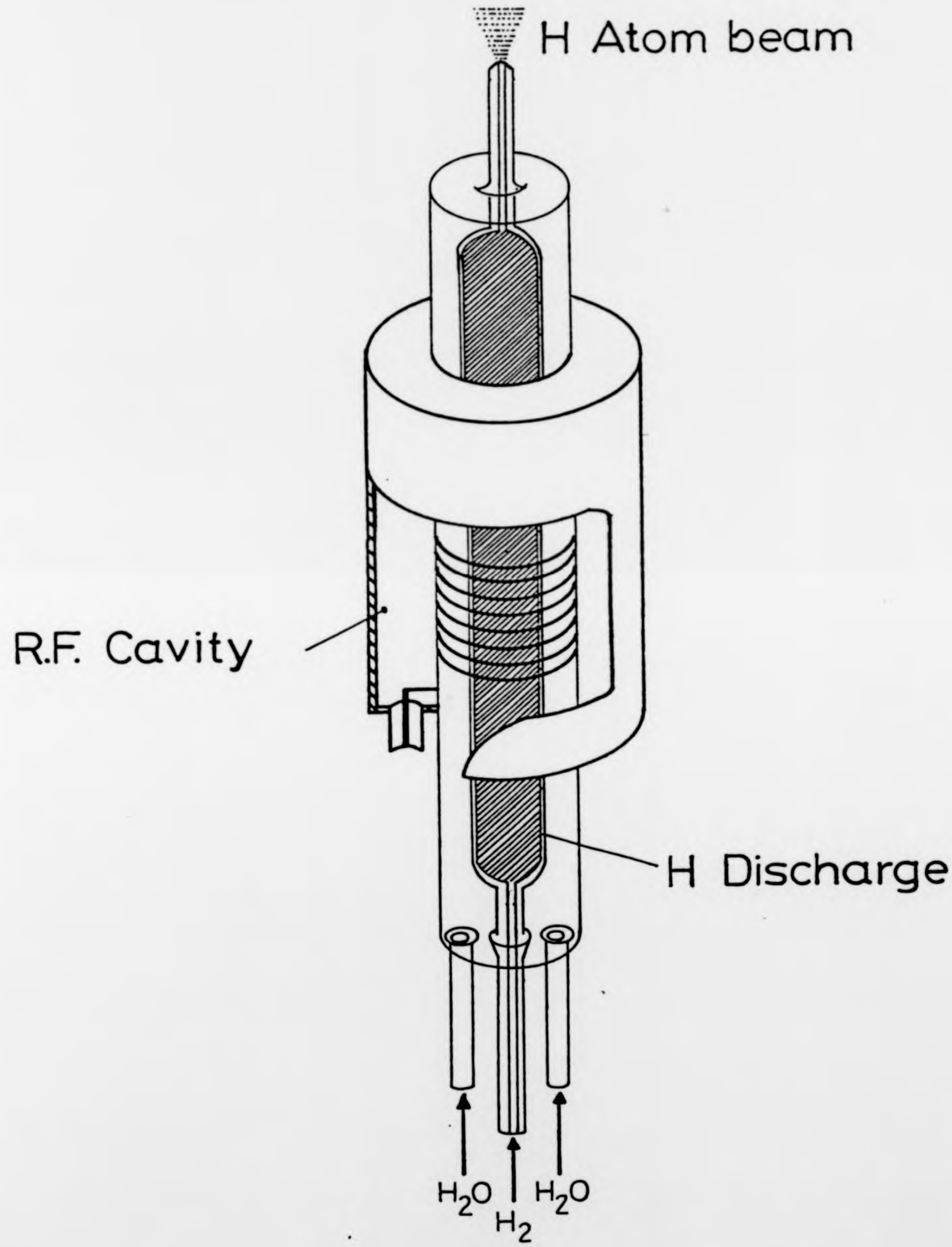

Discharge Tube

Figure 4.

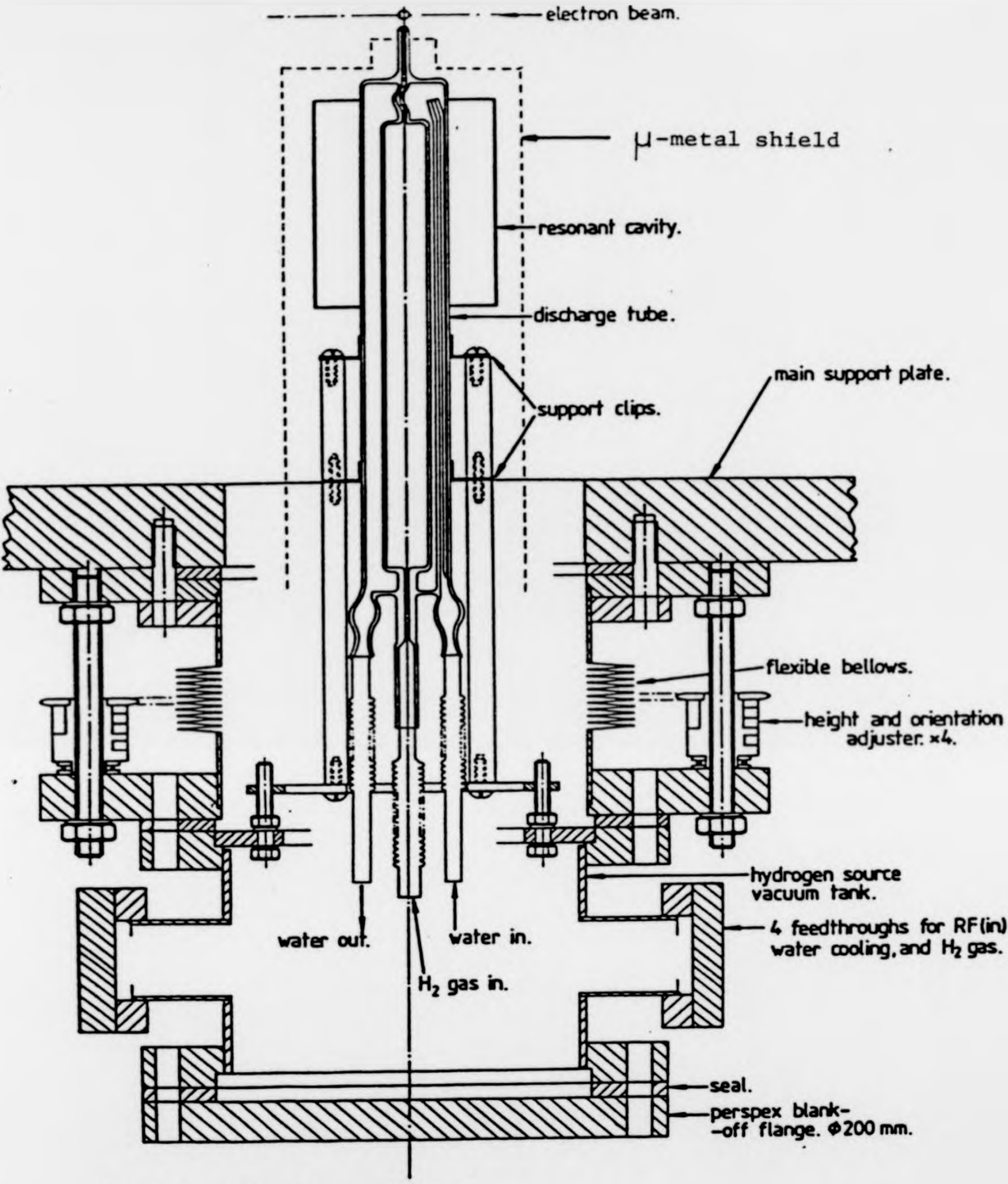

<u>The atomic hydrogen source.</u>

Figure 5.

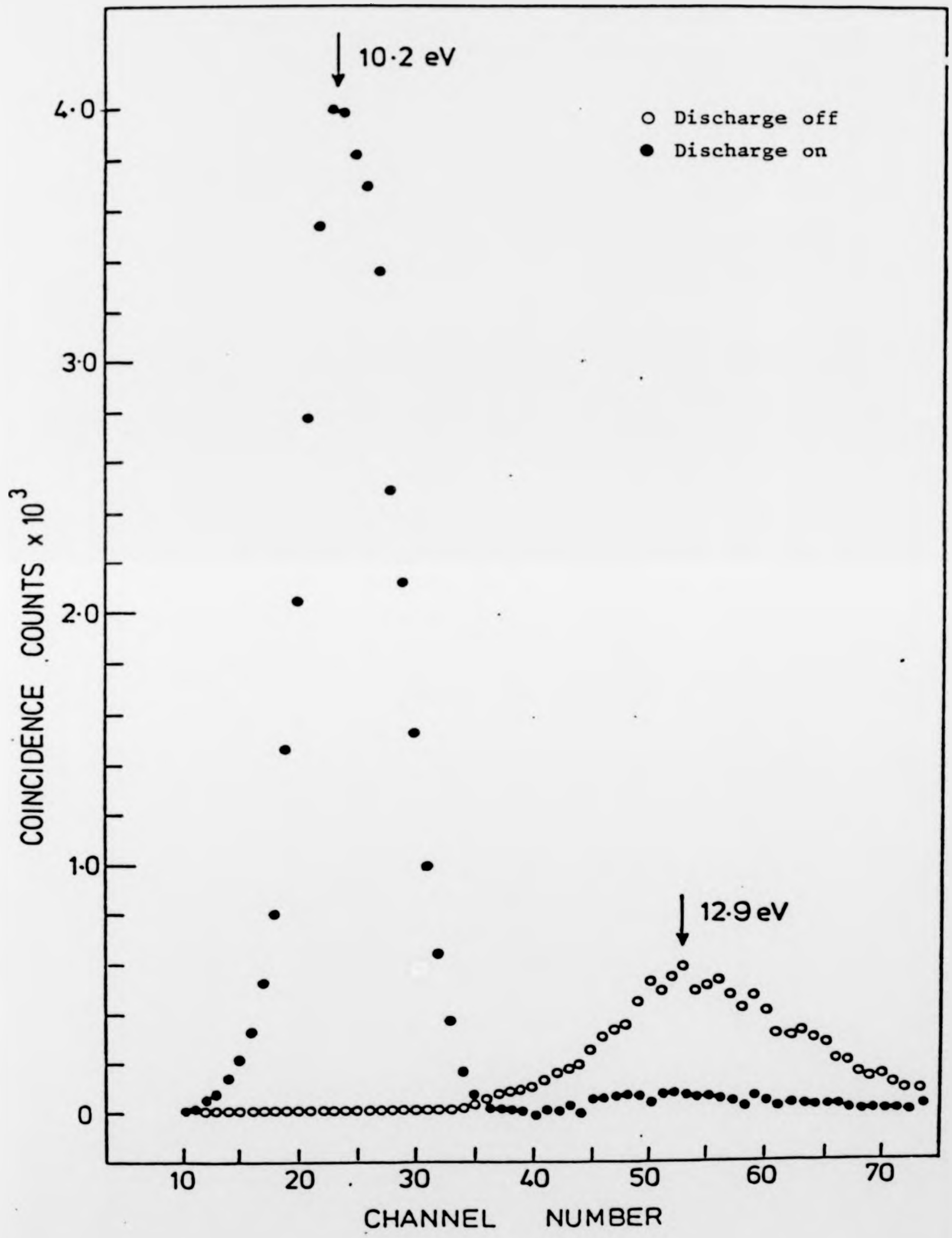
10·2 eV
12·9 eV
○ Discharge off
● Discharge on
COINCIDENCE COUNTS x 10^3
4·0
3·0
2·0
1·0
0
CHANNEL NUMBER
10
20
30
40
50
60
70

Figure 6.

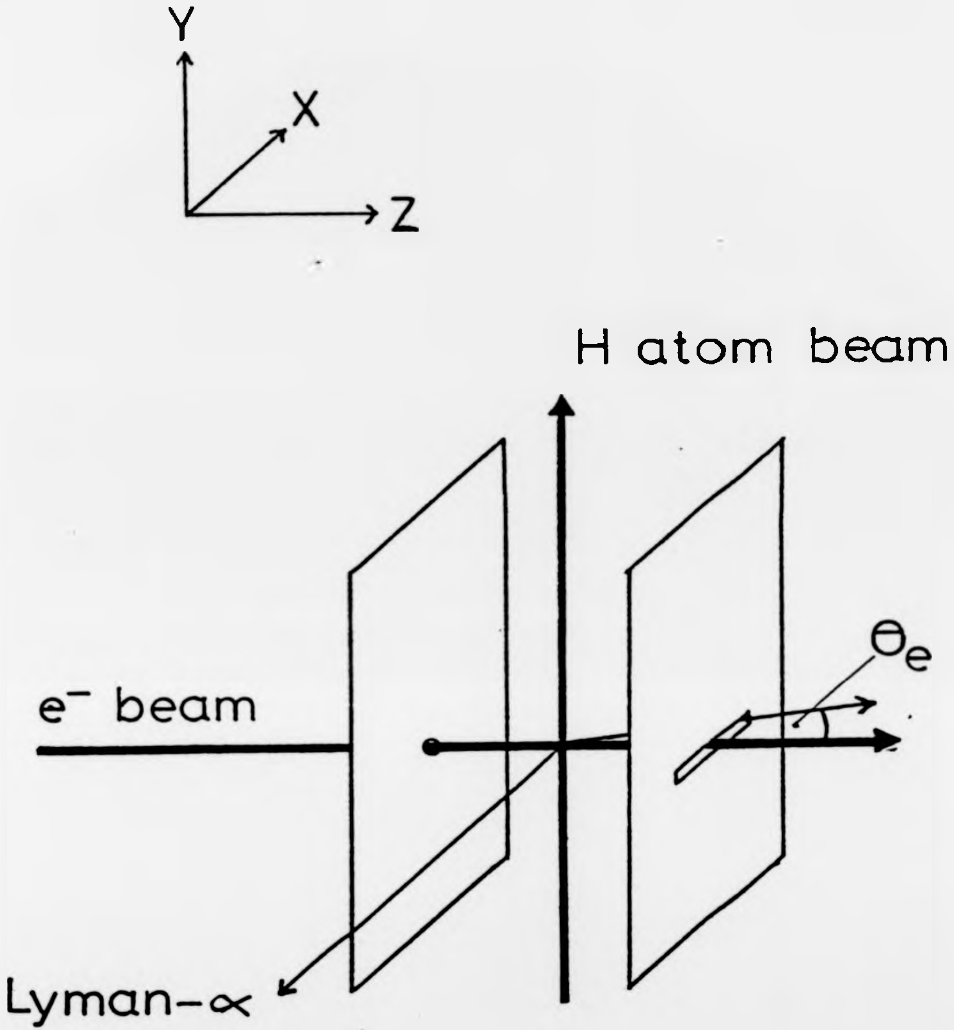

Experimental geometry

Figure 7.

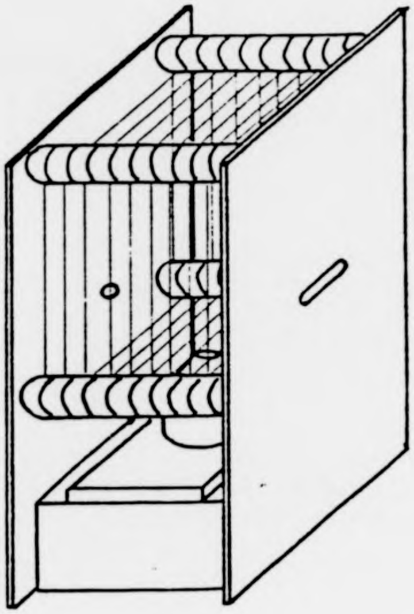

Field plates
incorporating
grid wires

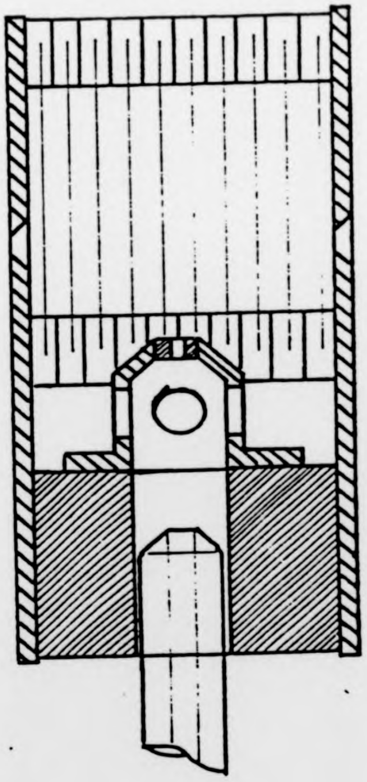

Section view
of plates showing
atomic beam collimator

Figure 8.

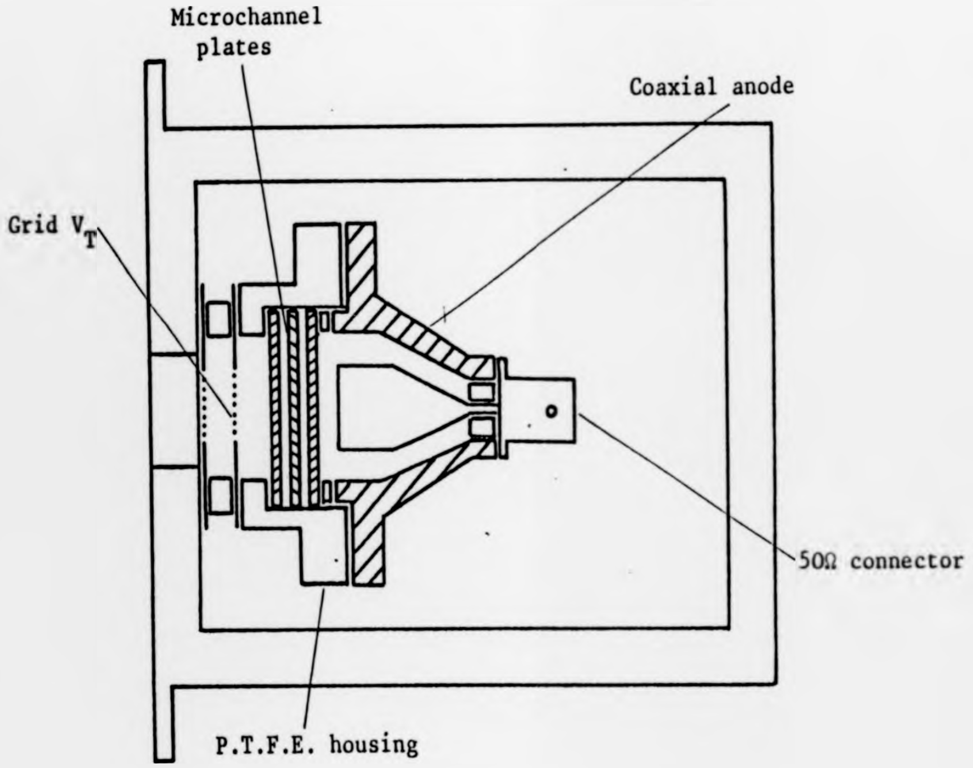

Electron M.C.P. detector

Figure 9.

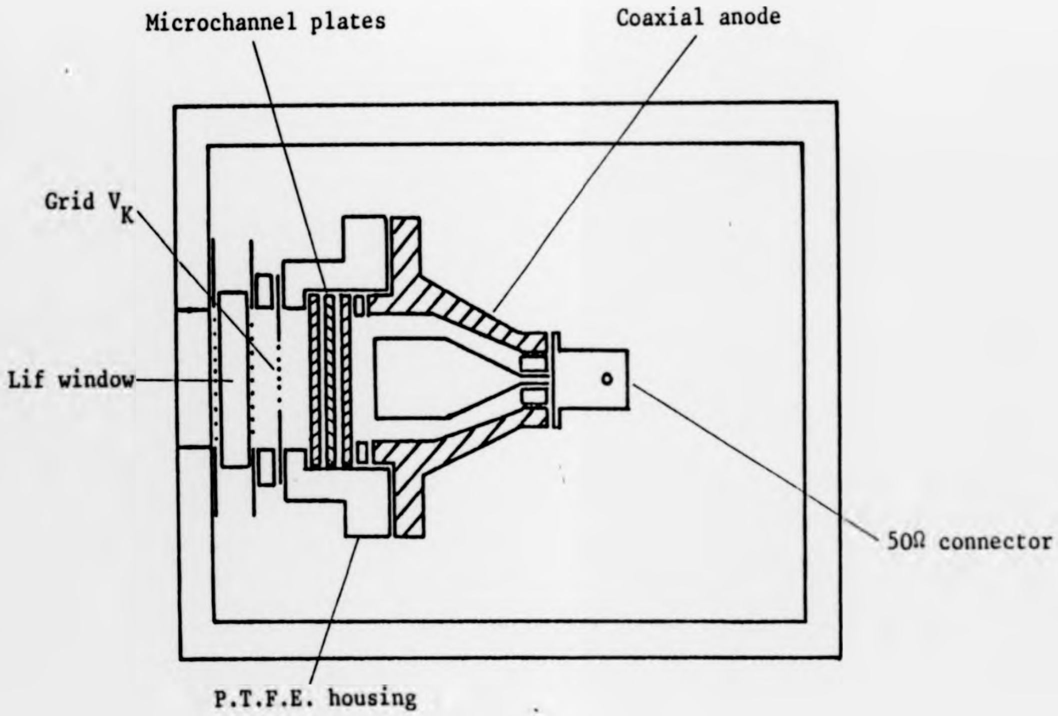

Lyman-α M.C.P. detector

Figure 10.

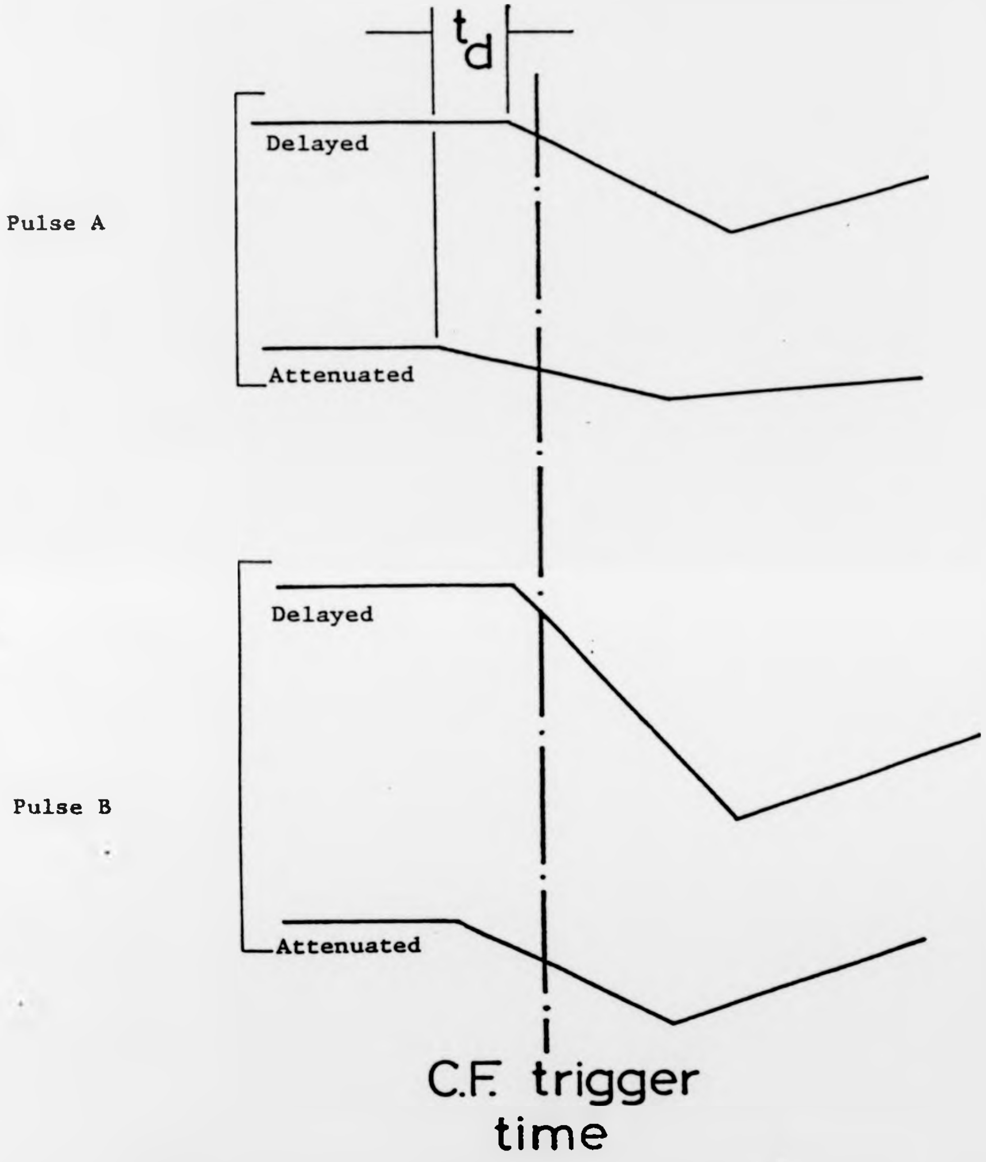

Constant fraction trigger timing for two different pulse amplitudes.

Figure 11.

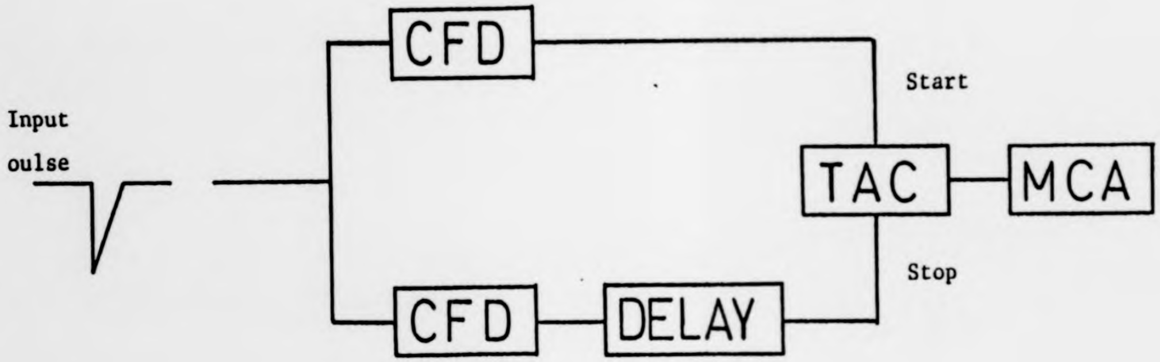

Circuit used for the adjustment of the constant fraction discriminators.

Figure 12.

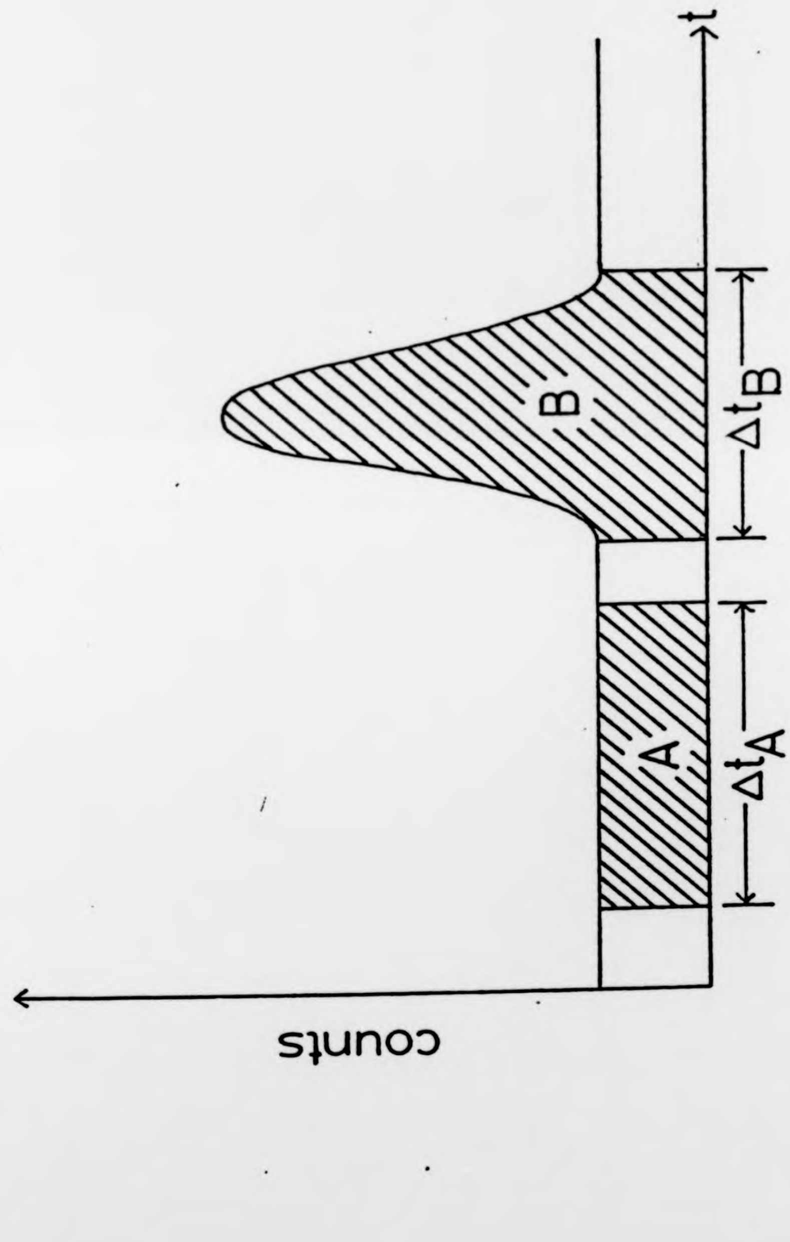

Typical shape of a coincidence spectrum

Figure 13.

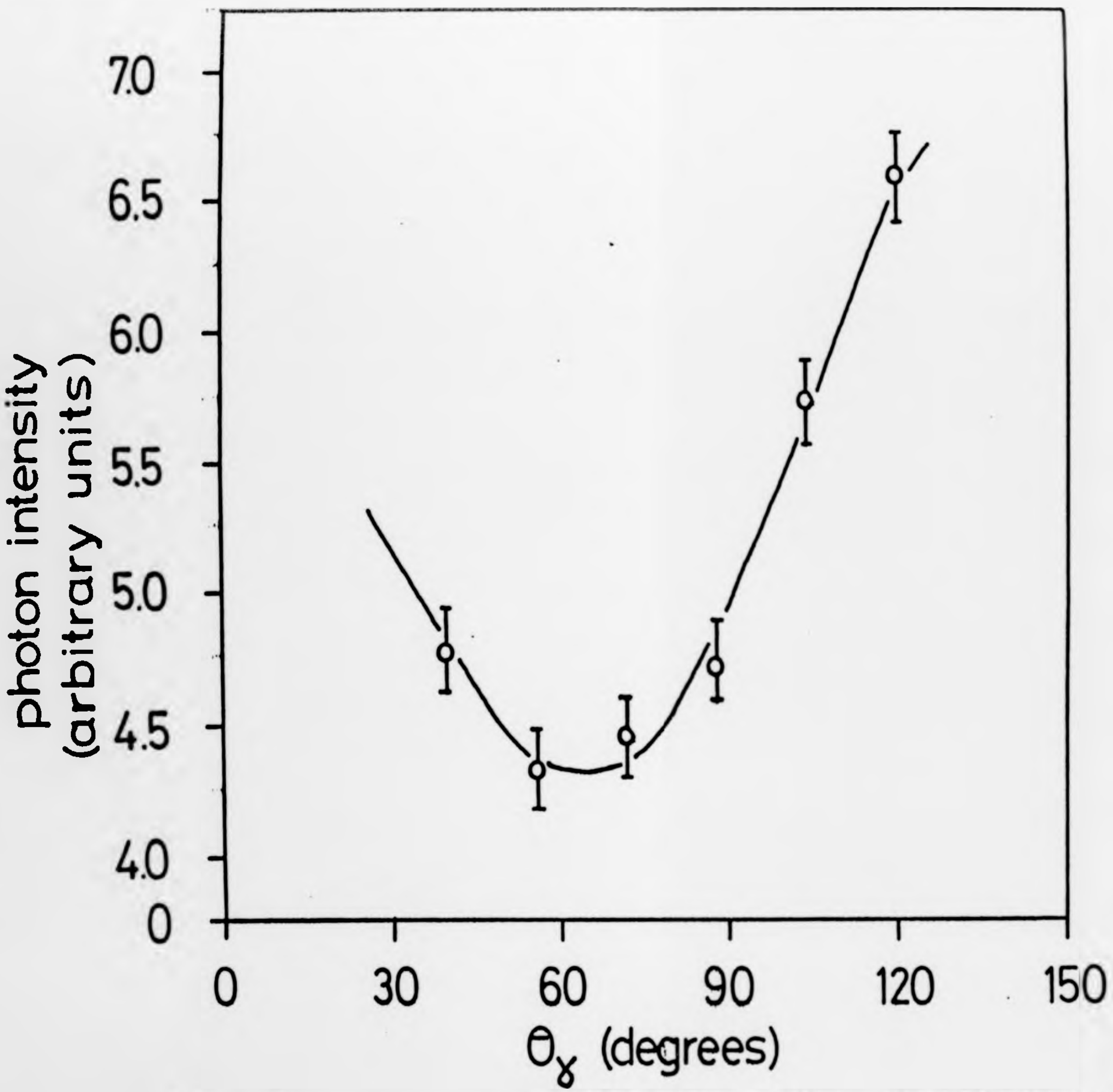

Angular correlation curve $\theta_e = 10°$, incident energy = 100 eV. The full curve represents a least squares fit of equation (2.47)

Figure 14.

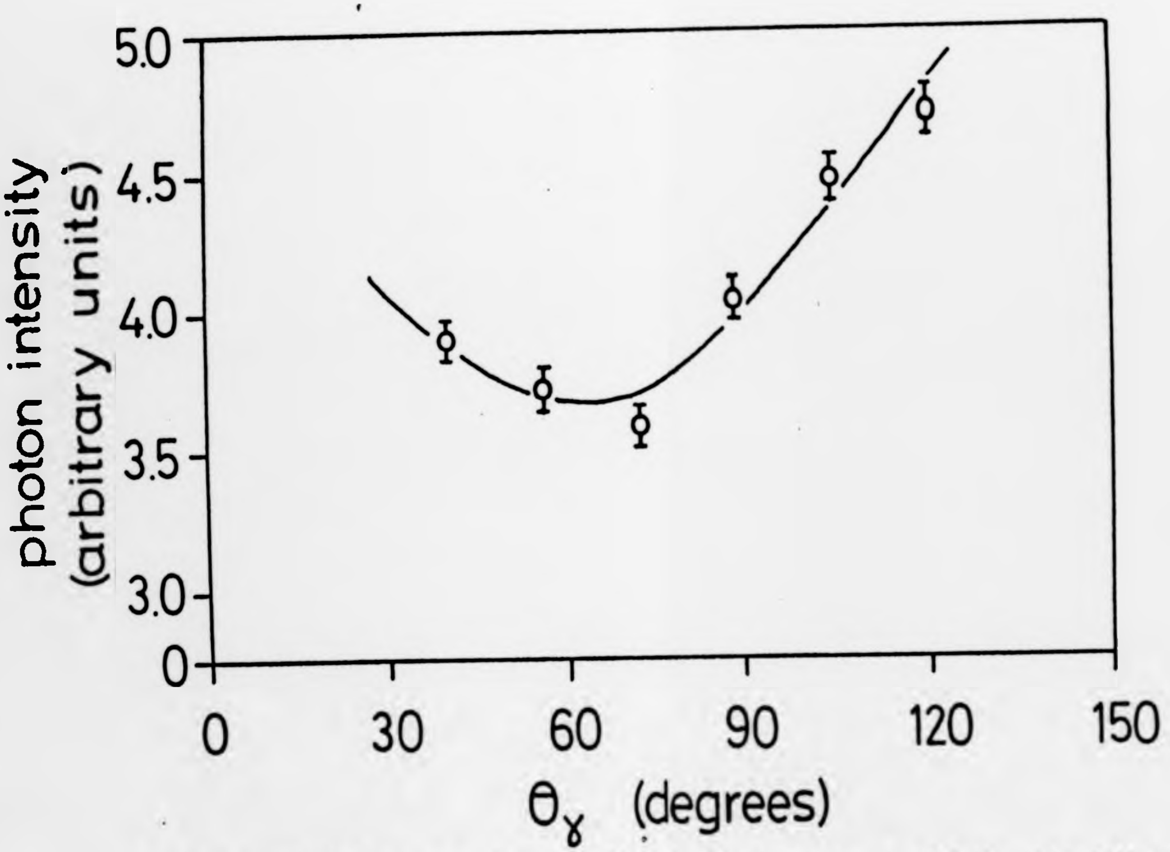

Angular correlation curve, $\theta_e = 2.4°$, incident energy = 350 eV. The full curve represents a least squares fit of equation (2.47).

Figure 15.

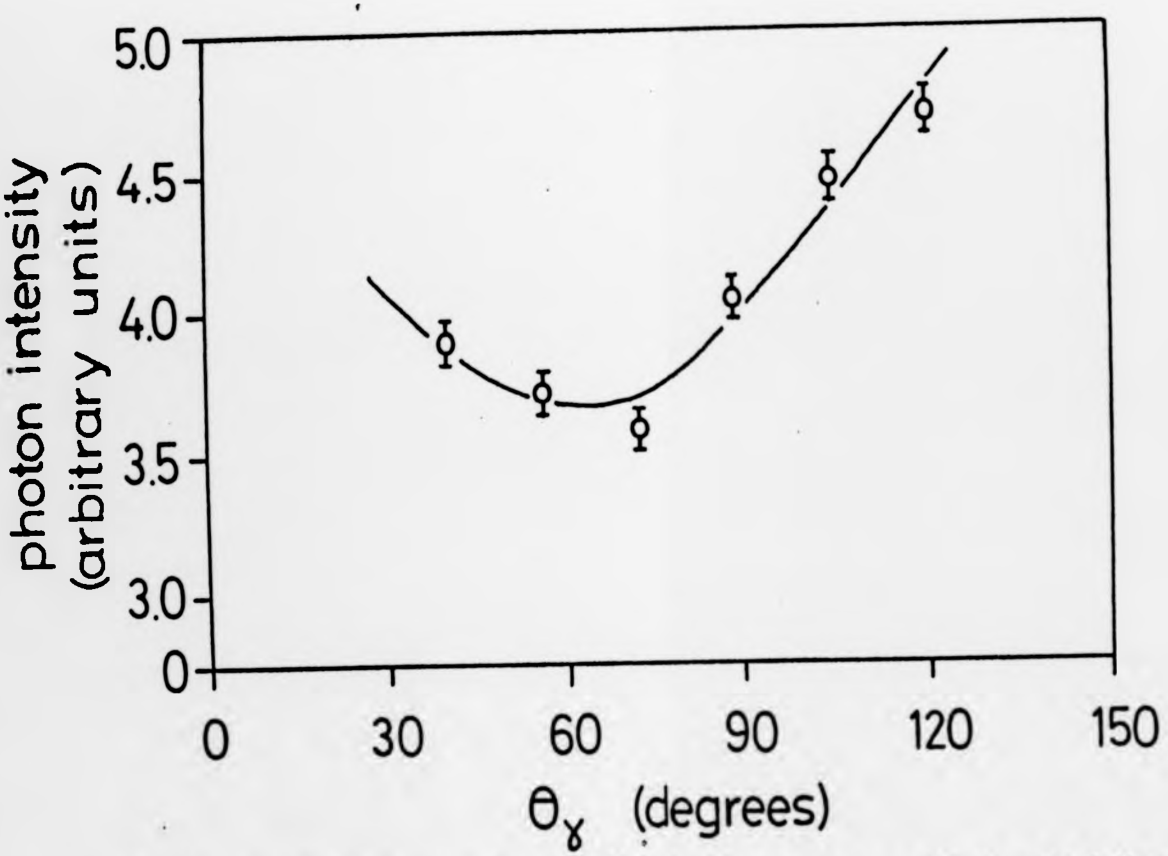

Angular correlation curve, $\theta_e = 2.4°$, incident energy = 350 eV. The full curve represents a least squares fit of equation (2.47).

Figure 15.

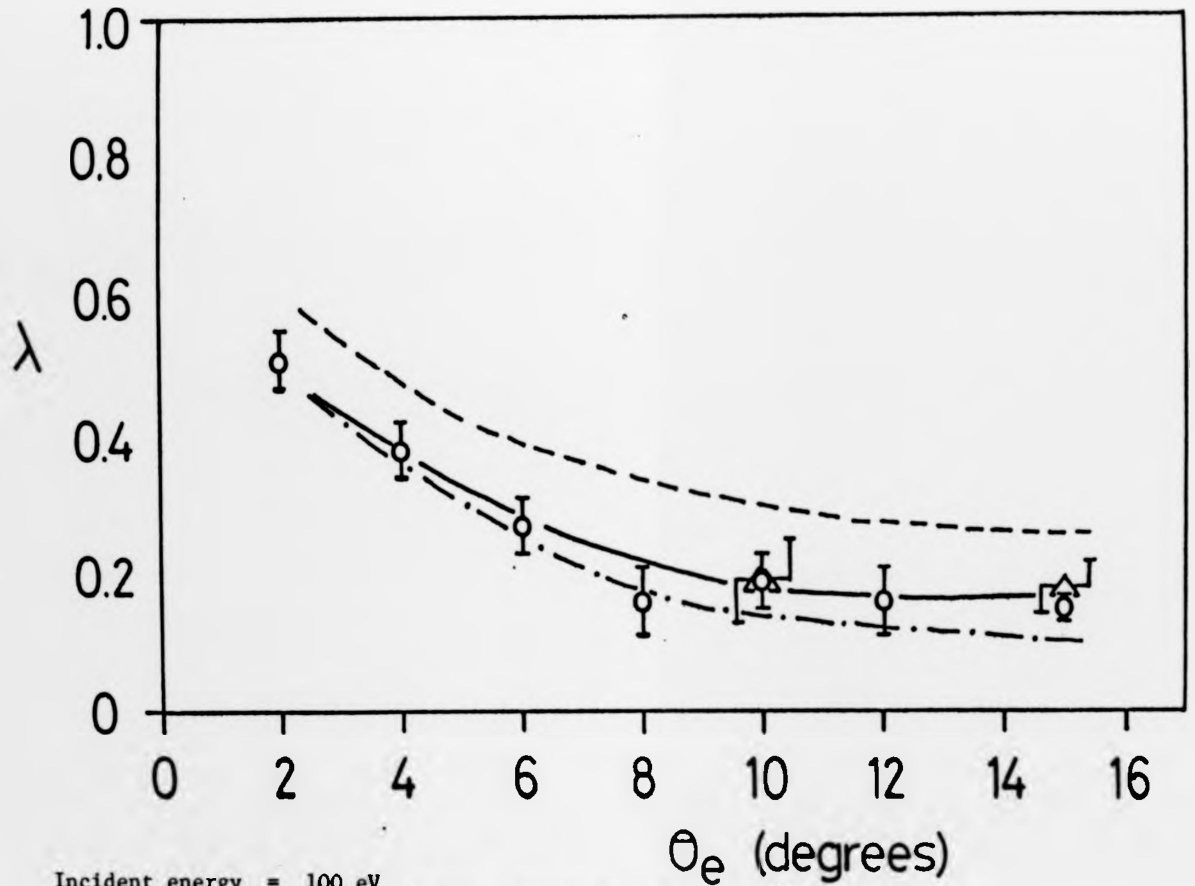

Incident energy = 100 eV

——— Free-particle-Second-Born calculation of Fargher(68).

------ On-Shell-Fadeev-Watson calculation of Fargher(68).

- . - Distorted-Wave-Polarised-Orbital calculation of Baluja et al.(69).

Δ Data of Hood et al.(34)

Figure 16.

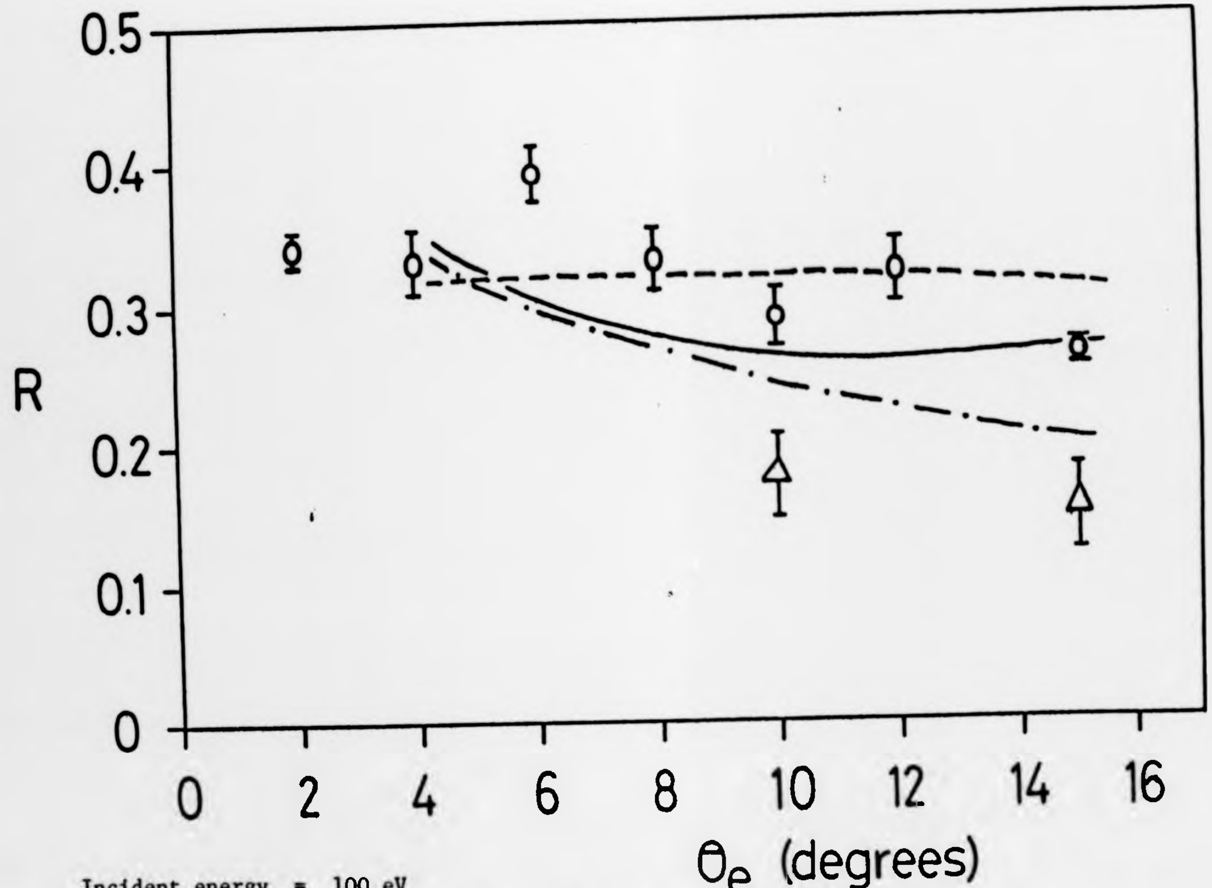

Incident energy = 100 eV

—— Free-particle-Second-Born calculation of Fargher(68).

----- On-Shell-Fadeev-Watson calculation of Farcher(68)

- . - Distorted-Wave-Polarised-Orbital calculation of Baluja et al.(69).

Δ Data of Hood et al.(34).

Figure 17.

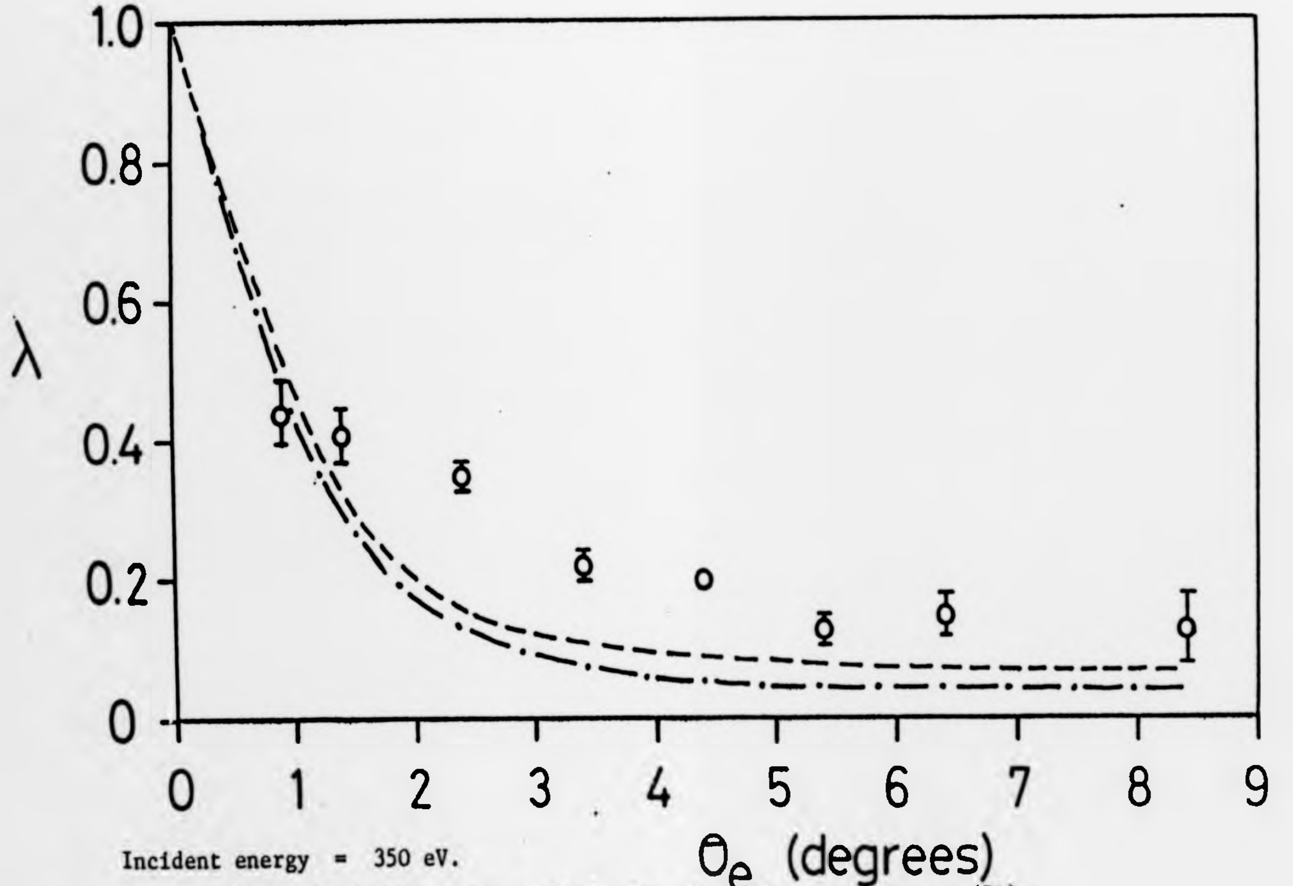

Incident energy = 350 eV.

------ On-Shell-Fadeev-Watson calculation of Fargher and Roberts (71).

-.- Distorted-Wave-Second-Born calculation of Walters$^{(70)}$.

Figure 18.

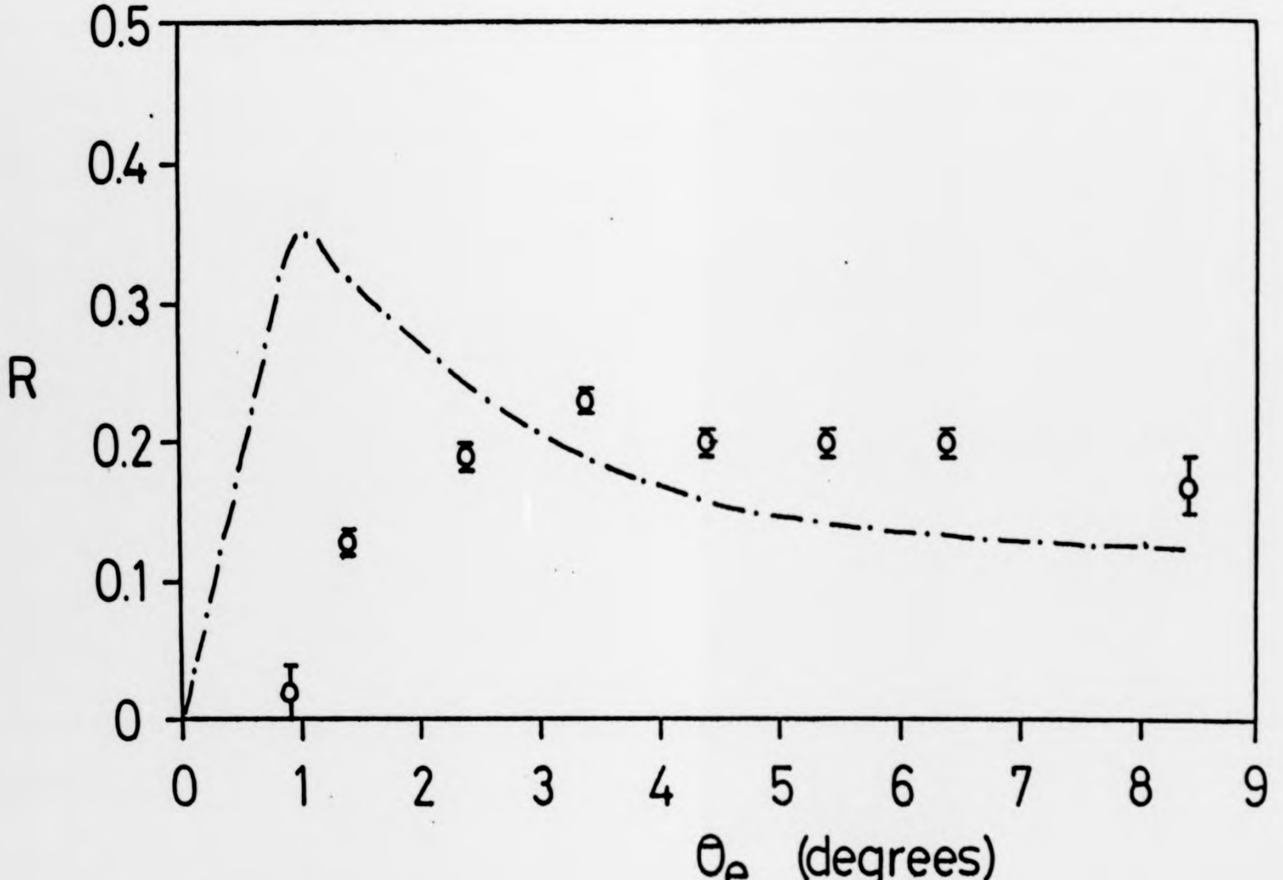

Incident energy = 350 eV.

-.- Distorted-Wave-Second-Born calculation of Walters$^{(70)}$.

Figure 19.

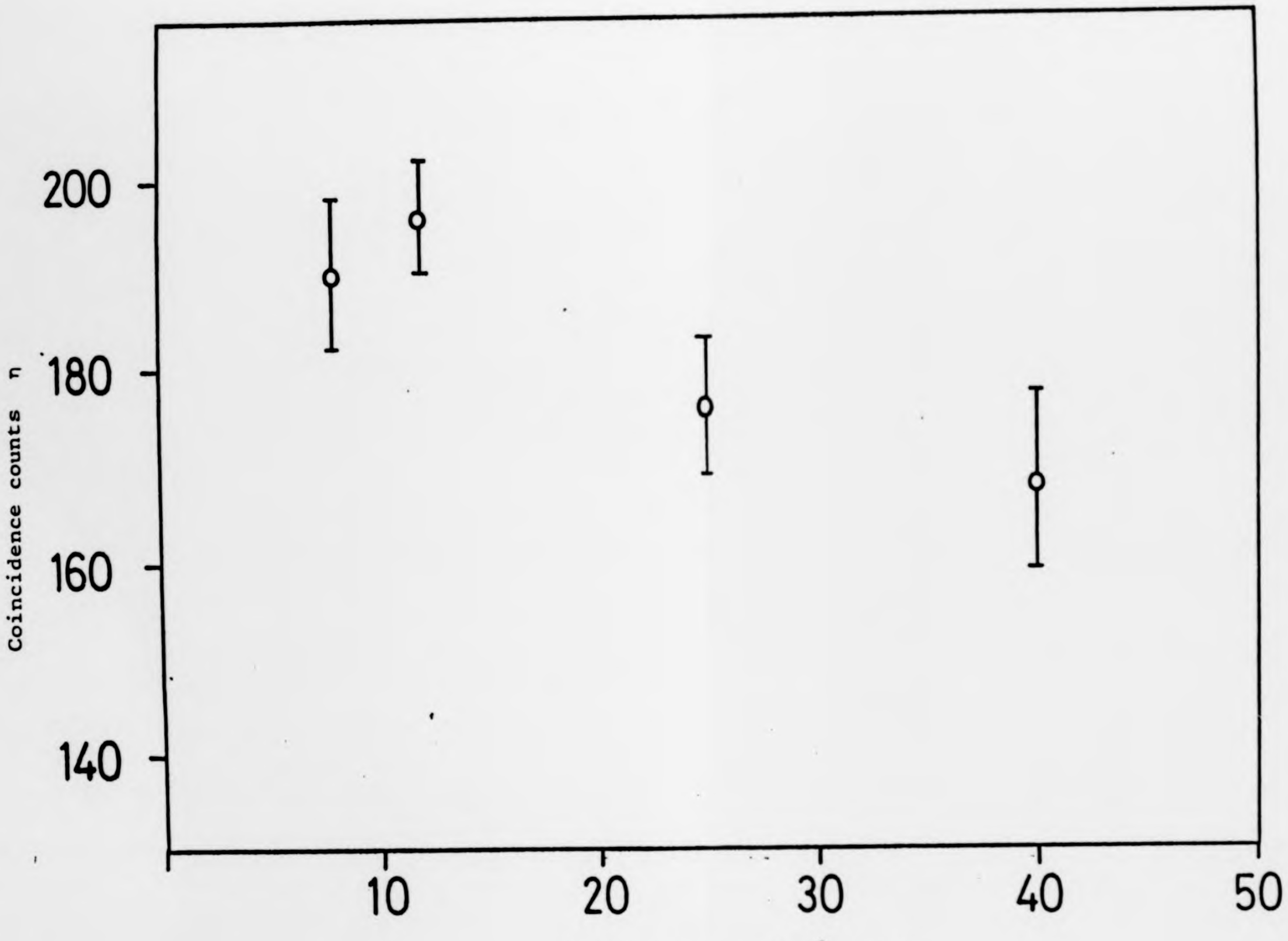
Coincidence counts n
200
180
160
140
10
20
30
40
50
Hydrogen pressure (10^{-2} torr.)

Figure 20.

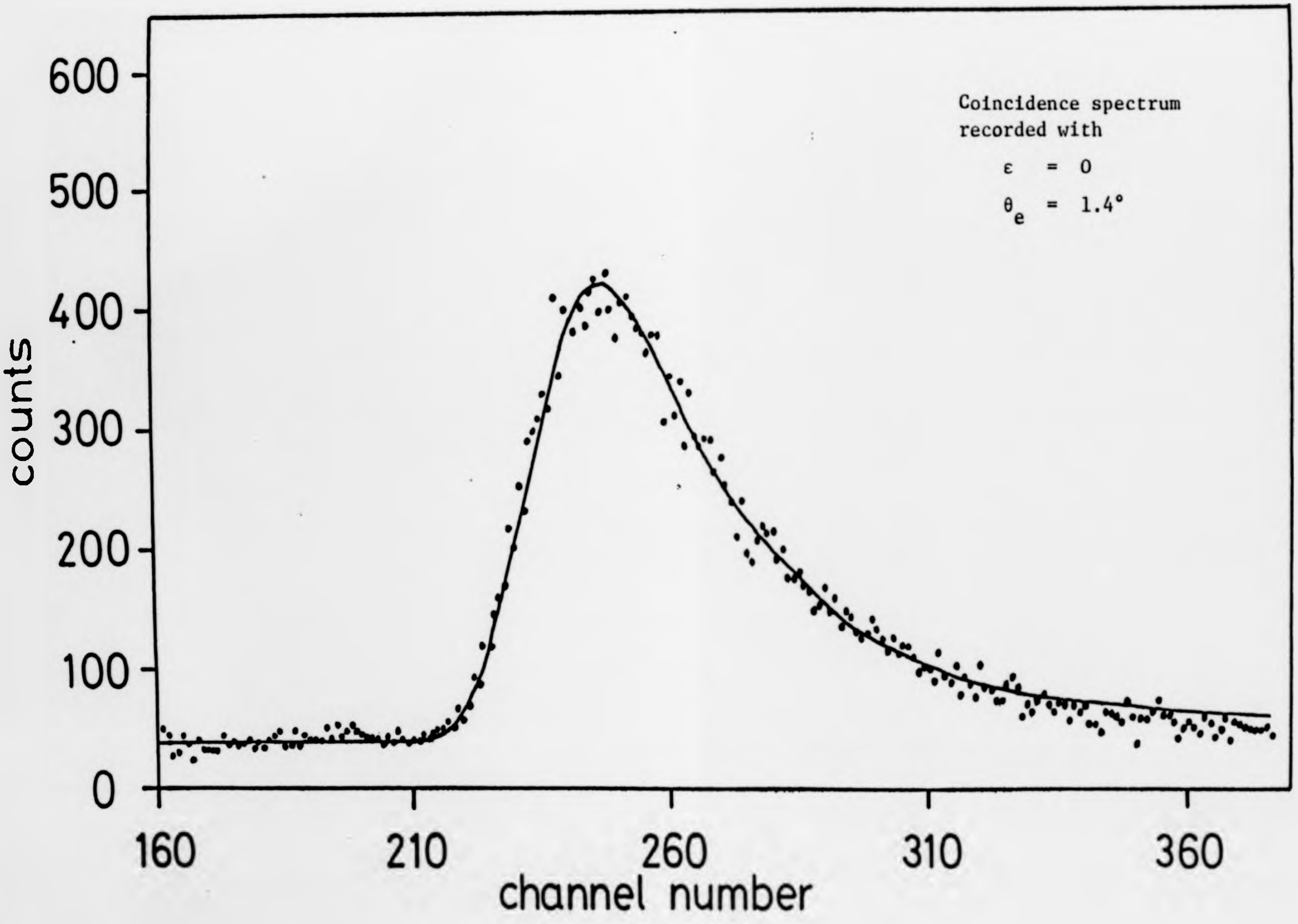
Coincidence spectrum
recorded with
$\varepsilon = 0$
$\theta_e = 1.4°$
counts
0
100
200
300
400
500
600
160
210
260
310
360
channel number

Figure 21.

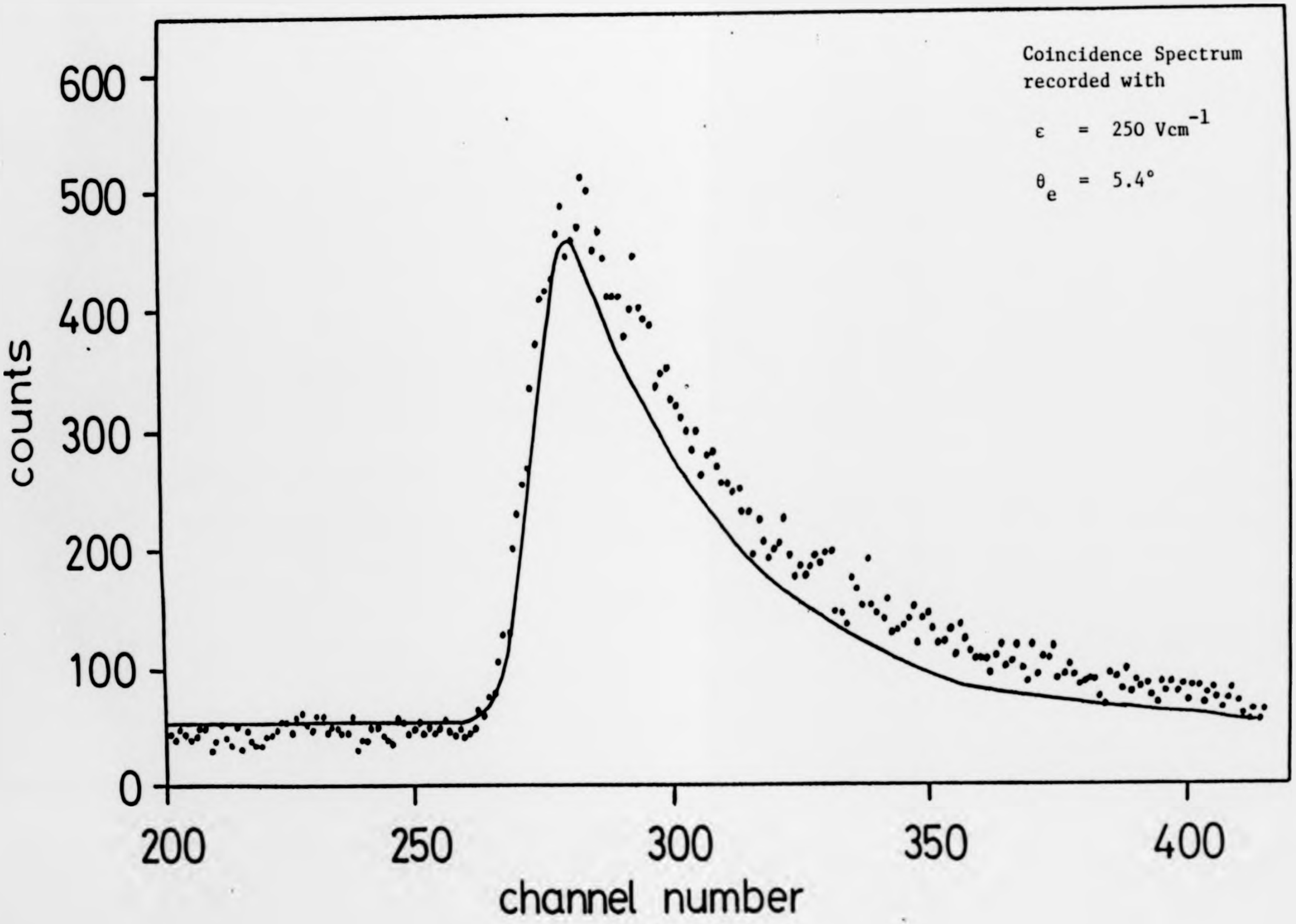
Coincidence Spectrum
recorded with
ε = 250 Vcm^{-1}
θ$_e$ = 5.4°
counts
0
100
200
300
400
500
600
200
250
300
350
400
channel number

Figure 22.

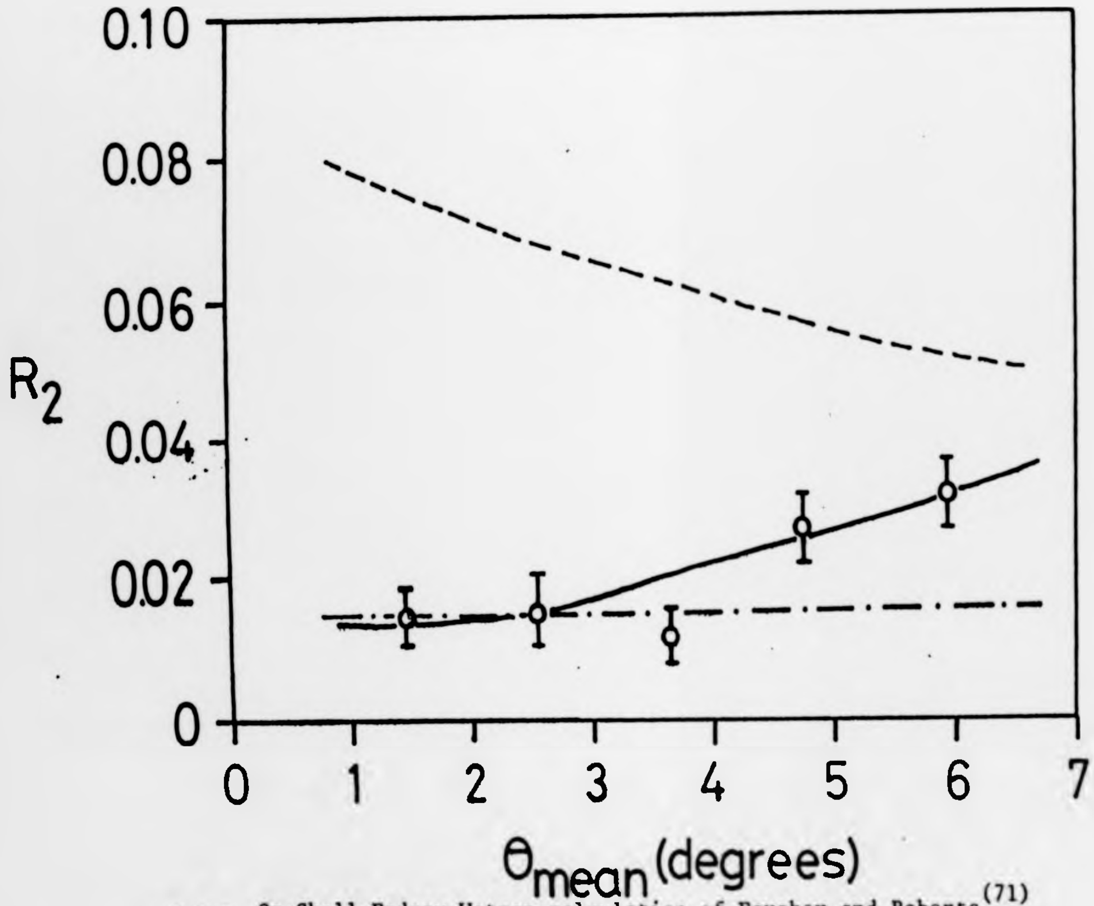

- - - On-Shell-Fadeev-Watson calculation of Fargher and Roberts(71)
- . - Plane-Wave-Second-Born calculation of Fargher and Roberts(71)
—— Distorted-Wave-Second-Born calculation of Walters(70)

Figure 23.

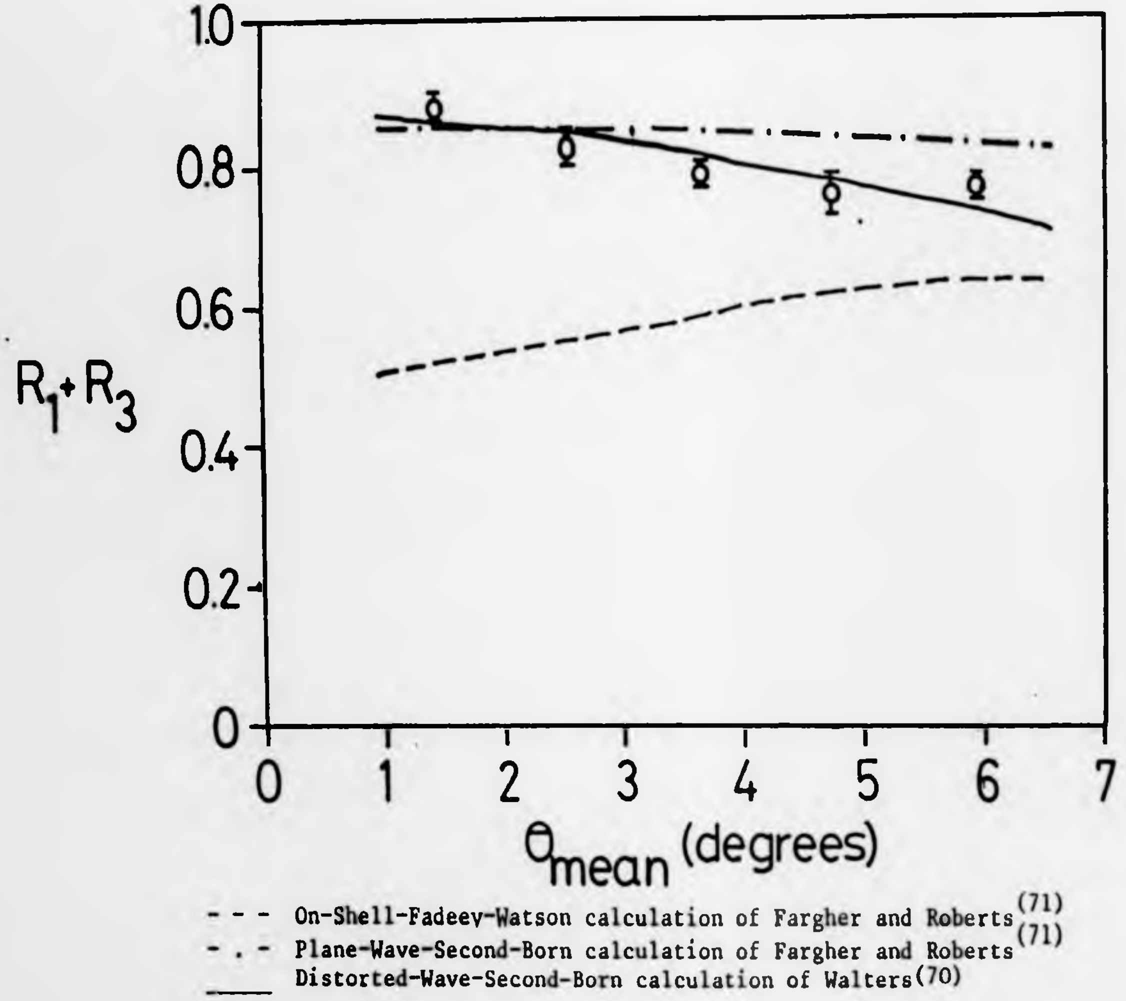
1.0
0.8
0.6
0.4
0.2
0
R_1+R_3
0
1
2
3
4
5
6
7
θ_{mean} (degrees)
- - - On-Shell-Fadeev-Watson calculation of Fargher and Roberts(71)
- . - Plane-Wave-Second-Born calculation of Fargher and Roberts(71)
—— Distorted-Wave-Second-Born calculation of Walters(70)

Figure 24.

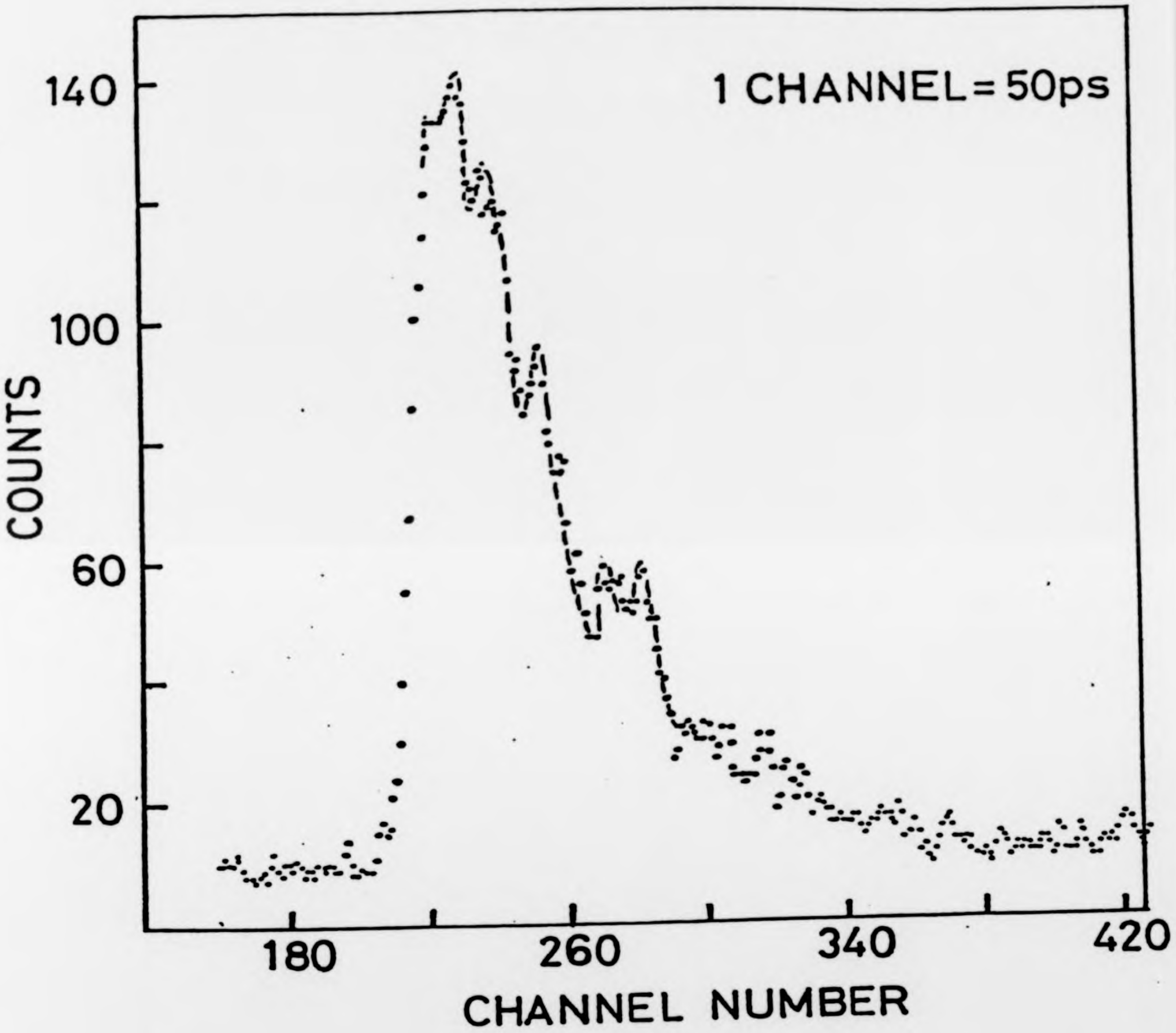

Coincidence spectrum recorded with an electric field of 250 Vcm^{-1} applied to the interaction region.

Figure 25.

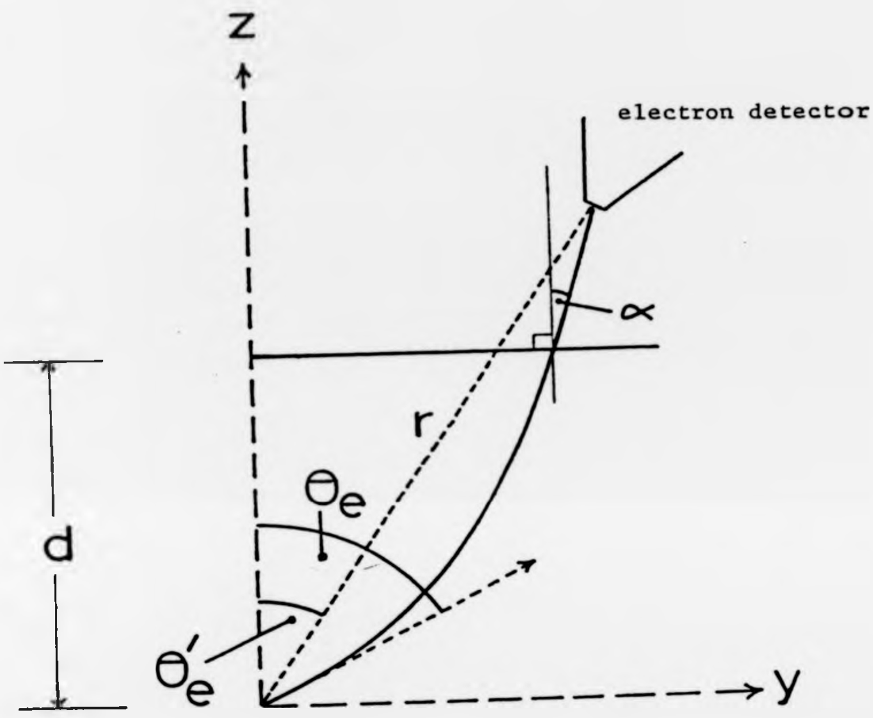

Modification to electron trajectories due to the electric field

Figure 26.

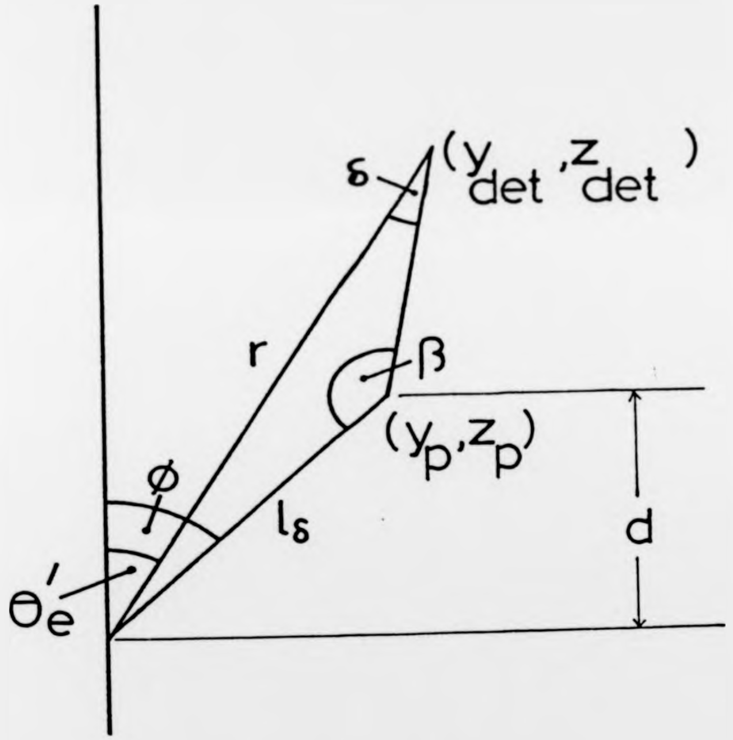

Figure 27.

APPENDIX A

I. Calculation of the Coefficients in the Expansion of the Stark Mixed States

In order to simplify the following calculations we define the following states in terms of spherical harmonic functions Y_{LM} and atomic spin states $|\alpha\rangle$ and $|\beta\rangle$ and using the notation $|nJLM_J\rangle$.

The ground states are

$$
\begin{aligned}
|1\ \tfrac{1}{2}\ 0\ \tfrac{1}{2}\rangle &= Y_{00}|\alpha\rangle = |1\rangle \\
|1\ \tfrac{1}{2}\ 0\,{-\tfrac{1}{2}}\rangle &= Y_{00}|\beta\rangle = |2\rangle
\end{aligned}
$$

The $n = 2$ states are

$$
\begin{aligned}
|2\ \tfrac{1}{2}\ 1\ \tfrac{1}{2}\rangle &= -\sqrt{1/3}\ Y_{10}|\alpha\rangle + \sqrt{2/3}\ Y_{11}|\beta\rangle = |3\rangle \\
|2\ \tfrac{1}{2}\ 1\,{-\tfrac{1}{2}}\rangle &= -\sqrt{2/3}\ Y_{1-1}|\alpha\rangle + \sqrt{1/3}\ Y_{10}|\beta\rangle = |4\rangle \\
|2\ \tfrac{1}{2}\ 0\ \tfrac{1}{2}\rangle &= Y_{00}|\alpha\rangle = |5\rangle \\
|2\ \tfrac{1}{2}\ 0\,{-\tfrac{1}{2}}\rangle &= Y_{00}|\beta\rangle = |6\rangle \\
|2\ \tfrac{3}{2}\ 1\ \tfrac{1}{2}\rangle &= \sqrt{2/3}\ Y_{10}|\alpha\rangle + \sqrt{1/3}\ Y_{11}|\beta\rangle = |7\rangle \\
|2\ \tfrac{3}{2}\ 1\,{-\tfrac{1}{2}}\rangle &= \sqrt{1/3}\ Y_{1-1}|\alpha\rangle + \sqrt{2/3}\ Y_{10}|\beta\rangle = |8\rangle \\
|2\ \tfrac{3}{2}\ 1\ \tfrac{3}{2}\rangle &= Y_{11}|\alpha\rangle = |9\rangle \\
|2\ \tfrac{3}{2}\ 1\,{-\tfrac{3}{2}}\rangle &= Y_{1-1}|\beta\rangle = |10\rangle \ .
\end{aligned}
\tag{A.1}
$$

The electric field mixes the states $|3\rangle$, $|5\rangle$ and $|7\rangle$ to form new eigenstates

$$
\underset{i=1,2,3}{|\phi_i^{\frac{1}{2}}\rangle} = a_i^{\frac{1}{2}}|3\rangle + b_i^{\frac{1}{2}}|5\rangle + c_i^{\frac{1}{2}}|7\rangle \tag{A.2}
$$

and the states $|4\rangle$, $|6\rangle$ and $|8\rangle$ are mixed to give

$$\underset{i=1,2,3}{|\phi_i^{-\frac{1}{2}}\rangle} = a_i^{-\frac{1}{2}}|4\rangle + b_i^{-\frac{1}{2}}|6\rangle + c_i^{-\frac{1}{2}}|8\rangle \quad . \qquad \text{(A.3)}$$

Noting from Chapter 2, page 29, that

$a_1^m \approx 1$ i.e. $|\phi_1^m\rangle$ is mainly $|3\rangle$ or $|4\rangle$

$b_2^m \approx 1$ $|\phi_2^m\rangle$ is mainly $|5\rangle$ or $|6\rangle$

$c_3^m \approx 1$ $|\phi_3^m\rangle$ is mainly $|7\rangle$ or $|8\rangle$

To further simplify the notation let $|9\rangle = |\phi_4^{\frac{1}{2}}\rangle$ and $|10\rangle = |\phi_4^{-\frac{1}{2}}\rangle$ (n.b. $\pm\frac{1}{2}$ has been substituted for the correct M_J values of $\pm\, ^3/2$).

Immediately after the collision the wavefunction can be written as a superposition of the new eigenstates

$$|\psi\rangle = \sum_{\substack{i=1,2,3,4 \\ \mu=\pm\frac{1}{2}}} g_i^{\mu}|\phi_i^{\mu}\rangle \quad .$$

This expression may be equated with equation (2.57)

$$\sum_{\substack{i=1,2,3,4 \\ \mu=\pm\frac{1}{2}}} g_i^{\mu}|\phi_i^{\mu}\rangle = \sum_{LM} f_{LM}\, Y_{LM}[|\alpha\rangle + e^{i\delta}|\beta\rangle]$$

where the f_{LM} are direct scattering amplitudes.

Forming the products $\langle\phi_i^{\frac{1}{2}}|\psi\rangle$ yields

$$\begin{aligned}
\underset{(i=1,2,3)}{\langle\phi_i^{\frac{1}{2}}|\psi\rangle} = g_i^{\frac{1}{2}} &= [a_i^{\frac{1}{2}}\langle 3| + b_i^{\frac{1}{2}}\langle 5| + c_i^{\frac{1}{2}}\langle 7|][\sum_{LM} f_{LM}Y_{LM}[|\alpha\rangle + e^{i\delta}|\beta\rangle]] \\
&= [a_i^{\frac{1}{2}}(-\sqrt{1/3}\langle\alpha|Y_{10} + \sqrt{2/3}\langle\beta|Y_{11}) + b_i^{\frac{1}{2}}\langle\alpha|Y_{00} \\
&\quad + c_i^{\frac{1}{2}}(\sqrt{2/3}\langle\alpha|Y_{10} + \sqrt{1/3}\langle\beta|Y_{11}][\sum_{LM} f_{LM}Y_{LM}[|\alpha\rangle + e^{i\delta}|\beta\rangle]] \\
&= b_i^{\frac{1}{2}}\, f_{00} + (-\sqrt{1/3}\; a_i^{\frac{1}{2}} + \sqrt{2/3}\; c_i^{\frac{1}{2}})f_{10} + (\sqrt{2/3}\; a_i^{\frac{1}{2}} + \sqrt{1/3}\; c_i^{\frac{1}{2}})e^{i\delta}f_{11}
\end{aligned}$$

(A.4)

and for $i = 4$

$$g_4^{\frac{1}{2}} = <9|[\sum_{LM} f_{LM} Y_{LM}[|\alpha> + e^{i\delta}|\beta>]]$$

$$= <\alpha|Y_{11}[\sum_{LM} f_{LM} Y_{LM}[|\alpha> + e^{i\delta}|\beta>]]$$

$$= f_{11} \tag{A.5}$$

Similarly for $\mu = -\frac{1}{2}$

$$g_i^{-\frac{1}{2}} = b_i^{-\frac{1}{2}} e^{i\delta} f_{00} + (-\sqrt{2/3}\ a_i^{-\frac{1}{2}} + \sqrt{1/3}\ c_i^{-\frac{1}{2}}) f_{1-1}$$
$$+ (\sqrt{1/3}\ a_i^{-\frac{1}{2}} + \sqrt{2/3}\ c_i^{-\frac{1}{2}}) e^{i\delta} f_{10} \tag{A.6}$$

and

$$g_4^{-\frac{1}{2}} = e^{i\delta} f_{1-1} \tag{A.7}$$

Let $a_i^{\frac{1}{2}}(\alpha) = a_i^{\frac{1}{2}} - \sqrt{2}\ c_i^{\frac{1}{2}}$ $\qquad a_i^{\frac{1}{2}}(\beta) = a_i^{\frac{1}{2}} + \sqrt{\tfrac{1}{2}}\ c_i^{\frac{1}{2}}$

$$a_i^{-\frac{1}{2}}(\alpha) = a_i^{-\frac{1}{2}} - \sqrt{\tfrac{1}{2}}\ c_i^{-\frac{1}{2}} \qquad a_i^{-\frac{1}{2}}(\beta) = a_i^{-\frac{1}{2}} + \sqrt{2}\ c_i^{-\frac{1}{2}} \tag{A.8}$$

then

$$g_i^{\frac{1}{2}} = b_i^{\frac{1}{2}} f_{00} - \sqrt{1/3}\ a_i^{\frac{1}{2}}(\alpha) f_{10} + \sqrt{2/3}\ a_i^{\frac{1}{2}}(\beta) e^{i\delta} f_{11} \tag{A.9}$$

$$g_4^{\frac{1}{2}} = f_{11} \tag{A.10}$$

$$g_i^{-\frac{1}{2}} = b_i^{-\frac{1}{2}} e^{i\delta} f_{00} - \sqrt{2/3}\ a_i^{-\frac{1}{2}}(\alpha) f_{1-1} + \sqrt{1/3}\ a_i^{-\frac{1}{2}}(\beta) e^{i\delta} f_{10} \tag{A.11}$$

$$g_4^{-\frac{1}{2}} = e^{i\delta} f_{1-1} \tag{A.12}$$

We note also at this pcint that due to reflection symmetry about the scattering plane

$$f_{1-1} = -f_{11}\ . \tag{A.13}$$

II. Probability for Decay of the Stark Mixed States

The probability of decay from the Stark mixed states to the $IS_{\frac{1}{2}}$ ground state is given by the square of the dipole matrix element

$$P \propto |\langle 1S_{\frac{1}{2}}|e.r|\Psi\rangle|^2 \quad .$$

The total probability may be written as the sum

$$P = P_1 + P_2 + P_3 \tag{A.14}$$

where the interference, or quantum beat, terms have been neglected.

$P_{1(2)}$ is the decay probability for the states $g_{1(2)}^{\pm\frac{1}{2}}|\phi_{1(2)}^{\pm\frac{1}{2}}\rangle$ and P_3 represents the decay probability for the states $g_3^{\pm\frac{1}{2}}|\phi_3^{\pm\frac{1}{2}}\rangle$ as well as the states $g_4^{\pm\frac{1}{2}}|\sigma_4^{\pm\frac{1}{2}}\rangle$.

Each of P_1, P_2 and P_3 can be further split into sums corresponding to the decay paths to the two different ground states and also two orthogonal polarisations of the radiation ($\perp$ and $\|$) giving

$$\underset{i=1,2}{P_i} = \Big|\sum_{\mu=\pm\frac{1}{2}} g_i^{\mu}\langle 1|e_{\perp}.r|\phi_i^{\mu}\rangle + \sum_{\mu=\pm\frac{1}{2}} g_i^{\mu}\langle 1|e_{\|}\cdot r|\phi_i^{\mu}\rangle + \sum_{\mu=\pm\frac{1}{2}} g_i^{\mu}\langle 2|e_{\perp}.r|\phi_i^{\mu}\rangle + \sum_{\mu=\pm\frac{1}{2}} g_i^{\mu}\langle 2|e_{\|}\cdot r|\phi_i^{\mu}\rangle\Big|^2 \tag{A.15}$$

In evaluating (A.14) account must be taken of the rules for combining the probabilities for the different decay paths as discussed in Chapter 2, page 32. Therefore summing coherently over the upper states and incoherently over the lower states yields

$$\begin{aligned}\underset{i=1,2}{P_i} &= \Big|\sum_{\mu=\pm\frac{1}{2}} g_i^{\mu}\langle 1|e_{\perp}.r|\phi_i^{\mu}\rangle\Big|^2 + \Big|\sum_{\mu=\pm\frac{1}{2}} g_i^{\mu}\langle 1|e_{\|}.r|\phi_i^{\mu}\rangle\Big|^2 \\ &\quad + \Big|\sum_{\mu=\pm\frac{1}{2}} g_i^{\mu}\langle 2|e_{\perp}.r|\phi_i^{\mu}\rangle\Big|^2 + \Big|\sum_{\mu=\pm\frac{1}{2}} g_i\langle 2|e_{\|}.r|\phi_i^{\mu}\rangle\Big|^2 \qquad \text{(A.16)} \\ &= P_{A\perp} + P_{A\|} + P_{B\perp} + P_{B\|} \quad .\end{aligned}$$

P_3 is given by a similar expression but with an additional summation over $i = 3$ and 4.

In order to further simplify (A.16) it is first necessary to evaluate the decay matrix elements.

Decay matrix elements:

$\langle 1|e.r|3\rangle = -\sqrt{1/3}\langle Y_{00}|e.r|Y_{10}\rangle$
$\langle 1|e.r|4\rangle = -\sqrt{2/3}\langle Y_{00}|e.r|Y_{1-1}\rangle$
$\langle 1|e.r|5\rangle = 0$
$\langle 1|e.r|6\rangle = 0$
$\langle 1|e.r|7\rangle = \sqrt{2/3}\langle Y_{00}|e.r|Y_{10}\rangle$
$\langle 1|e.r|8\rangle = \sqrt{1/3}\langle Y_{00}|e.r|Y_{1-1}\rangle$
$\langle 1|e.r|9\rangle = \langle Y_{00}|e.r|Y_{11}\rangle$
$\langle 1|e.r|10\rangle = 0$

$\langle 2|e.r|3\rangle = \sqrt{2/3}\langle Y_{00}|e.r|Y_{11}\rangle$
$\langle 2|e.r|4\rangle = \sqrt{1/3}\langle Y_{00}|e.r|Y_{10}\rangle$
$\langle 2|e.r|5\rangle = 0$
$\langle 2|e.r|6\rangle = 0$
$\langle 2|e.r|7\rangle = \sqrt{1/3}\langle Y_{00}|e.r|Y_{11}\rangle$
$\langle 2|e.r|8\rangle = \sqrt{2/3}\langle Y_{00}|e.r|Y_{10}\rangle$
$\langle 2|e.r|9\rangle = 0$
$\langle 2|e.r|10\rangle = \langle Y_{00}|e.r|Y_{1-1}\rangle$

Evaluating the relevant matrix elements for two orthogonal polarisations and for emission in the direction $\phi = \pi$, $\theta = \pi/2$ yields

$$\begin{aligned}
\langle Y_{00}|e_{\perp}.r|Y_{10}\rangle &= 0 \\
\langle Y_{00}|e_{\perp}.r|Y_{11}\rangle &= \sqrt{1/6}\ i\ e^{i\phi} = -\sqrt{1/6}\ i \\
\langle Y_{00}|e_{\perp}.r|Y_{1-1}\rangle &= \sqrt{1/6}\ i\ e^{-i\phi} = -\sqrt{1/6}\ i \\
\langle Y_{00}|e_{\parallel}.r|Y_{10}\rangle &= \sqrt{1/3}\ \sin\theta = \sqrt{1/3} \\
\langle Y_{00}|e_{\parallel}.r|Y_{11}\rangle &= \sqrt{1/6}\ \cos\theta e^{i\phi} = 0 \\
\langle Y_{00}|e_{\parallel}.r|Y_{1-1}\rangle &= -\sqrt{1/6}\ \cos\theta e^{-i\phi} = 0
\end{aligned} \qquad \text{(A.17)}$$

For i = 1 and 2:

$$\begin{aligned}
P_{A\perp} = {} & |g^{\frac{1}{2}}\langle 1|e_{\perp}.r|[a^{\frac{1}{2}}|3\rangle + b^{\frac{1}{2}}|5\rangle + c^{\frac{1}{2}}|\ \rangle] \\
& + g^{-\frac{1}{2}}\langle 1|e_{\perp}.r|[a^{-\frac{1}{2}}|4\rangle + b^{-\frac{1}{2}}|6\rangle + c^{-\frac{1}{2}}|8\rangle]|^2
\end{aligned}$$

where the subscript i has been dropped for clarity

$$\begin{aligned}
= {} & |g^{\frac{1}{2}}a^{\frac{1}{2}}\langle 1|e_{\perp}.r|3\rangle + g^{\frac{1}{2}}c^{\frac{1}{2}}\langle 1|e_{\perp}.r|7\rangle \\
& + g^{-\frac{1}{2}}a^{-\frac{1}{2}}\langle 1|e_{\perp}.r|4\rangle + g^{-\frac{1}{2}}c^{-\frac{1}{2}}\langle 1|e_{\perp}.r|8\rangle|^2 .
\end{aligned}$$

Applying (A.17) gives

$$= |g^{-\frac{1}{2}}a^{-\frac{1}{2}}(-\sqrt{2/3})(-\sqrt{1/6}\ i) + g^{-\frac{1}{2}}c^{-\frac{1}{2}}(\sqrt{1/3})(-\sqrt{1/6}\ i)|^2$$

then substituting (A.8)

$$\begin{aligned}
&= |g^{-\frac{1}{2}}\ (\tfrac{i}{3})\ a^{-\frac{1}{2}}(\alpha)|^2 \\
&= \tfrac{1}{9}\ (a^{-\frac{1}{2}}(\alpha))^2\ |g^{-\frac{1}{2}}|^2 .
\end{aligned}$$

Substituting (A.11)

$$\begin{aligned}
&= \tfrac{1}{9}(a^{-\frac{1}{2}}(\alpha))^2|b^{-\frac{1}{2}}e^{i\delta}f_{00} - \sqrt{2/3}\ a^{-\frac{1}{2}}(\alpha)f_{1-1} + \sqrt{1/3}\ a^{-\frac{1}{2}}(\beta)e^{i\delta}f_{10}|^2 \\
&= \tfrac{1}{9}(a^{-\frac{1}{2}}(\alpha))^2((b^{-\frac{1}{2}})^2|f_{00}|^2 + \tfrac{2}{3}(a^{-\frac{1}{2}}(\alpha))^2|f_{11}|^2 + \tfrac{1}{3}(a^{-\frac{1}{2}}(\beta))^2|f_{10}|^2 \\
&\quad + 2\sqrt{1/3}\ b^{-\frac{1}{2}}a^{-\frac{1}{2}}(\beta)\mathrm{Re}(f_{00}\ f_{10}^{*}))
\end{aligned} \qquad \text{(A.18)}$$

In (A.18) terms including $e^{i\delta}$ vanish since δ is a random phase factor and such terms average to zero over the atomic ensemble.

In order to further simplify (A.18) we note the following relationships

$$\begin{array}{llll}
\text{For } i = 1 & a^{\frac{1}{2}} = a^{-\frac{1}{2}} & b^{\frac{1}{2}} = -\, b^{-\frac{1}{2}} & c^{\frac{1}{2}} = -\, c^{-\frac{1}{2}} \\
\text{For } i = 2 & a^{\frac{1}{2}} = -\, a^{-\frac{1}{2}} & b^{\frac{1}{2}} = b^{-\frac{1}{2}} & c^{\frac{1}{2}} = c^{-\frac{1}{2}} \\
\text{For } i = 3 & a^{\frac{1}{2}} = -\, a^{-\frac{1}{2}} & b^{\frac{1}{2}} = b^{-\frac{1}{2}} & c^{\frac{1}{2}} = c^{-\frac{1}{2}} \, .
\end{array} \qquad (A.19)$$

Using (A.8) and writing (A.18) in terms of $\mu = +\frac{1}{2}$ coefficients only

$$\begin{aligned}
P_{A\perp} &= \tfrac{1}{9}(a^2 + \tfrac{1}{2}c^2 + \sqrt{2}ac)(b^2|f_{00}|^2 + \tfrac{2}{3}(a^2 + \tfrac{1}{2}c^2 + \sqrt{2}\,ac)|f_{11}|^2 \\
&\quad + \tfrac{1}{3}(a^2 + 2c^2 - 2\sqrt{2}\,ac)|f_{10}|^2 + 2\sqrt{1/3}(-ab + \sqrt{2}\,bc)\mathrm{Re}(f_{00}f_{10}^{*})) \\
&= \tfrac{1}{27}\Big[|f_{00}|^2(3b^2(a^2 + \tfrac{1}{2}c^2 + \sqrt{2}\,ac)) \\
&\quad + |f_{10}|^2(a^4 - \tfrac{3}{2}\,a^2c^2 + c^4 - \sqrt{2}\,a^3c + \sqrt{2}\,ac^3) \\
&\quad + |f_{11}|^2(2a^4 + 6a^2c^2 + \tfrac{1}{2}c^4 + 4\sqrt{2}\,a^3c + 2\sqrt{2}\,ac^3) \\
&\quad + \mathrm{Re}(f_{00}f_{10}^{*})(\sqrt{3}\,b(-2a^3 + 3ac^2 + \sqrt{2}\,c^3))\Big] \, .
\end{aligned} \qquad (A.20)$$

Similarly for the other terms

$$\begin{aligned}
P_{A\|} = \tfrac{1}{27}\Big[&|f_{00}|^2(3b^2(a^2 + 2c^2 - 2\sqrt{2}\,ac)) \\
&+ |f_{10}|^2(a^4 + 12a^2c^2 + 4c^4 - 4\sqrt{2}\,a^3c - 8\sqrt{2}\,ac^3) \\
&+ |f_{11}|^2(2a^4 - 3a^2c^2 + 2c^4 - 2\sqrt{2}\,a^3c + 2\sqrt{2}\,ac^3) \\
&- \mathrm{Re}(f_{00}\,f_{10}^{*})(\sqrt{3}b(2a^3 + 12ac^2 - 6\sqrt{2}\,a^2c - 4\sqrt{2}\,c^3))\Big]
\end{aligned} \qquad (A.21)$$

$$\begin{aligned} P_{B\perp} = \frac{1}{27}\Big[& |f_{00}|^2 (3b^2(a^2 + \tfrac{1}{2}c^2 + \sqrt{2}ac)) \\ & + |f_{10}|^2 (a^4 - \tfrac{3}{2} a^2c^2 + c^4 - \sqrt{2}\, a^3c + \sqrt{2}\, ac^3) \\ & + |f_{11}|^2 (2a^4 + 6a^2c^2 + \tfrac{1}{2}c^4 + 4\sqrt{2}\, a^3c + 2\sqrt{2}\, ac^3) \\ & - \mathrm{Re}(f_{00}f_{10}^{*})(\sqrt{3}b(2a^3 - 3ac^2 - \sqrt{2}\, c^3))\Big] \end{aligned} \tag{A.22}$$

$$\begin{aligned} P_{B\parallel} = \frac{1}{27}\Big[& |f_{00}|^2 (3b^2(a^2 + 2c^2 - 2\sqrt{2}\, ac)) \\ & + |f_{10}|^2 (a^4 + 12a^2c^2 + 4c^4 - 4\sqrt{2}\, a^3c - 8\sqrt{2}\, ac^3) \\ & + |f_{11}|^2 (2a^4 - 3a^2c^2 + 2c^4 - 2\sqrt{2}\, a^3c + 2\sqrt{2}\, ac^3) \\ & - \mathrm{Re}(f_{00}f_{10}^{*})(\sqrt{3}b(2a^3 + 12ac^2 - 6\sqrt{2}\, a^2c - 4\sqrt{2}\, c^3))\Big] \end{aligned} \tag{A.23}$$

Substituting (A.20) - (A.23) into (A.16) yields for $i = 1$ and 2

$$\begin{aligned} P = \frac{1}{27}\Big| & |f_{00}|^2 (3b^2(4a^2 + 5c^2 - 2\sqrt{2}\, ac)) \\ & + |f_{10}|^2 (4a^4 + 21a^2c^2 + 10c^4 - 10\sqrt{2}\, a^3c - 14\sqrt{2}\, ac^3) \\ & + |f_{11}|^2 (8a^4 + 6a^2c^2 + 5c^4 + 4\sqrt{2}\, a^3c + 8\sqrt{2}\, ac^3) \\ & \pm \mathrm{Re}(f_{00}f_{10}^{*})(\sqrt{3}b(-8a^3 - 18ac^2 + 12\sqrt{2}\, a^2c + 10\sqrt{2}\, c^3))\Big] \end{aligned} \tag{A.24}$$

An essentially similar calculation for P_3 but including the $|\phi_4^{\mu}>$ states yields

$$\begin{aligned} P_3 = \frac{1}{27}\Big| & |f_{00}|^2 (3b^2(4a^2 + 5c^2 - 2\sqrt{2}\, ac)) \\ & + |f_{10}|^2 (4a^4 + 21a^2c^2 + 10c^4 - 10\sqrt{2}\, a^3c - 14\sqrt{2}\, ac^3) \\ & + |f_{11}|^2 (8a^4 + 6a^2c^2 + 5c^4 + 4\sqrt{2}\, a^3c + 8\sqrt{2}\, ac^3 + 9 - 12a^2 - 6c^2 - 12\sqrt{2}ac) \\ & - \mathrm{Re}(f_{00}f_{10}^{*})(2\sqrt{3}b(4a^3 - 6\sqrt{2}\, a^2c + 9ac^2 - 5\sqrt{2}\, c^3))\Big] \end{aligned} \tag{A.25}$$

Substituting the values for a, b and c from the table on page 29 gives

$$\begin{aligned} P_1 &= 1.68|f_{00}|^2 + 3.11|f_{10}|^2 + 5.46|f_{11}|^2 + 4.58\mathrm{Re}(f_{00}f_{10}^*) \\ P_2 &= 1.50|f_{00}|^2 + 0.06|f_{10}|^2 + 0.25|f_{11}|^2 - 0.58\mathrm{Re}(f_{00}f_{10}^*) \\ P_3 &= 0.09|f_{00}|^2 + 9.96|f_{10}|^2 + 8.00|f_{11}|^2 - 1.93\mathrm{Re}(f_{00}f_{10}^*) \end{aligned} \tag{A.26}$$

Finally the quantities (A.26) are related to the coefficients C_i of equation (2.62) by

$$\begin{aligned} \underset{i=1,2}{C_i} &= K\, P_i \\ [C_3 + C_4] &= K\, P_3 \end{aligned} \tag{A.27}$$

where K is a constant depending on experimental parameters.

APPENDIX B

Modification to Electron Trajectories due to the Electric Field

Figure 26 illustrates the effect that the electric field has on electrons which are initially scattered through an angle θ_e. Due to the acceleration of the electrons in the z-direction by the field these electrons will enter the detector as if they had been scattered through an angle θ_e' .

Let $2d$ = separation of the field plates

r = distance of the detector from the collision region

E = energy of electrons in eV after the collision

ε = electric field strength in Vm^{-1}

and take the origin of coordinates to be the collision region. For an electron scattered through an angle θ_e the velocity immediately after the collision may be specified in terms of the two components

$$U_z = \left(\frac{2eE}{m}\right)^{\frac{1}{2}} \cos\theta_e$$

$$U_y = \left(\frac{2eE}{m}\right)^{\frac{1}{2}} \sin\theta_e \quad . \qquad \text{B.1}$$

The electric field produces an acceleration in the z-direction given by

$$a = \frac{-e\varepsilon}{m} \quad .$$

As the electrons leave the field region, i.e. $z = d$,

$$V_z = (U_z^{\,2} + 2ad)^{\frac{1}{2}} \qquad \text{B.2}$$

and

$$V_y = U_y \quad . \qquad \text{B.3}$$

The time spent in the field is given by

$$t = \frac{V_z - U_z}{a} .$$

After time t we have

$$y_p = U_y t \qquad \text{B.5}$$

$$z_p = d .$$

Referring to Fig. 27

$$y_{det} = r \sin \theta_e' \qquad \text{B.6}$$

$$z_{det} = r \cos \theta_e' .$$

The angle $\beta = \alpha + 180 - \phi$ B.7

and $\delta = 180 - \beta - (\phi - \theta_e')$

$$= \theta_e' - \alpha . \qquad \text{B.8}$$

Therefore

$$\frac{r}{\sin(\phi - \alpha)} = \frac{\ell_\delta}{\sin(\theta_e' - \alpha)} . \qquad \text{B.9}$$

where

$$\ell_\delta = (y_p^2 + z_p^2)^{\frac{1}{2}} . \qquad \text{B.10}$$

Re-arranging B.9 yields

$$\sin(\theta_e' - \alpha) = \frac{(y_p^2 + z_p^2)^{\frac{1}{2}}}{r} \sin(\phi - \alpha) \qquad \text{B.11}$$

From Figure 27

$$\phi = \tan^{-1}\left(\frac{y_p}{z_p}\right) \qquad \text{B.12}$$

and from Figure 26

$$\alpha = \tan^{-1}\left(\frac{V_y}{V_z}\right) . \qquad \text{B.13}$$

Finally, substituting the appropriate expressions into B.11 yields

$$
\begin{aligned}
\theta'_e = \sin^{-1}\{ \Big[& \frac{2eE}{mr^2a^2}\sin^2\theta_e((\frac{2eE}{m}\cos^2\theta_e - \frac{2e\varepsilon}{m}d)^{\frac{1}{2}} \\
& - (\frac{2eE}{m})^{\frac{1}{2}}\cos\theta_e)^2 + d^2 \Big|^{\frac{1}{2}} \\
& \times \sin \Big| \tan^{-1}((\frac{2eE}{m})^{\frac{1}{2}}\sin\theta_e((\frac{2eE}{m}\cos^2\theta_e - \frac{2e\varepsilon}{m}d)^{\frac{1}{2}} \\
& - (\frac{2eE}{m})^{\frac{1}{2}}\cos\theta_e)(\frac{-m}{e\varepsilon d})) \\
& - \tan^{-1}((\frac{2eE}{m})^{\frac{1}{2}}\sin\theta_e(\frac{2eE}{m}\cos^2\theta_e - \frac{2e\varepsilon}{m}d)^{-\frac{1}{2}})\Big]\} \\
& + \tan^{-1}((\frac{2eE}{m})^{\frac{1}{2}}\sin\theta_e(\frac{2eE}{m}\cos^2\theta_e - \frac{2e\varepsilon}{m}d)^{-\frac{1}{2}})
\end{aligned} \tag{B.14}
$$

B.14 then gives the angle at which an electron initially scattered through θ_e will be detected. θ'_e was calculated for a range of scattering angles θ_e and the results are shown in Table 2.

APPENDIX C

Determination of the Phase δ from measurements of R_2, R_{13} and λ.

From equation (5.9) we may write

$$M_2 = \frac{C_2}{\mathbb{P}} tp \qquad (C.1)$$

$$M_1+M_3 = \frac{[C_1+C_3+C_4]}{\mathbb{P}} tp$$

where the quantities C_i are given by equations (2.66) and $\mathbb{P}$ by (5.8). Expanding the expressions C.1

$$M_2 = \frac{[1.50|f_{00}|^2 + 3.11|f_{10}|^2 + 5.46|f_{11}|^2 + 4.58\mathrm{Re}(f_{00}f_{10}^*)]1.6}{[17.3|f_{00}|^2 + 22.6|f_{10}|^2 + 25.7|f_{11}|^2 + 3.4\mathrm{Re}(f_{00}f_{10}^*)]} \qquad (C.2)$$

$$M_1+M_2 = \frac{[1.77|f_{00}|^2 + 13.07|f_{10}|^2 + 13.46|f_{11}|^2 + 2.65\mathrm{Re}(f_{00}f_{10}^*)]1.6}{[17.3|f_{00}|^2 + 22.6|f_{10}|^2 + 25.7|f_{11}|^2 + 3.4\ \mathrm{Re}(f_{00}f_{10}^*)]}$$

Dividing top and bottom of expressions (C.2) by $|f_{11}|^2$ and putting $\alpha = |f_{10}|^2/|f_{11}|^2$ and $\varepsilon = \mathrm{Re}(f_{00}f_{10}^*)$ gives

$$M_2 = \frac{[1.50|f_{00}|^2/|f_{11}|^2 + 3.11\alpha + 5.46 + 4.58\varepsilon/|f_{11}|^2]1.6}{[17.3|f_{00}|^2/|f_{11}|^2 + 22.6\alpha + 25.7 + 3.4\ \varepsilon/|f_{11}|^2]} \qquad (C.3)$$

$$M_1+M_3 = \frac{[1.77|f_{00}|^2/|f_{11}|^2 + 13.07\alpha + 13.46 + 2.65\varepsilon/|f_{11}|^2]1.6}{[17.3|f_{00}|^2/|f_{11}|^2 + 22.6\alpha + 25.7 + 3.4\ \varepsilon/|f_{11}|^2]}$$

Now $$\lambda = \frac{|f_{10}|^2}{|f_{10}|^2 + 2|f_{11}|^2}$$

therefore $$\frac{2\lambda}{1-\lambda} = \frac{|f_{10}|^2}{|f_{11}|^2} = \alpha. \qquad (C.4)$$

Thus measurements of the λ parameter permit α to be determined. Expressions (C.3) may then be solved to yield values for the quantities $|f_{00}|^2/|f_{11}|^2$ and $\varepsilon/|f_{11}|^2$.

Now $$\frac{\varepsilon}{|f_{11}|^2} = \frac{\mathrm{Re}(f_{00}f_{10}^{*})}{|f_{11}|^2} = \frac{|f_{00}||f_{10}|\cos\delta}{|f_{11}|^2}$$

and thus $$\cos\delta = \frac{\varepsilon/|f_{11}|^2}{|f_{00}||f_{10}|/|f_{11}|^2}$$

$$= \frac{\varepsilon/|f_{11})|^2}{|f_{00}|/|f_{11}| \;\; |f_{10}|/|f_{11}|}$$

$$= \frac{\varepsilon/|f_{11}|^2}{(\alpha\;|f_{00}|^2/|f_{11}|^2)^{\frac{1}{2}}}$$

giving

$$\delta = \cos^{-1}\left[\frac{\varepsilon/|f_{11}|^2}{(\alpha\;|f_{00}|^2/|f_{11}|^2)^{\frac{1}{2}}}\right] \qquad \text{(C.5)}$$

BIBLIOGRAPHY

(1) Moiseiwitsch, B.L. and Smith, S.J. 1968 Rev. Mod. Phys. 45, 238.

(2) Williams, K.L. 1969 Proc. IVth I.C.P.E.A.C., Ed. I Andur (Cambridge, Mass.: M.I.T. Press).

(3) Williams, J.F. and Willis, B.A. 1975 J. Phys. B: Atom. Molec. Phys. 8, 1641.

(4) Long, R.L., Cox, D.M. and Smith, S.J. 1968 J. Res. N.B.S. A 79, 549.

(5) McGowan, J.W., Williams J.F. and Curley, E.K. 1969 Phys. Rev. 180, 132.

(6) Williams, J.F. and Willis, B.A. 1974 J. Phys. B: Atom Molec. Phys. 7, L61.

(7) Ott, W.R., Kauppila, W.E. and Fite W.L. 1970 Phys. Rev. A 1, 1089.

(8) Kauppila, W.E., Ott, W.R. and Fite, W.L. 1970 Phys. Rev. A 1, 1099.

(9) Brady, E.L. and Deutsch, M. 1947 Phys. Rev. 72, 870.

(10) Dunsworth, J.V. 1940 Rev. Sci. Inst. 11, 167.

(11) Hamilton, D.R. 1940 Phys. Rev. 58, 122.

(12) Racah, G. 1951 Phys. Rev. 84, 910.

(13) Coester, F. and Jauch, J.M. 1952 Helvetica Physica Acta 26, 3.

(14) Macek, J.H. and Jaecks, D.H. 1971 Phys. Rev. A 4, 2288.

(15) Fano, U. and Macek, J.H. 1973 Rev. Mod. Phys. 45, 553.

(16) Blum, K. 1981 Density Matrix Theory and Applications (Plenum Press).

(17) Fano, U. 1957 Rev. Mod. Phys. 29, 74.

(18) Slevin, J. 1984 Rep. Prog. Phys. 47, 461.

(19) Eminyan, M., MacAdam, K.B., Slevin, J. and Kleinpoppen, H. 1974 J. Phys. B: Atom. Molec. Phys. 7, 1519.

(20) Sutcliffe, V.C., Haddad, G.N., Steph, N.C. and Golden, D.E. 1978 Phys. Rev. A 17, 100.

(21) Hollywood, M.T., Crowe, A. and Williams, J.F. 1979 J. Phys. B: Atom. Molec. Phys. 13, 3009.

(22) Slevin, J., Porter, H.Q., Eminyan, M., Defrance, A. and Vassilev, G. 1980 J. Phys. B: Atom. Molec. Phys. 13, 3009.

(23) Steph, N.C. and Golden, D.E. 1980 Phys. Rev. A 21 759.

BIBLIOGRAPHY (Contd.)

(24) McAdams, R., Hollywood, M.T., Crowe, A. and Williams, J.F. 1980 J. Phys. B: Atom. Molec. Phys. 13, 3691.

(25) van Linden van den Heuvell, H.B., van Eck, J. and Heideman, H.G.M. 1982 J. Phys. B: Atom. Molec. Phys. 15, 3517.

(26) Crowe, A. and Nogueira, J.C. 1982 J. Phys. B: Atom. Molec. Phys. 15, L501.

(27) Crowe, A., Nogueira, J.C. and Liew, Y.C. 1983 J. Phys. B: Atom. Molec. Phys. 16, 481.

(28) Beijers, J.P.M., van Eck, J. and Heideman, H.G.M. 1984 J. Phys. B: Atom. Molec. Phys. 17, L265.

(29) Standage, M.C. and Kleinpoppen, H. 1975 Phys. Rev. Lett. 36, 577.

(30) van Linden van den Heuvell, H.B., Nienhuis, G., van Eck, J. and Heideman, H.G.M. 1983 J. Phys. B: Atom. Molec. Phys. 16, 1619.

(31) van Linden van den Heuvell, H.B., van Gasteren, E.M., van Eck, J. and Heideman, H.G.M. 1983 J. Phys. B: Atom. Molec. Phys. 16, 1619.

(32) Williams, J.F. 1975 Proc. IXth I.C.P.E.A.C., Ed. J. Risley (Seattle: University of Washington Press).

(33) Dixon, A.J., Hood, S.T. and Weigold, E. 1978 Phys. Rev. Lett. 40, 1262.

(34) Hood, S.T., Weigold, E. and Dixon, A. 1979 J. Phys. B: Atom. Molec. Phys. 12, 631.

(35) Weigold, E., Frost, L. and Nygaard, K.J. 1980 Phys. Rev. A 21, 1950.

(36) Slevin, J., Eminyan, M., Woolsey, J.M., Vassilev, G. and Porter, H.Q. 1980 J. Phys. B: Atom. Molec. Phys. 13, L341.

(37) Frost, L. and Weigold, E. 1980 Phys. Rev. Lett. 45, 247.

(38) Williams, J.F, 1981 J. Phys. B: Atom. Molec. Phys. 14, 1197.

(39) Slevin, J., Eminyan, M., Woolsey, J.M., Vassilev, G., Porter, H.Q. , Back, C.G. and Watkin, S. 1982 Phys. Rev. A 26, 1344.

(40) Macek, J. 1969 Phys. Rev. Lett. 23, 1.

(41) Macek, J. and Burns, D. 1976 Beam Foil Spectroscopy, Ed. S Bashkin (Springer, Berlin).

(42) Teubner, P.J.O., Furst, J.E., Tonkin, M.C. and Buckman, S.J. 1981 Phys. Rev. Lett. 46, 1569.

BIOGRAPHY (Contd.)

(43) Eck, T.G. 1973 Phys. Rev. Lett. 31, 270.

(44) Burns, D.J. and Hancock, W.H. 1971 Phys. Rev. Lett. 27, 370.

(45) Mahan, A.H. and Smith, S.J. 1977 Phys. Rev. A 16, 1789.

(46) Krotkov, R. 1975 Phys. Rev. A 12, 1793.

(47) Blum, K. and Kleinpoppen, H. 1977 J. Phys. B: Atom. Molec. Phys. 10, 3283.

(48) Gabrielse, G. abd Band, Y.B. 1977 Phys. Rev. Lett. 39, 697.

(49) Sellin, I.A., Mowat, J.R., Peterson, R.S., Griffin, P.M., Laubert, R. and Haselton, H.H. 1973 Phys. Rev. Lett. 31, 1335.

(50) Gaupp, A., Andrä, H.J. and Macek, J. 1974 Phys. Rev. Lett 32, 268.

(51) Sellin, I.A., Liljeby, L., Mannervik, S. and Hultberg, S. 1979 Phys. Rev. Lett. 42, 570.

(52) Havener, C.C., Westerveld, W.B. and Risley, J.S. 1982

(53) Krotkov, R. and Stone, J. 1980 Phys. Rev. A 22, 473.

(54) Burgdörfer, J. 1981 Phys. Rev. A 24, 1756.

(55) Corney, A. 1977 Atomic and Laser Spectroscopy (Oxford: Oxford University Press).

(56) Völkel, M. and Sandner, W. 1983 J. Phys. E: Sci. Inst. 16, 456.

(57) Slevin, J. and Stirling, W. 1981 Rev. Sci. Inst. 52, 1780.

(58) Wood, B.J. and Wise, H. 1962 J. Phys. Chem. 66, 1049.

(59) Muggleton, A.H.F. and Parsons, C.T. 1963 Rev. Sci. Inst. 34, 804.

(60) Grossberg, A.B. 1973 Fortran for Engineering Physics (McGraw-Hill Book Company).

(61) Mazeau, M.J. 1974 Ph.D. Thesis.

(62) Harting, E. and Read 1976 Electrostatic Lenses (Amsterdam: Elsevier).

(63) Wiza, J.L. 1979 Nucl. Inst. Meth. 162, 587.

(64) Green, M.I., Kenealy, P.F. and Beard, G.B. 1975 Nucl. Inst. Meth. 126, 175.

(65) Timothy, J.G. 1981 Rev. Sci. Ubst, 52, 1131.

BIBLIOGRAPHY (Contd.)

(66) Samson, J.A.R. 1967 Techniques of Vacuum Ultraviolet Spectroscopy (John Wiley and Sons).

(67) Holzapfel, C. 1974 Rev. Sci. Inst. 45, 894.

(68) Fargher, H.E. 1983 Ph.D. Thesis.

(69) Baluja, K.L., McDowell, M.R.C., Morgan, L.A. and Myerscough, V.P. 1978 J. Phys. B: Atom. Molec. Phys. 11, 715.

(70) Walters, H.R.J. 1983 Private communication.

(71) Fargher, H.E. and Roberts, M.J. 1983(a) J. Phys. B: Atom. Molec. Phys. 16, 1077; 1983(b) J. Phys. B: Atom, Molec. Phys. 16, 4427.

(72) Imhof, R.E. and Read, F.H. 1971 J. Phys. B: Atom. Molec. Phys. 4, 450.

(73) Back, C.G., Watkin, S., Eminyan, M., Rubin, K., Slevin, J. and Woolsey, J.M. 1984 J. Phys. B: Atom. Molec. Phys. 17, 2695.

ACKNOWLEDGEMENTS

Firstly I wish to record my gratitude to Dr. J. Slevin for supervising this research and for his encouragement and guidence throughout. I thank Mr. C. Back for his assistance and advice in many stages of this work, and also Dr. J.M. Woolsey, Professor M. Eminyan and Professor K. Rubin. I also wish to thank Mr. A.J. Duncan and members of the shared technical services for their technical advice and cooperation. Finally I thank the Carnegie Trust for the Universities of Scotland for financial support.